UNIVERSITY OF IOANNINA
SCHOOL OF SCIENCES
DEPARTMENT OF PHYSICS

RELAXATION PROCESSES IN Cu-Zr METALLIC GLASSES BY MOLECULAR DYNAMICS SIMULATIONS

A thesis presented

By

PABLO ANTONIO PALOMINO RICO

To

The Department of Physics
in partial fulfilment of the requirements for the degree of
Doctor in Philosophy
in the subject of Physics

IOANNINA 2018

UNIVERSITY OF IOANNINA
SCHOOL OF SCIENCES
DEPARTMENT OF PHYSICS

RELAXATION PROCESSES IN Cu-Zr METALLIC GLASSES BY MOLECULAR DYNAMICS SIMULATIONS

A thesis presented

By

PABLO ANTONIO PALOMINO RICO

To

The Department of Physics
in partial fulfilment of the requirements for the degree of
Doctor in Philosophy
in the subject of Physics

IOANNINA 2018

Consultative jury:

- Γ. Ευαγγελάκης (G. Evangelakis). Καθηγητής Τμήματος Φυσικής Π. Ι. (επιβλέπων)
- Δ. Παπαγεωργίου (D. Papageorgiou). Αναπλ. Καθηγητής ΤΜΕΥ Π. Ι.
- Χ. Λέκκα (Ch. Lekka). Αναπλ. Καθηγήτρια ΤΜΕΥ

Examining jury:

- Γ. Ευαγγελάκης (G. Evangelakis). Καθηγητής Τμήματος Φυσικής Π. Ι. (επιβλέπων)
- Ι. Λαγαρής (I. Lagaris). Καθηγητής Τμήματος Μηχανικών Πληροφορικής Π. Ι.
- Ι. Δεληγιαννάκης (I. Deligiannakis). Καθηγητής Τμήματος Φυσικής Π. Ι.
- Θ. Μπάκας (Th. Bakas). Καθηγητής Τμήματος Φυσικής Π. Ι.
- Ε. Λοιδωρίκης (E. Lidorikis). Καθηγητής ΤΜΕΥ Π. Ι.
- Δ. Παπαγεωργίου (D. Papageorgiou). Αναπλ. Καθηγητής ΤΜΕΥ Π. Ι.
- Χ. Λέκκα (Ch. Lekka). Αναπλ. Καθηγήτρια ΤΜΕΥ

ABSTRACT

We present Molecular Dynamics simulations results referring to relaxation processes, occurring in $Cu_{65}Zr_{35}$ computer glass at the quiescent state, during tensile solicitation, as well as the stress releasing effect that takes place when this material is under constant strain. The study comprises a thorough analysis of the thermodynamics, structural and dynamical properties of this system. We found a rattling mode of atomic motions that takes place in highly localized regions characterized by their high mobility and low local density and composed mostly by loosely packed clusters of atoms. The rattling mode has a frequency that is essentially independent from both temperature and applied strain. However, the regions where the rattling atoms are localized, and thus the fractions of atoms undergoing rattling, increase with temperature and applied strain. It is argued that the rattling motions constitute the 'fast processes' that lie between the β relaxation and the Boson peak in the characteristic spectrum of dynamic modes in glasses. In addition, we found that our glass exhibited a characteristic endothermic response upon straining, which has not been reported before. The study of this response and its evolution upon straining indicates the presence of aging and rejuvenation processes and delimits the different stages at which each one of these processes is dominant in our glass. It is concluded that the fast processes are precursors of the β relaxation mode, and could be considered as predictors of the spatial origin of the shear transformation zones, governing the onset of plastic flow. Furthermore, during the stress relaxation process occurring when the glass is subjected to a fixed strain, the location of the rattling atoms coincides with the heterogeneous regions where most of the stress and energy of the system is being released, thus they act as the stress mediators of the metallic glasses. These results could be useful for the understanding of the complex relaxation spectrum of the metallic glasses and provide a better insight of the intricate relaxation dynamics that characterizes these materials, especially at the higher frequency region. Moreover, the results presented here have important consequences in the macroscopic properties of metallic glasses, like ductility, brittleness and toughness fracture. It turns out, therefore, that understanding the structural and dynamical behaviour of the MGs during these relaxation processes is crucial for eventual control and improvement of their properties.

ACKNOWLEDGEMENTS

Almost four years have passed since I left my country and embarked on a trip to Greece. The Physics Department of Ioannina notified me my acceptance as a PhD student the day of my birthday. I still remember myself shouting out to the world, entranced:

"A veces la vida es como una función seno... Esta vez me tocó una interferencia constructiva de mil senos, y peté del subidón! ME VOY A GRECIA A DOCTORARME CON UNA MARIE CURIE!!! (Otro que se fuga...)"

It has been a very intense and interesting period of my life and I would like to take a moment to dedicate a few words to some very special persons: to the ones that most supported me during this journey, but also to the ones that had a deeply impact in my life and helped me become the person I am.

I am a Physicist: an observer and a modeller. To obtain the "Philosophiae doctor" degree in Physics was a dream, for a long time. Many mentors guided and assisted me along this path. In my school years, Don Francisco helped me develop my logical reasoning and Don Emilio contributed to improve my critical thinking. During high school, Paulina and Natividad increased my interest in mathematics. After high school, the paths diverge and an important decision must be taken. I remember asking my tutor, Natividad: "Mathematics in Málaga or Physics in Granada?" She knew me and she didn't doubt it: "Physics in Granada". She pointed me the right direction. My years at the university were fascinating and many professors profoundly impacted me: Maria del Carmen Carrión, José Callejas, Alfonso Salinas, Arturo Moncho and Ángel Delgado, between others, forged me, not only as a physicist, but also as a person. During my PhD in Greece, I was also blessed. My supervisor, Prof. Γ. Ευαγγελάκης took me under his wing. He guided and supported me at all times, even during the most difficult ones, when I needed it more. He even introduced me to his family, which no mentor had done before. I felt really esteemed. He is one of those persons that I will never forget. I was also strongly supported by the others members of my advisory committee: Assoc. Prof. Δ. Παπαγεωργίου and Assoc. Prof. Χ. Λέκκα. They were always there. Always. Moreover, during my PhD studies, I was graced to be part of a formidable group of Professors and researchers: the VitriMetTech ITN. I am very thankful to all of them. In particular, I felt really privileged to have the opportunity to work closely with Prof. A.L. Greer, a beautiful person and a great scientist. To all these teachers and professors: I owe you, not only my abilities, skills and knowledge, acquired during many years, but also my curiosity, interest and motivation, which are fundamental for a physicist. You all have something in common: you reached out to me.

You taught me through emotions, because you made me feel especial. I am, and always will be, grateful to you. So please, keep it up. Keep making the students to come feel especial, because you have a huge power: to deeply influence other people's life, and with great power comes great responsibility.

Humans are social beings and people around us most certainly can immensely influence us. In that sense, I consider myself very lucky, because I have been being surrounded by extremely delightful persons: my friends. David Pérez, Helena Bosch, Rosa Aguilera, Noé Lifona, David Roca, Manuel Sánchez, Jesús Vera, Gloria Luque, Luis Serrano Díaz, Rocío Cebrero, Ángel Cobo, José Galván, María Casinello, Julio Gutiérrez, Julio Abril, Noelia De Alda, Javier Orquín, Karel de Jongh, Laura Burgos, Antonio Pujante, Ιωάννης Μανωλάρας, Γιούλη Πανταζή, Αλεξάνδρα Τσόλκα, Ευάγγελος Καζάκος, Ιωάννης Βαγγελίδης, Αντωνία Ζησοπούλου, Αλεξανδρα Λαγογιάννη, Γιώργος Αλμύρας and Ναταλία Μουζοκέ, between others. I would need many pages to thank you all individually, but I am afraid that these acknowledgements are already getting out of hand and I still have not said anything about my family. I just wanted you to know that I am incredibly grateful our paths have crossed at some point in life. I love you. For the one I have not mentioned, please, forget me if your name is not here. It is in my heart, were it matters most.

Last, but no least, I would like to dedicate some words to my family. First, I want to thank my parents: Isabel Rico and Francisco Palomino, who granted me life, and moulded me, to become the person I am. There are no words to express the joy of being your son. My brothers: Borja, Jorge and Misael, who have been always next to me, supporting and accompanying me. To my grandparents Mercedes and Francisco and my uncles: you have all contributed to create the best possible environment around me. I love you.

Por último, pero no menos importante, me gustaría dedicar unas palabras a mi familia. Primero, quiero agradecer a mis padres: Isabel Rico y Francisco Palomino, quienes me concedieron la vida, y me moldearon, para convertirme en la persona que soy. No hay palabras para expresar la alegría de ser vuestro hijo. Mis hermanos, Borja, Jorge y Misael, quienes han estado siempre a mi lado, apoyándome y acompañándome. A mis abuelos Mercedes y Francisco y a mis tíos: Todos habéis contribuido a crear el mejor entorno posible a mi alrededor. Os quiero.

This work is supported by VitriMetTech Project FP7-PEOPLE- 2013-ITN-#607080.

Caminante, son tus huellas
el camino, y nada más;
caminante, no hay camino,
se hace camino al andar,
Al andar se hace el camino,
y al volver la vista atrás
se ve la senda que nunca
se ha de volver a pisar.
Caminante, no hay camino,
sino estelas en el mar.

Proverbios y cantares XXIX, Antonio Machado.
Campos de Castilla, 1912.

Wanderer, your footsteps are
the road, and nothing more;
wanderer, there is no road,
the road is made by walking.
By walking one makes the road,
and upon glancing behind
one sees the path
that never will be trod again.
Wanderer, there is no road,
only wakes upon the sea.

Selected Poems of Antonio Machado,
transl. by Betty Jean Craige,
University of Georgia, 1978.

Dedicated to my family, specially to Alba,
who very recently granted me the title of “uncle”.

CONTENTS

1) Metallic glasses

A glass is a solid material in which the atomic structure is non-crystalline (or amorphous) and exhibits a glass transition upon heating towards the liquid state. One of the processes to obtain glassy alloys is by means of fast cooling. Metallic glasses (MGs), also called amorphous metals, were reported for the first time in 1960 by Klement, Willens and Duwetz [1]. Using extremely high cooling rates, of the order of 10^6 K/s, they were able to quench a molten Gold-Silicon alloy to an amorphous glassy structure. Unfortunately, the high cooling rates needed restricted one of the dimensions of the material that could be obtained to 20-50 μm, thus limiting the geometries that could be produced to ribbons, wires and powders. Therefore, the early research on MGs was focused on the discovery of new alloys with an enhanced glass forming ability (GFA) and lower cooling rates requirements in order to allow for the manufacture of larger pieces, i.e. bulk metallic glasses (BMGs). In the late 1980s and '90s the work of Inoue lead to a broader range of metallic glasses with a better GFA and lower requirements regarding the cooling rates [2]–[7].

1.1) The glass transition

When a liquid is cooled down below its melting point (T_m) without crystallization taking place, it is called a supercooled liquid (SCL) or undercooled liquid. SCLs retain some structural aspects from the liquid state. The dynamics of these systems can be assessed by means of the viscosity (η) that increases dramatically upon cooling. Such an increase in the viscosity hinders the atomic rearrangements in SCLs, resulting in the volume alteration with respect to the equilibrium volume at the corresponding temperature. When the temperature is further decreased, the system "freezes" in a metastable state, thus forming a glass (provided that no nucleation or crystal growth occurs). Fig. 1.1 shows the variation of specific volume as a function of temperature. The glass transition temperature (T_g) is commonly defined as the temperature at which the viscosity reaches 10^{12} Pa·s [8], and it depends on the way the glass is prepared. For

instance, higher cooling rates mean that the atoms have less time to rearrange. Consequently, the deviation from the supercooled liquid regime occurs at higher temperatures. Due to this dependency, the glass transition does not appear as a true thermodynamic phase transition but rather a kinetic effect. In fact, the glassy state below T_g is not an equilibrium state and timescales play an important role here: Although MGs look like solids on experimental timescales of years, they may look like liquids at geological timescales. For this reason, we will refer to this state as metastable or quiescent.

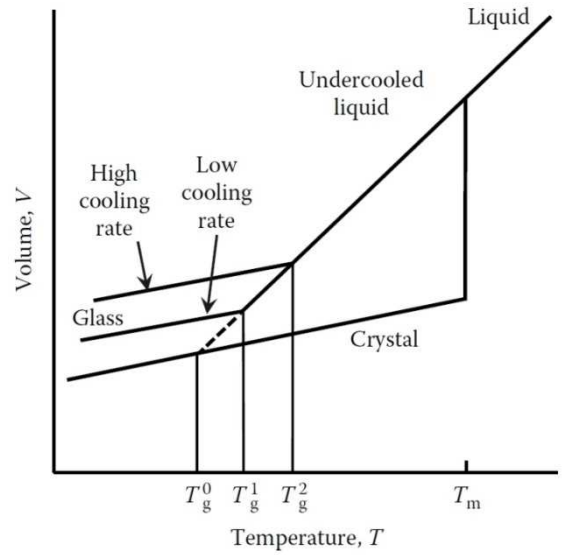

Fig. 1.1) Variation of specific volume with respect to temperature for a crystal and a glass-forming material [9].

1.2) Atomic structure of metallic glasses

One of the fundamental differences between crystalline and amorphous materials resides in their structure. In the case of crystalline materials, the atomic structure is highly ordered: a unit cell consisting of a fixed number of atoms is periodically repeated in all directions, providing a long range order. This is not true for amorphous materials, and in that sense, they lack long range translational or orientational order. Nevertheless, a significant degree of short and even medium range order was predicted, and confirmed

experimentally afterwards [10]–[12]. However, the large amount of possible structural configurations of amorphous system complicates their atomic structure analysis and many efforts have been done in order to reveal in detail the microstructure of MGs.

Since MGs can be considered as being basically frozen liquids, it is reasonable to expect certain similarities with the atomic structure of SCL, which was suggested to consist of icosahedral (ICO) clusters by Frank [13], [14] in order to explain their stability below the melting temperature. ICO atomic clusters have five-fold symmetry, and as a consequence, they lack translational periodicity but provide high packing efficiency and therefore density. Although ICO clusters dominate the atomic structure of MGs, experimental results report a large variety of different clusters geometries participating in their atomic structural arrangement [12], [15]. These geometries, often called Kasper polyhedra [14], could be considered as the main underlying topological short range order (SRO) in MGs, however, the fact that, in reality, most of these clusters are distorted and/or truncated further complicates their identification and analysis.

The SRO is not sufficient to fully characterize the structure of amorphous metals. In crystalline solids, the symmetric packing of the unit cell links atomic and macroscopic scale. In amorphous metals however, the rules by which atomic clusters combine to form dense bulk glasses are not so obvious, and several models have been proposed. Miracle [16] considered the solute centred atomic clusters as spheres and suggested that they are efficiently packed in the form of face-centred cubic (FCC) or hexagonal closed packed (HCP) patterns, composing the medium range order (MRO). Such MRO would extend to a few cluster diameters (~1nm), when the order breaks down due to internal strains and packing frustration. Adjacent clusters share solvent atoms preferably in common faces to minimize volume but also in common edges or vertices due to internal strains. Sheng *et al*. [12] suggested a similar model in which the solute centred clusters occupy the vertices of bigger icosahedral patterns in the case of alloys with a low solute concentration and strings or networks in alloys with a high solute concentration.

In the particular case of the Cu-Zr model system, Molecular dynamics (MD) simulations predicted that the atomic structure is basically composed of ICO Cu-centred clusters and Zr-centred rhombic dodecahedral (RD) clusters, in different proportions and compositions, depending between others factors, on the stoichiometry of the system [17]. Experimental results [18] support the MD predictions. Regarding the MRO of the Cu-Zr alloy, Almyras *et al*. [17] suggested that it was composed by Superclusters that

preserve the stoichiometry of the system and are formed by interconnecting ICO-like atomic clusters (Fig. 1.2). Li *et al* [18] suggested that the MRO consist of a string like backbone network formed as well by ICO clusters and a liquid like structure filling the remaining space.

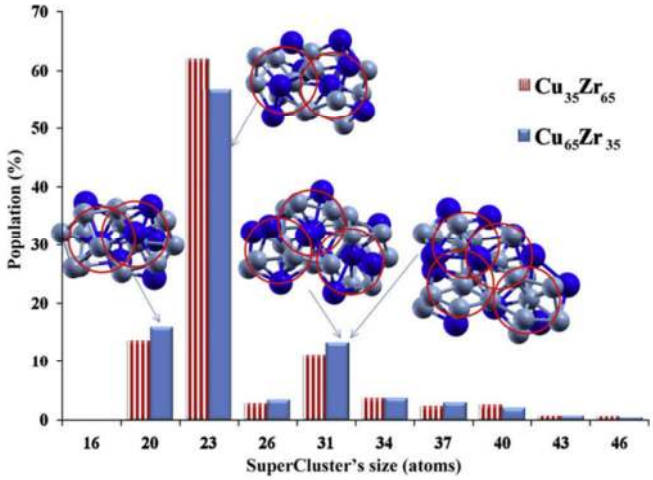

Fig. 1.2) Populations of Superclusters for two different Cu-Zr compositions [17].

1.3) Potential energy landscape and structural relaxation

The thermodynamic metastability of glasses entails structural relaxation, as an attempt of the system to reach the crystalline equilibrium phase, increasing its configurational order. Such relaxations are associated with significant changes in the physical properties of glasses, such as embrittlement, elastic properties and atomic structure. The potential energy landscape (PEL) is a very useful concept to understand and describe these structural relaxations. Fig. 1.3 depicts a 1-dimensional scheme of the PEL versus configurational coordinates. When a liquid undergoes a glass transition, the system gets trapped in a local minimum of one of the basins, however, the hierarchical configuration of the basins and the broad distribution of energy barriers allow the system to travel along the PEL by means of the different structural relaxation processes (Fig. 1.3(b)).

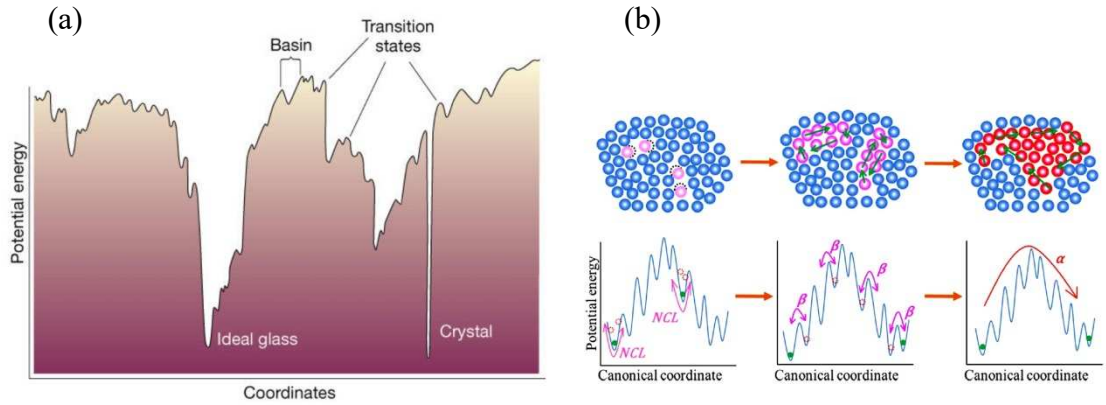

Fig. 1.3) (a) Potential energy landscape of glass forming materials [19]. (b) The hierarchical structure of basins and the atomic rearrangements associated with the different relaxations mechanisms [20]. Notice that Jiang et al. [20] called the Near Constant Loss (NCL) what other authors referred to as the fast β' relaxation [21], [22].

For electrically insulating glasses, dielectric spectroscopy reveals a range of phenomena, intrinsic to the glassy state, spread over a wide range of frequencies (Fig. 1.4). The α relaxation (10^{-6} - 1 Hz) is associated with the glass transition; the β or Johari-Goldstein relaxation (10^{-2} - 10^{7} Hz) is associated with modes in loosely packed regions; the boson peak (10^{12} Hz) is associated with an excess in the low temperature vibrational density of states; and infra-red bands are found at even higher frequency [23]–[25]. Lunkenheimer *et al*. [23] found that there are significant dynamic modes between the β relaxation and the boson peak; in their comprehensive review of glass dynamics, they considered that the discovery of these intermediate fast processes (10^{8} - 10^{11} Hz) was "the most important outcome" of their extended dielectric investigations.

It is now understood that β relaxation in metallic glasses is closely related to the deformation mechanisms, the glass transition, atomic diffusion and the breakdown in the Stokes-Einstein relation, and to crystallization [24], [26], [27]. The fast processes have particular importance because they may be the threshold to β relaxation. In particular, the fast processes may be critical in understanding the onset of plasticity in metallic glasses, and the link between that onset and structural inhomogeneity [28]. The fast processes are stronger relative to the boson peak for glasses formed from more fragile liquids [29] (Using the definition of strong and fragile liquids provided by Angell [8]). Taking the intermediate-to-high fragility of metallic glass-forming liquids into account, fast processes may therefore be significant for metallic glasses.

Understanding these processes and the onset of β relaxation may assist in the design of glasses to optimize properties.

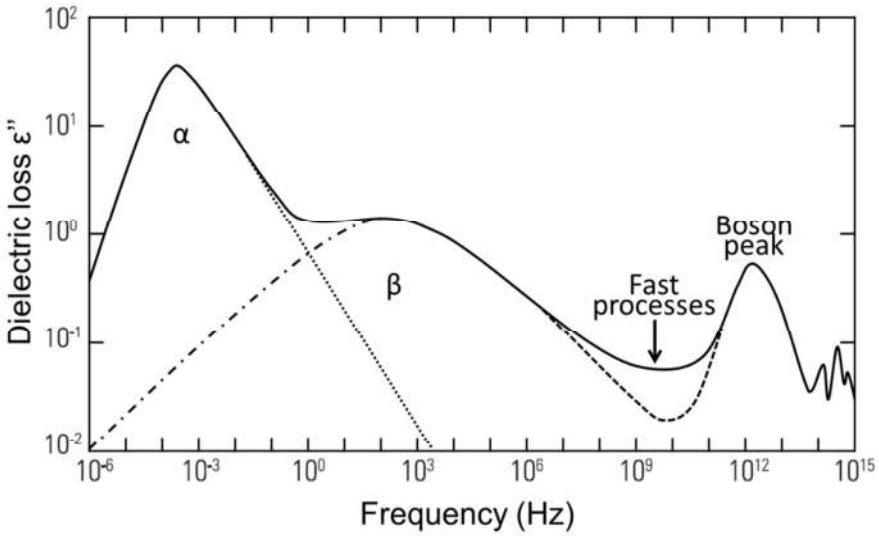

Fig. 1.4) Schematic spectrum of frequency-dependent dielectric loss in glass-forming systems, showing characteristic dynamic modes [25].

Dielectric spectroscopy is not applicable to metallic glasses, which have been investigated using techniques such as dynamic mechanical analysis (DMA), in which characteristic dynamic modes are revealed by peaks in the loss modulus as a function of temperature. There is an α-relaxation peak, and β relaxation is indicated by anything from an excess wing on the α peak, to a distinct β peak [25], [30]–[32]. Recent studies have also found a second fast β' peak [21], [22] and a near-constant-loss mode [20] on the low-temperature side of the β peak. The shifts of loss peaks to higher temperature at higher frequency give the effective activation energy of the modes. For β relaxation in metallic glasses, the activation energy is 26(±2)RTg [24], [27]; for the fast β' and near-constant-loss modes, it is roughly half this value [20]–[22]. In the context of the present work, we note that binary Cu-Zr glasses exhibit β relaxation as a shoulder on the α peak [31].

DMA has a limited frequency range, and is incapable of revealing the boson peak. This has, however, been detected in measurements of low-temperature specific heat of CuZr-based metallic glasses [33], and the boson peak and β relaxation are similarly affected by changes in metallic-glass composition [34]. In the absence of direct

high-frequency spectroscopy measurements, MD simulations have proved to be a useful tool in elucidating structural and dynamic aspects of the boson peak. Jakse *et al*. [35] used MD to simulate a $Cu_{50}Zr_{50}$ (at.%) glass and found a well-defined peak consistent with the specific-heat measurements [33]. They found that the boson peak is associated with the "rattling" of both species of atoms in localized regions of relatively low density and defective structure. The participating atoms vibrate with mean-square amplitudes that are abnormally large and also span a wide range, reflecting the diversity of local coordinations. For the boson peak similarly found in MD simulations of a $Cu_{64}Zr_{36}$ glass, Ding *et al*. [36] focused on the 1% of vibrational modes of lowest frequency. These *soft modes* lie in the region of interest for the fast processes in Fig. 1.4.

1.4) Mechanical properties

Because of their unique structural characteristics the mechanical properties of MGs differ greatly from the conventional crystalline metals. Their superior strength (and fatigue strength), fracture toughness, hardness, elastic limit, elastic energy and resistance to corrosion, oxidation and wear [6], [7] made them the subject of interest for many researchers. Fig. 1.5 offers a comparison of the strength and elastic limit for different materials, where MGs occupy a privileged position, with strengths higher than the steels alloys and an elastic limit similar to polymers.

Nevertheless, these desirable properties are accompanied by their inability to undergo homogeneous plastic deformation. Without a crystal slip plane, the plastic flow is concentrated into shear bands, leading to high flow stresses [37], thus they do not strain harden, causing them to be quite brittle, and to fail catastrophically due to the uninhibited propagation of the bands. MGs exhibit varying degrees of brittle and plastic failure, through intricate fracture patterns, considerably different from that of crystalline solids. Therefore, the understanding of the deformation behaviour taking place in MGs is critical to maximally exploit their benefits, while avoiding their drawbacks as much as possible.

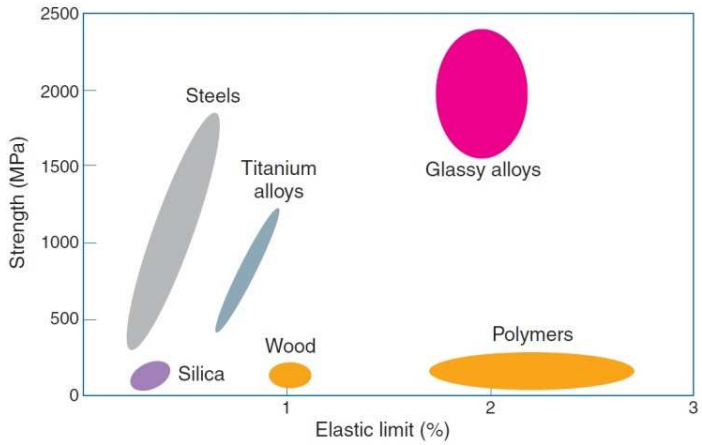

Fig. 1.5) Comparison of the strength and the elastic limit for different materials. MGs possess higher strength than steels alloys while preserving elastic limits characteristic for polymers [38].

Several theories have been proposed to explain the deformation behaviour of MGs. Spaepen [39] considered plastic flow on the basis of the "free volume" model by Cohen and Turnbull [40], where deformation occurs as a series of local atomic jumps into loosely packed regions, thus the macroscopic flow is microscopically triggered by these jumps (Fig. 1.6(a)). The direction of the jumps is aleatory in the absence of external forces but in the presence of a stress field, it becomes biased in the direction of the force causing the stress, leading to a microscopic plastic shear unit. The free volume can be created or annihilated by means of these local jumps and it plays a dominant role in the deformation response of MGs.

In addition, Argon [41] proposed that the accommodation of shear strain in MGs under applied stress occurs at the atomic scale, around free volume regions that have a typical diameter of 5 atoms. He considered two modes of thermally activated shear transformations: one that resembles the nucleation of a dislocation loop, and happens below 0.6 t_g (Fig. 1.6(b)), through inhomogeneous plastic flow and another one, taking place over 0.6 t_g, based on the diffuse rearrangement of atoms involving homogeneous plastic flow.

Later, Falk and Langer, using MD simulations, and based on the ideas of Spaepen and Argon, proposed the deformation process to be governed by Shear Transformation Zones (STZs) [42]. They argued that the MGs response to deformation is viscoelastic at low stresses and viscoplastic above the yield stress. The STZs are small regions, of 5 to

10 molecules, in special configurations that are particularly susceptible to inelastic rearrangements in response to shear stresses (Fig. 1.6(c)). When one STZ creates a localized distortion of the surrounding material, the formations of large planar bands of STZs, called shear bands, are triggered, causing crack growth and fracture of the MG.

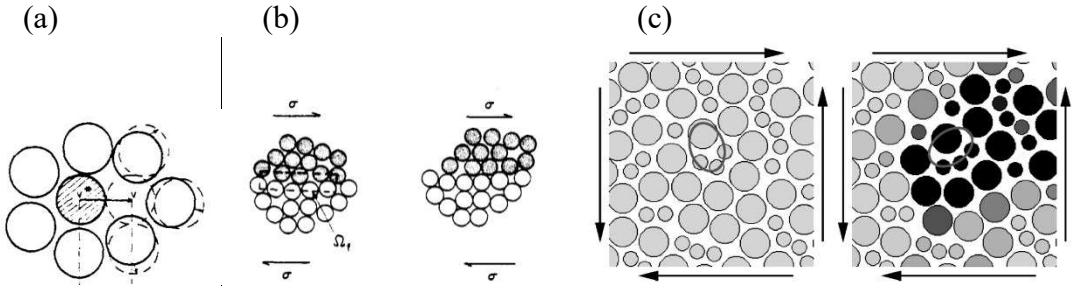

Fig. 1.6). Schematic representations of different deformation mechanisms. (a) Spaepen picture of an individual atomic jump in which free volume is created [39]. (b) Argon mechanism of an intense shear transformation at low temperatures [41]. (c) Falk and Langer figure of a STZ before and after a transformation [42].

Besides the differences in the exposed theories, they are actually very similar in the logical construction and in the underlying physics at a phenomenological level [43], i.e. all of these theories point to loosely packed (or free volume rich) local regions where atoms have an enhanced mobility and the structure is defective, (low content in Full Icosahedral (FI) clusters) as the carriers of the plastic deformation in MGs. Nevertheless, the basic understanding of the structure and mechanical properties of MGs is still very much underdeveloped, especially when compared with the science of crystalline materials, and in fact, understanding the glassy nature and the glass transition have been considered as one of the deepest and most interesting unsolved problem in the solid state theory [44].

1.5) Other properties and applications

Besides the mechanical properties exposed in the previous section, MGs possess interesting electromagnetic properties. They have higher electrical resistivity than usual metals [38], their resistivity temperature coefficient is small, and can be positive or

negative [45]. Additionally, they may possess soft magnetic properties. Their microstructural homogeneity and the absence of magnetocrystalline anisotropy can give very low coercivity and low hysteretic losses [37], they magnetize and demagnetize easily and can operate at high temperatures with minimal flux density reduction [38]. Furthermore, some of the electromagnetic and mechanical properties appear to be correlated [46].

Inoue *et al*. [47] enumerated a rather comprehensive list of fields where MGs have potential applications due to their outstanding properties, i.e. striking-face plates in golf clubs, frames in tennis rackets, various shapes of optical mirrors, casing in cellular phones, casing in electromagnetic instruments, connecting part for optical fibres, shot pinning balls, electromagnetic shielding plates, soft magnetic choke coils, soft magnetic high frequency power coils, high torque geared motor parts, high corrosion resistant coating plates, vessels for lead-free soldering, higher sensitivity type, higher load type and smaller size type pressure sensors in various vehicles including automobiles, Coriolis type liquid flow meters, springs, slat truck covers for airplanes, in-printing plates, high density information storage materials, yoke materials for linear actuators, high frequency antennas, magnetic iron cores for high rotation speed motors, biomedical instruments such as endoscope parts, implants, scalpel blades, etc.

2) Molecular Dynamics simulations

Alder and Wainwright first introduced Molecular Dynamics (MD) simulations in 1957 [48]. They studied the interactions of a hard spheres system with 32 particles and revealed many important properties regarding the behaviour of simple liquids. A few years later, in 1964, Rahman [49] carried out the first simulations using a more realistic Lennard-Johnes potential, for a liquid Argon system with 864 particles. The first MD simulations of amorphous materials, which had results in good agreement with the experimental data, were done in 1975 by Heimendahl and Thorpe [50] and Connel [51]. In both cases, the glassy structures were directly constructed at the objective temperature. MD simulations where the structure was obtained by very rapidly quenching liquid configurations were presented one year later, by Rahman *el at.* [52] for a theoretical system of Leonard-Jones particles, and by Yamamoto *et al*. [53] afterwards, who successfully obtained amorphous Iron with a 686 atoms system quenched at a cooling rate of 10^{11} K/s. Since then, much progress has been made in terms of computing power, and nowadays it is possible to perform MD simulations with billions of particles [54]. Atomistic MD simulations provide a unique insight to study the behaviour of atoms, and are an important tool that allows us to reveal and understand numerous materials' properties, which in many cases are inaccessible otherwise.

2.1) Equations of motion and integrating algorithm

The usual MD approach is a numerical solution of the classical many-body problem. In the classical approximation, quantum-mechanical effects are absent and therefore, these simulations are valid for temperatures greater than the Debye temperature of the material under study and for phenomena requiring times longer than a femtosecond. Under these assumptions MD simulations are based on the Newton's equation of motion:

$$\vec{F}_i = m_i \frac{\partial^2 \vec{r}_i}{\partial t^2} = -\vec{\nabla}_i U \qquad (2.1)$$

Where $\vec{F}_i$ is the force acting on the atom i with mass m_i and position $\vec{r}_i$, and U is the interatomic potential describing the atomic interactions. This equation is then solved for each atom, by using a numerical integration algorithm, such as the Velocity Verlet algorithm [55], which has been proved to be one of the simplest and most efficient ones [56], [57], and it was used for this work. Using the actual position $\vec{r}_i(t)$ and velocity $\vec{v}_i(t)$ of each atom, and its force calculated by applying equation (2.1), it is then possible to calculate the position and velocity that the atoms will have after a small time increment, Δt, by applying the mentioned Verlet algorithm, i.e. equations (2.2) and (2.3):

$$\vec{r}_i(t + \Delta t) = \vec{r}_i(t) + \vec{v}_i(t)\Delta t + \frac{\vec{F}_i(t)}{2m}\Delta t^2 \qquad (2.2)$$

$$\vec{v}_i(t + \Delta t) = \vec{v}_i(t) + \frac{\vec{F}_i(t + \Delta t) + \vec{F}_i(t)}{2m}\Delta t \qquad (2.3)$$

this process can then be iterated to compose long MD simulations. In order to solve these equations for a system with N particles, 6N initial conditions are required. It is possible to use the 3N initial lattice position of the atoms in the system and 3N initial velocities, which can be chosen randomly, following the Maxwell-Boltzmann distribution so that the mean momentum of the atoms corresponds with the target temperature of our system.

The time increment or time step Δt must be carefully chosen [58]. Simulations with smaller time steps will yield more accurate results, but will also need more computational resources to be completed. In this sense, Δt must be small enough to ensure stability and avoid the influence of round off errors, while ensuring that the simulation can be finished in a reasonable amount of time. Generally, a Δt of the order of few femtoseconds is a good choice. Notice that during that period of time, the atomic forces are hypothetically constant.

The output of the aforementioned process is the trajectory of the system in the phase space, i.e. the positions and velocities of the atoms for each time step. These quantities can then be used to calculate some thermodynamic equilibrium parameters such as the temperature, the pressure and the stress, the local density distribution function and dynamic quantities as the phonon density of states, memory functions, etc. For instance, the temperature of the system is calculated as:

$$T = \frac{2}{3Nk_B}\left\langle \sum_{i=1}^{N} \frac{\vec{P}_i^2}{2m_i} \right\rangle \tag{2.4}$$

where k_B is the Boltzmann constant and P_i and m_i are, respectively, the momentum and the mass of atom *i*. The local atomic stress tensor over the volume V, around a particle *i* at position $\vec{r}_i$ can also be calculated by applying the virial stress formula [59]:

$$\sigma_i = \frac{1}{V}\left(-m_i \vec{v}_i \otimes \vec{v}_i + \frac{1}{2} \sum_{j(\neq i)}^{N} \vec{r}_{ij} \otimes \vec{F}_{ij} \right) \tag{2.5}$$

where m_i is the mass of the particle *i* with velocity $\vec{v}_i$, the index *j* runs for the neighbouring particles around particle *i*, located at $\vec{r}_j$. $\vec{r}_{ij}$ is equal to $\vec{r}_j - \vec{r}_i$ and $\vec{F}_{ij}$ represents the inter-particle force applied on particle *i* by particle *j*. The total stress tensor of the system can be computed by adding the stress tensor of each particle calculated through the equation (2.5). Under hydrostatic conditions, the external pressure is a third of the trace of the internal stress tensor of the system [60], i.e.:

$$P = \frac{1}{3}\left(\sigma_{xx} + \sigma_{yy} + \sigma_{zz}\right) \tag{2.6}$$

The external pressure may be similarly computed from the virial theorem[60]:

$$PV = Nk_BT - \frac{1}{3}\left(\sum_{i,j<i}^{N} \vec{r}_{ij} \cdot \frac{\partial \Phi_{ij}}{\partial \vec{r}_{ij}} \right) \tag{2.7}$$

where *V* is the volume, *N* is the number of particles, *T* is the temperature of the system and Φ_{ij} is the interatomic potential between particles *i* and *j*.

2.2) Interatomic potentials

Interatomic potentials are the most important input for MD simulations since they contain all the interactions that will control forces and hence, the positions and velocities of the atoms in the system. In the simplest approach, these interactions occur in a pair-wise base. The interaction must be repulsive at very short distances to resist compression and avoid collapse, and attractive at larger distances to represent the bonding of atoms. A basic example is the Lennard-Jones potential (Fig. 2.1), first proposed in 1924 [61], which has been extensively used in MD due to its simplicity. This potential, however, is not able to account for more complex interactions where the local environment must be taken into account.

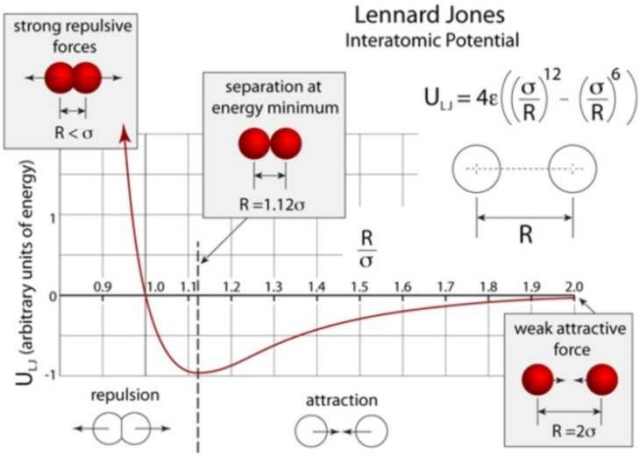

Fig. 2.1) Lennard-Jones potential. The Red line indicates the sum of the repulsion and attraction terms. The separation at the energy minimum, R=1.12σ, indicates the equilibrium distance for a pair of particles [62]. In this plot, σ represents the lattice separation distance and it is used as a normalization factor

In that case, there are better approaches, i.e. the so called many-body potentials, as the Tight-Binding scheme in the Second Moment Approximation (TBSMA) [63] and the Embedded-Atom method (EAM) [64]. In these potentials, the electron density of states in the environment of an atom is calculated from the contributions of surrounding atoms and taken into account for the resulting potential energy, which can be expressed by the following formula:

$$U_i = \frac{1}{2}\sum_{j \neq i} \varphi_{\alpha\beta}(r_{ij}) + F_\alpha\left(\sum_{j \neq i} \rho_\beta\left(r_{ij}\right)\right) \qquad (2.8)$$

where $\varphi_{\alpha\beta}(r_{ij})$ is a short-range pair potential interaction of atoms *i* and *j* (with element type α and β respectively) and F_α is the embedding energy, which is a function of the atomic electron density ρ_β. Notice that, in this way, although the MD simulations method is based on classical mechanics, it can account for quantum effects implicitly, by means of the potential. Because the interaction distance of particles is usually negligible after a certain distance, a cut-off length of the order of a few Angströms is introduced, and interactions beyond that distance are considered to be zero. Both the pair potential and the embedding functions are usually determined empirically from known properties of the materials. In the present work we used a particular EAM potential developed for the Cu-Zr system by Cheng *et al.* [65], which has been proved to reproduce accurately the experimentally measured properties of the constituting elements and their crystalline and amorphous alloys [66], [67]. This potential was developed using the force-matching method [68] by fitting the predetermined PEL (potential energies, atomic forces and stress tensors of the ensembles). The PEL was first studied via VASP [69]–[71] *ab initio* simulations for the crystalline, liquid and glass phases. Cheng *et al.* [65] further refined the generated EAM parameters using a recursive method and the data were compared to a large set of experimental and *ab initio* data. Fig. 2.2 [72] shows the embedded energy, pair potential and density functions as well as the cohesive energy comparing the *ab initio* calculations (points) with the EAM potential (lines). More information about the potential, as well as its parameters can be found in [72].

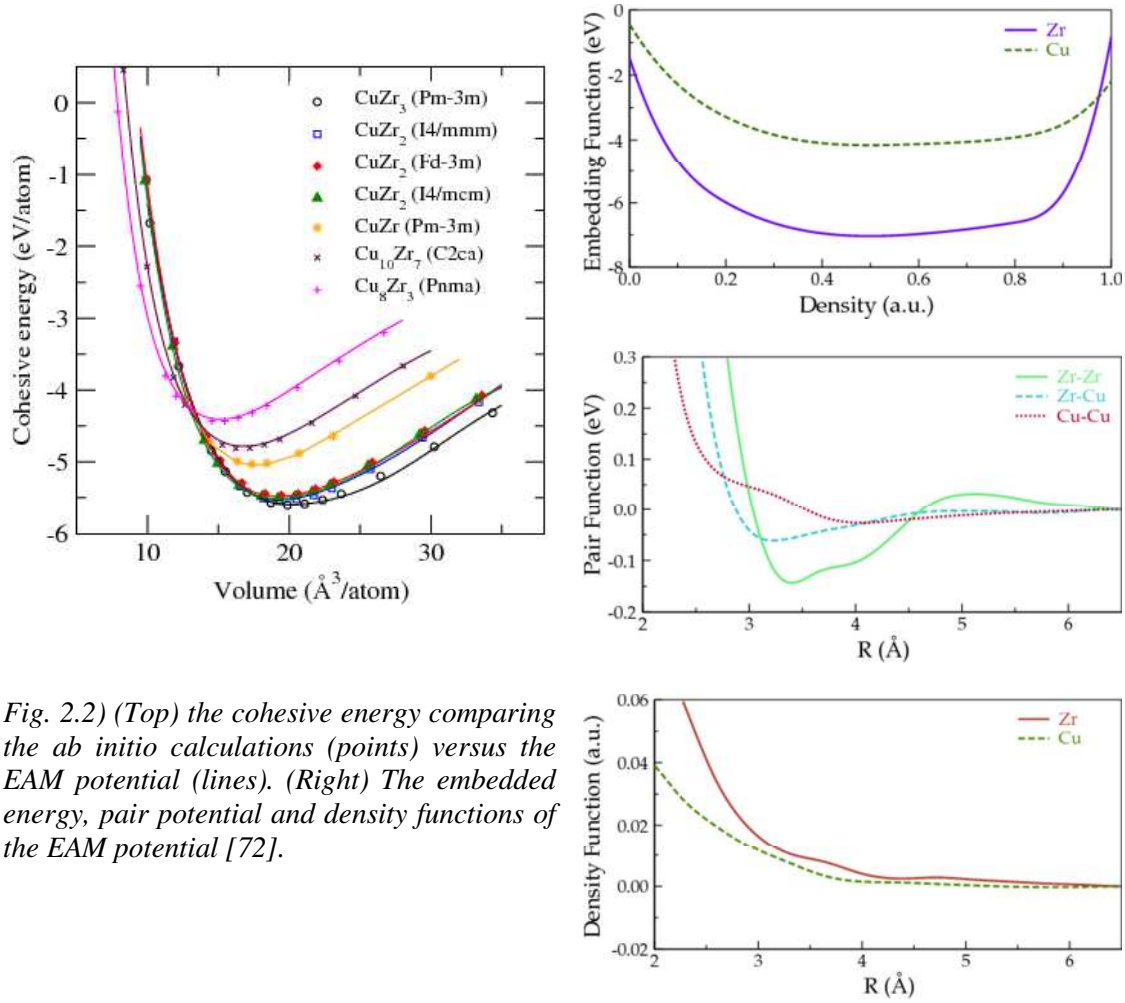

Fig. 2.2) (Top) the cohesive energy comparing the ab initio calculations (points) versus the EAM potential (lines). (Right) The embedded energy, pair potential and density functions of the EAM potential [72].

2.3) Periodic boundary conditions

MD systems can be discretized spatially and run in parallel in several computer nodes, in order to simulate larger ensembles in the same amount of time. Up to date, the largest MD simulation was performed by Eckhardt *et al.* [54], containing $4.125 \cdot 10^{12}$ atoms. Despite the impressive size of their system, the truth is that it is still far below the Avogadro's number ($6.022 \cdot 10^{23}$) of particles that macroscopic systems have, not to mention that the computational resources and time required to run such massive systems are not available to everyone, and in reality, most of the work published nowadays is based on systems containing from a few thousands to a few hundreds of thousands

particles. In such small systems, surface effects can have a great influence compared to their macroscopic counterparts, where only a small portion of particles are close to the surface. In order to eliminate the surface effects in MD simulations, Periodic Boundary conditions (PBC) [73] are applied, mimicking an infinite system and allowing to reproduce the macroscopic behaviour of bulk materials. The use of PBC introduces identical images of the simulation box side by side as shown schematically in Fig. 2.3.

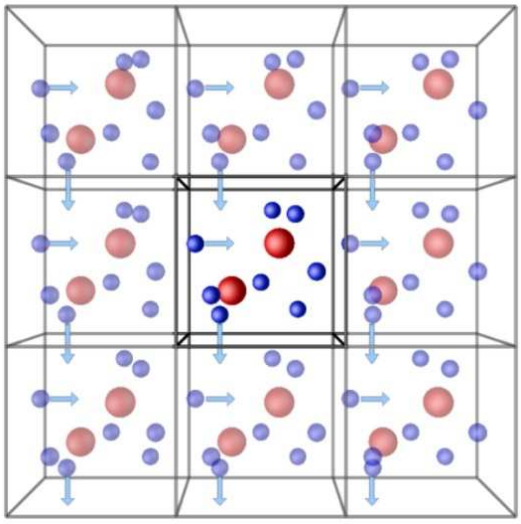

Fig. 2.3) Periodic Boundary Conditions. Images of the simulation box (in the centre) are attached side by side in all dimensions. When a particle leaves the box from one side, it re-enters from the opposite one with the same velocity [74].

Consequently, a particle that leaves the simulation box during the run re-enters it through the opposite side with the same velocity. Additionally, the particles that are near the borders of the box can interact with the particles in the adjacent copy and undesired surface effects can be avoided. Still, the simulation box should be long enough to avoid particles interactions with themselves, which means a minimum box length of at least two times the potential cutoff mentioned in the previous section, known as minimum image convention. Notice that PBC can be imposed in one, two or the three dimensions depending on whether the system under study must simulate respectively a wire, a surface or a bulk material.

Alternatively, it is also plausible to simulate the bulk behaviour and reduce the influence of surfaces by using very large systems and fixing the boundary particles in

their positions. In that case, it is recommended to exclude from the analysis the particles that are near the borders.

2.4) Statistical ensembles. Thermostat and barostat

MD simulations can be run in several statistical ensembles. In the microcanonical ensemble (NVE), a number of particles (N), are contained in an isolated box of volume (V) and therefore the total energy of the system (E_T) is constant. The corresponding Hamiltonian of the system coincides with the total energy and it can be expressed as:

$$H = E_T = K + U = \sum_i^N \frac{p_i^2}{2m_i} + \sum_i^N U_i \qquad (2.9)$$

where *K* and *U* represent the kinetic and potential energy of the system respectively, p_i is the momentum of the atom *i*, and U_i is its potential energy. Under these conditions, the system is isolated from the external environment. For that reason, it is a very useful ensemble for checking the internal stability and the degree of reached equilibration by simply observing how well the total energy is conserved.

When the temperature of the system needs to be controlled, for instance to melt or to cool down the system, the canonical ensemble (NVT) is commonly used. In this case, the number of particles (N), the volume of the box (V) and the temperature (T) are kept constant. To this end, a thermostat needs to be applied. There are several thermostats based on different theories and with different characteristics [75]. For this dissertation, we used the Nose [69] thermostat, for which it has been proved that the resulting Hamiltonian refers to a canonical ensemble [77]. Conceptually, the Nose thermostat introduces an extra degree of freedom, *s*, and its associated momentum p_s, to account for a virtual thermal bath. The Hamiltonian of the system then becomes:

$$H = \sum_{i}^{N} \frac{p_i^2}{2m_i s^2} + \sum_{i}^{N} U_i + \frac{p_s^2}{2Q} + (3N+1)k_B T ln\, s \qquad (2.10)$$

where Q is an effective mass of the thermostat that determines the frequency of the temperature fluctuations, k_B is the Boltzmann's constant and T is the temperature of the thermal bath. If the system is at thermal equilibrium, the value of s becomes approximately one, thus the associated momentum p_s is close to zero and we recover the microcanonical Hamiltonian composed by the kinetic and potential energy of the system. In that sense, deviations from the thermal equilibrium will provoke deviations of s with respect to unity. Still, if the deviations are small, the changes in the value of s are also small. We can take advantage of this property to estimate the equivalent to the kinetic energy of our system in the microcanonical ensemble even when we are using the canonical ensemble. If we subtract from the Hamiltonian, shown in the equation (2.10), the potential energy ($\sum_i^N U_i$) and half the potential introduced by Nosé ($((3N+1)k_B T ln\, s)/2$), the remaining terms represent the equivalent to the Kinetic energy of the microcanonical ensemble (provided, as mentioned, that the deviations from the thermal equilibrium are small). This quantity will be referred to as K_m.

If the pressure of the system needs to be controlled, a barostat can be applied. The barostat adds new terms to the Hamiltonian in a similar fashion as the thermostat, although in this case, it allows the fluctuation of the simulation box size so the system pressure can match the external pressure. For the present work, the Andersen [78] barostat was used. When the thermostat and the barostat are combined, the pressure and temperature of the system are kept constant, which corresponds to the Isothermal-Isobaric ensemble (NPT). In that case, the Hamiltonian has the form:

$$H = \sum_{i}^{N} \frac{p_i^2}{2m_i s^2 V^{2/3}} + \sum_{i}^{N} U_i + \frac{p_s^2}{2Q} + (3N+1)k_B T ln\, s + \frac{p_V^2}{2W} + P_{ext}V \qquad (2.11)$$

where V is the volume of the system and W is the effective mass of the Andersen piston as Q is the effective mass for the Nose thermostat. In this case, the equations of motions become:

$$\frac{\partial^2 \vec{r}_i}{\partial t'^2} = -\frac{1}{mV^{2/3}} \frac{\partial U_i}{\partial \vec{r}'_{ij}} - \frac{1}{s} \frac{\partial s}{\partial t'} \frac{\partial \vec{r}_i}{\partial t'} - \frac{2}{3} V \frac{\partial V}{\partial t'} \frac{\partial \vec{r}_i}{\partial t'} \tag{2.12}$$

$$\frac{\partial^2 s}{\partial t'^2} = -\frac{s}{V} V^{2/3} \sum_i^N m_i \left(\frac{\partial \vec{r}_i}{\partial t'} \right)^2 - \frac{(3N+1) k_B T s}{Q} + \frac{1}{s} \left(\frac{\partial s}{\partial t'} \right)^2 \tag{2.13}$$

$$\frac{\partial^2 V}{\partial t'^2} = -\frac{s^2}{3WV^{1/3}} \sum_i^N m_i \left(\frac{\partial \vec{r}_i}{\partial t'} \right)^2 - \frac{s^2}{3WV} + \frac{1}{s} \left(\frac{\partial s}{\partial t'} \frac{\partial V}{\partial t'} + \sum_i^N \vec{r}_i \frac{\partial U_i}{\partial \vec{r}'_i} \right) - P_{ext} \frac{s^2}{W} \tag{2.14}$$

where:

$$\vec{r}'_i = \vec{r}_i V^{1/3} \qquad t' = \int^t \frac{\partial t}{s} \tag{2.15}$$

3) Characterization Methods

3.1) Radial distribution function

The radial distribution function (RDF), often called *g(r)*, pair distribution function or pair correlation function, is commonly used to characterize the structure of a system of particles and it is particularly useful for liquids and amorphous materials. In general, it is calculated as:

$$g(r) = \frac{1}{4\pi r^2 \rho N} \sum_{i}^{N} \sum_{j}^{N} \delta\left(r - \left|\vec{r}_{ij}\right|\right) \qquad (3.1)$$

where N is the total number of particles in the system, ρ is the density (N/V) and $\vec{r}_{ij}$ is the distance between particles i and j. The summation over the j indexes is actually a histogram of the j particles surrounding particle i, as a function of the distance from particle i, and the summation over the i indexes averages for all particles in the system. For this reason, the RDF is rather a histogram than a function per se. Physically, the quantity $\rho g(r)dr$ represents the "probability" of finding a particle at a distance between r and r+dr, given that there is a particle at the origin of r. Note that this "probability" is not normalized to unity, but instead we have:

$$\int_0^{\infty} \rho g(r) 4\pi r^2 dr = N - 1 \approx N \qquad (3.2)$$

and in fact, the quantity $\rho g(r) 4\pi r^2$ is actually the number of particles in a spherical shell of radius r and thickness dr centred at a reference particle i. The function *g(r)* can also be thought of as the factor that multiplies the bulk density ρ to give a local density, $\rho(r) = \rho g(r)$, about some fixed particle [79]. The *g(r)* is zero when $r \rightarrow 0$ because it is not possible to find a particle at a distance shorter than the particles' diameter, and it tends to 1 when $r \rightarrow \infty$ because it is normalized with the density of the system. An example of a two dimensional configuration of particles and the associated RDF can be seen in Fig. 3.1, where the colour of the particles depends on the distance to the

reference (black) particle and the same colour dependence has been used to separate the different regions in the RDF.

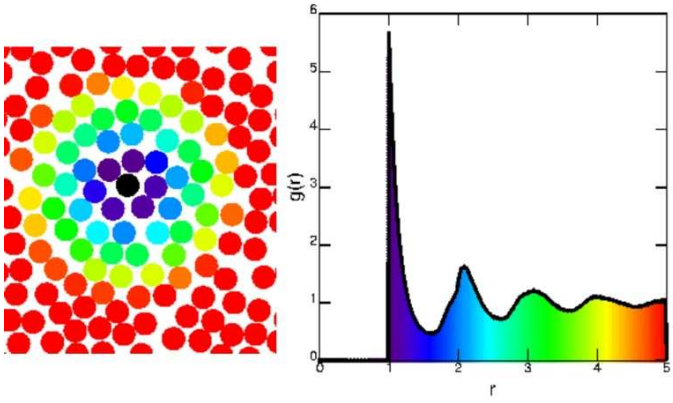

Fig. 3.1) Particles are coloured depending on the distance to the reference black particle. The same colour scheme is used in the g(r) to illustrate the different likelihoods of finding a neighbouring particle at a certain distance, r [80].

So far, no distinction has been done regarding the species of particles *i* and *j* and in this case, the RDF if often called total RDF. However, the RDF can also be calculated between specific pairs of atomic species present in the system (i.e. element types α and β). Then, the RDF is called partial radial distribution function (PRDF) and it takes the form:

$$g(r)_{\alpha\beta} = \frac{N}{4\pi r^2 \rho N_\alpha N_\beta} \sum_{i}^{N_\alpha} \sum_{j}^{N_\beta} \delta\left(r - \left|\vec{r}_{ij}\right|\right) \qquad (3.3)$$

where N_α and N_β are the total number of particles of type α and β. For instance, in the case of a system composed by Cu and Zr atoms, it is possible to calculate the total RDF by not taking into account whether the atoms are Cu or Zr (total RDF) and it is also possible to calculate the PRDF for the different pair combinations (i.e. Cu-Cu, Zr-Zr and Cu-Zr). The total RDF is also a weighted average of all the PRDFs.

The RDF provides statistical information about the atomic ordering, allowing for example, to characterize the different elemental phases. Fig. 3.2(a) illustrates an example for solid, liquid and gas Argon. The maxima indicate the average location of the successive neighbourhoods and the widths of the peaks indicate the average "thickness" of those neighbourhoods. In fact, the first minimum of the RDF is often

used as a cutoff when determining the limits of the first neighbourhood. In addition, the area under the peaks is the average number of atoms in the corresponding neighbourhood, which can be specified by element if the PRDFs are known. The RDF for amorphous systems is quite similar to the RDF of a liquid, which is not surprising, considering that, as we saw in section 1.1), amorphous materials are SCLs very fast quenched into the solid state, thus they retain some of the structural properties of liquids. Fig. 3.2(b) illustrates an example of a typical Cu-Zu RDF for different stoichiometries, obtained by X-rays diffraction (XRD) and Neutron diffraction (ND) methods at room temperature [15].

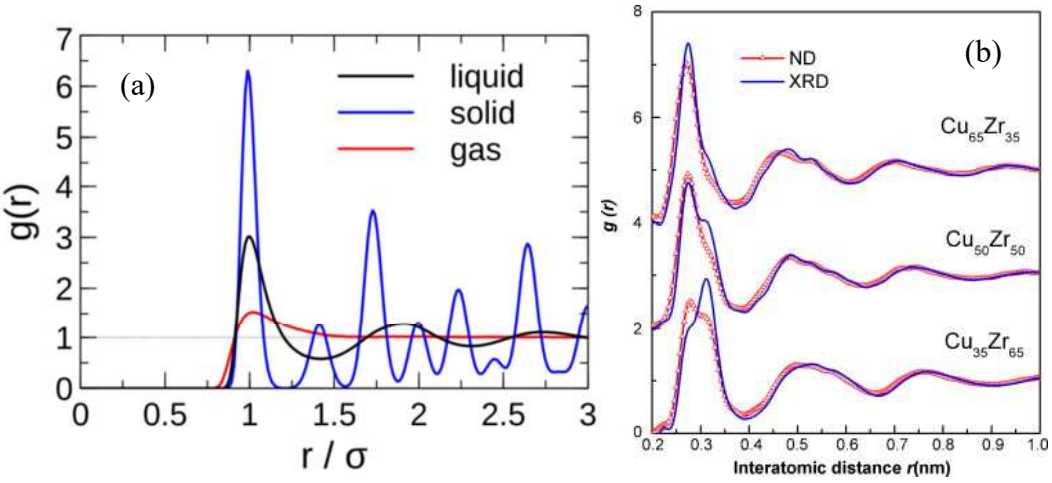

Fig. 3.2) (a) RDF for solid (50 K), liquid (80 K) and gaseous (300 K) Argon [81]. The different phases of matter are clearly distinguishable from the peaks distribution. (b) RDFs for several stoichiometries of amorphous Cu-Zr obtained by X-rays diffraction (XRD) and Neutron diffraction (ND) methods at room temperature [15].

3.2) Voronoi tessellation

The Voronoi tessellation is a method to divide a certain space containing points into regions, where each of those regions is centred on one of those points and the partition is made based on the distance to the surrounding points. It was developed by Georgy Voronoi in 1908 [82] and it has been commonly used in material science in order to analyse the atomic structure. In that case, each atom represents one of the mentioned points, and the region around it represents the cell where the atom resides. The cells are

defined by the intersections of planes drawn perpendicularly to each line that connects the central atom with each of its surrounding neighbours. If the radii of the particles are specified, the distances (from the central atom) at which the planes are drawn are weighted accordingly. Otherwise, the planes are drawn at the bisection of the lines. The region enclosed by these planes defines a polyhedron and its faces are called Voronoi faces (VF). The shape of the Voronoi polyhedron is characterized by the Voronoi indexes: $< n_3\ n_4\ n_5\ n_6\ n_7\ \ldots >$, where n_i denotes the number of i-edged VF. Fig. 3.3 shows some examples of the Voronoi tessellation method. In addition, the volume of the Voronoi polyhedron, called Voronoi Volume, can be considered as a good approximation of the atomic volume for the central atom.

Atoms sharing a VF are considered to be nearest neighbours, and so it is commonly accepted that the number of VF of an atom is equal to its coordination number (CN) [18], [83], [84], which enable the analysis of nearest neighbours without the need of a cutoff distance. However, it is worth noticing that this method does not distinguish between the nearest neighbours and the next nearest neighbours. For example, at atom in a body-centred cubic (BCC) unit cell has eight nearest neighbours and six next nearest neighbours, but its Voronoi index (Fig. 3.3(c)) is < 0 6 0 8 >, which means a CN of 14. In the present work, the Voronoi analysis has been carried out with the Voro++ package developed by C. H. Rycroft [85].

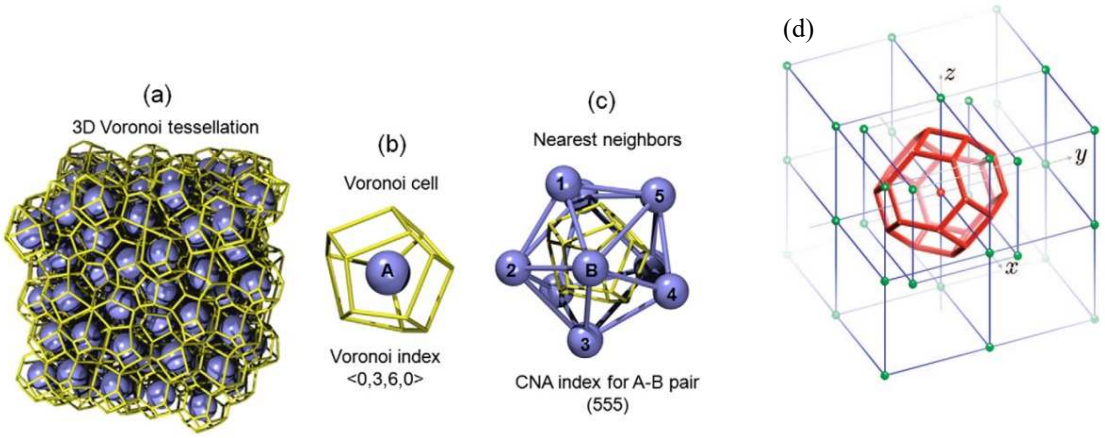

Fig. 3.3) (a) example of 3D Voronoi tessellation. (b) Voronoi cell around the central atom A. The Voronoi polyhedron has 3 faces with 4 edges and 6 faces with 5 edges, so the corresponding Voronoi index is < 0 3 6 0 > (c) the nearest neighbours of atom A. [83]. (d) Voronoi cell corresponding to a BCC lattice with Voronoi index < 0 6 0 8 > indicating a CN of 14 [86].

3.3) Clusters analysis

The Voronoi tessellation is especially useful to analyse the Atomic volume, and to some extent, the CN. However, it is rather strict when it comes to the classification of cluster geometries because small deviations in the arrangement of the atoms can yield quite different Voronoi indexes, and in addition, it is not guaranteed that two geometries are equal just because they share the same set of Voronoi indexes [87]. If, as it happens in reality, there is a considerable amount of truncated and distorted clusters, the number of different Voronoi indexes that are found in the system and their classification can be overwhelming.

In order to obtain information on the possible clusters in the system, including the ones that are distorted and/or truncated, Almyras *et al*. [88] developed a method based on the comparison of model polyhedrons with the atomic topological arrangements present in the system. The cluster analysis procedure considers prototype polyhedrons of 13-atom Icosahedron (ICO), 13-atom Cuboctahedron (CUB), 13-atom truncated tetrahedron (TT) and 15-atom Rhombic Dodecahedron (RD). In addition, they introduced truncated clusters into the analysis, by considering local arrangements where up to 25% of the atoms are missing (i.e. at least 10 atoms for a 13-atoms cluster or 11 for a 15-atoms cluster are enough for the comparison), which increases the number of possible clusters without affecting the results qualitatively. For the analysis, every atom in the system is considered as a possible centre of a candidate cluster. Neighbouring atoms at a distance shorter than a certain cutoff (obtained from the PRDFs) are then selected as nearest neighbours. Finally, the candidate cluster composed by the selected set of atoms is compared with the mentioned geometrical models. For the comparison, they build the function R, which is the root mean square distance between the locations of all atoms of the candidate cluster from the atoms of the prototype clusters. The function R is the objective of a non-linear minimization fitting, during which, the prototype clusters are allowed to rotate and modify their size. The minimum value of R among the prototypes, serves as the criteria to select the best match between the candidate cluster and the different polyhedrons considered. Furthermore, the value of R after the minimization has taken place, provides an estimation of the amount of deformation present in the candidate cluster, in other words, it is regarded as the error of the fit. Fig. 3.4 illustrates some examples of the method. Several topological arrangements of atoms (red balls)

and the prototype cluster with the best fit (blue balls) are shown for an ICO cluster with R = 0.35 Å^2, an ICO cluster with R = 0.53 Å^2 and a RD cluster with R = 0.85 Å^2.

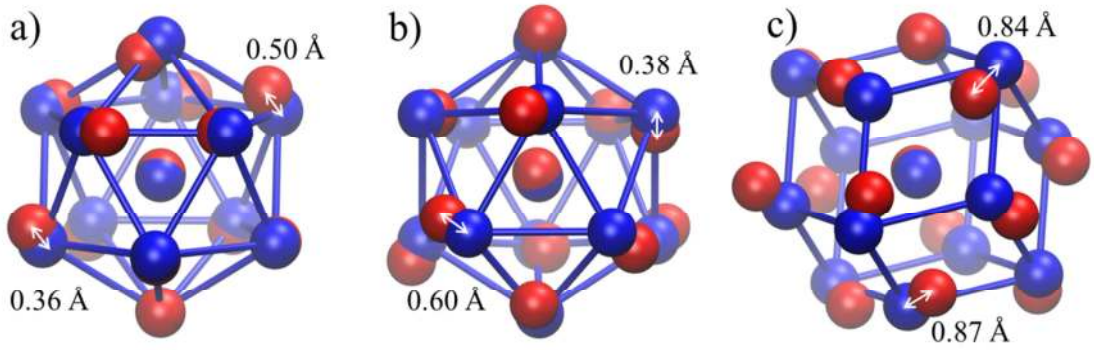

Fig. 3.4) Ball and spoke representations of atoms arrangements (in red) and fitted prototype clusters (in blue). The numbers indicate the distance between the centres of the atoms (white arrows). (a) ICO cluster with R=0.35 Å^2. (b) ICO cluster with R =0.53 Å^2. (b) RD cluster with R=0.85 Å^2.

After the process is done, each atom in the system is assigned a prototype cluster with the corresponding value of R. It is then possible to build histograms for each cluster type, as a function of R (See section 4.2)), including all atoms in the system. This allows for a detailed description of the whole system's microstructure with just a couple of plots and it is one of the biggest advantages of the method over the Voronoi tessellation. Additionally, further classification attending to how well the candidate cluster fits the prototype can be done. For example, ICO clusters could be additionally classified as "perfect" ($R \leq 0.3$), "good" ($0.3 < R \leq 0.6$) or "distorted" ($0.6 < R \leq 0.8$).

3.4) Mean squared displacement

The mean squared displacement (MSD) measures the deviation of a particle position with respect to a reference position over time. It is a common tool to study the dynamics of a system through the average of the individual dynamics for each of the system's particles. It is defined as:

$$MSD(dt) = \langle dr^2(dt) \rangle = \frac{1}{N} \sum_{i=1}^{N} \langle \left(\vec{r}_i(t) - \vec{r}_i(t_0) \right)^2 \rangle \qquad (3.4)$$

Where $dt = t - t_0$ is called the delay (or time interval), the factor $\frac{1}{N}$ together with the sum indicates the average over N particles, the angle brackets represent a time average and $\vec{r}_i(t)$ is the position of particle *i,* at a certain time, *t*.

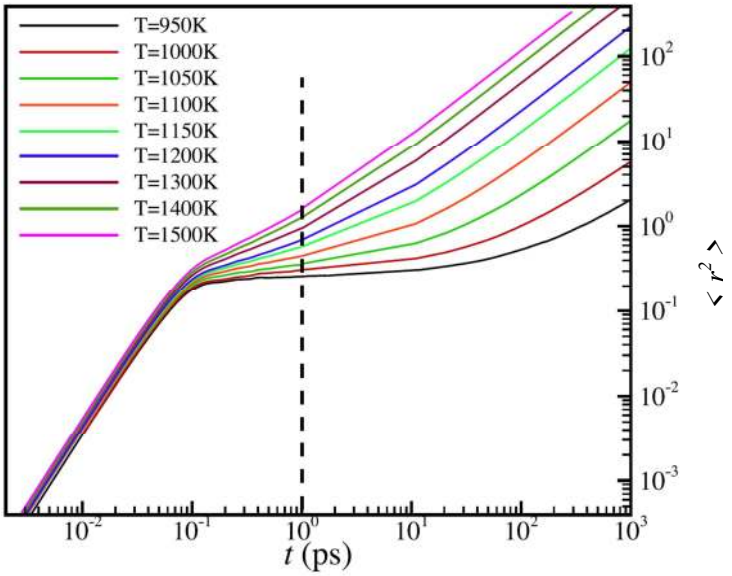

Fig. 3.5) MSD of the $Cu_{64}Zr_{36}$ system, as a function of the delay t, for different temperatures [89].

The MSD dependence on the delay, *dt*, can be modelled as a power law, i.e. $\langle dr^2(dt) \rangle \sim Kt^{\propto}$, where K is a constant. The value of α (the slope in a log-log plot, as in Fig. 3.5) indicates how particles move [90]. A value of α > 1 means superdiffusion. In the special case in which α = 2 (see Fig. 3.5 for dt < 100 fs), the particles move ballistically. If 0 < α < 1, we have subdiffusion. There is another special case in which α = 1, which means than the particles have normal diffusion, also called random walk or Brownian dynamics, typical of the liquid state. A plateau (i.e. α = 0) in the MSD plot, indicates confined movements (particles are moving inside a cage) which is the typical dynamics in solid materials. The upturn after the plateau is an indication of cage breaking [91], [92], i.e. the particles are escaping the cage in which they were confined.

Additionally, the diffusion coefficient, D, can be extracted from the slope of the MSD when $\rightarrow \infty$, through the Einstein equation:

$$D = \frac{1}{2A} \lim_{dt \to \infty} \frac{d}{d(dt)} \langle dr^2(dt) \rangle \qquad (3.5)$$

where *A* is the dimension of the space (i.e. 3 for a 3D system).

For this dissertation, we have used, besides the MSD, a parameter we called "Squared Differences" (SD), which is basically the MSD without the time average:

$$SD(t) = dr^2(t) = \frac{1}{N} \sum_{i=1}^{N} \left(\vec{r}_i(t) - \vec{r}_i(0) \right)^2 \qquad (3.6)$$

In the SD, the reference snapshot with the positions of the particles, $\vec{r}_i(0)$, is fixed and subsequent snapshots after a time *t* are then compared to the reference. While the MSD proportionate information about the dynamics of the system in average during the whole length of the trajectory, the SD proportionate the information about how those dynamics change over time with respect to a certain reference. This becomes very useful and complements the information obtained by means of the MSD when the dynamics of the system evolve with time. For instance, during a long simulation where the system is being strained in the elastic and plastic regimes, the information provided by the MSD is actually an average of the dynamics taking place on those two regimes, while with the SD it is possible to extract the dynamical behaviour of the system during the elastic regime and observe how it evolves when entering the plastic region. However, the SD needs to be averaged over a large number of particles *N*; otherwise the results are too noisy to extract detailed and accurate information. The values presented in this dissertation regarding the MSD and the SD during the strain process, have been calculated considering and removing the affine displacements of the atoms introduced as part of the techniques commonly used to simulate deformation processes.

Additionally, we have used one more indicator defined by Falk and Langer [42] and generally referred to as $D^2_{min}(t, \Delta t)$, which is the local deviation from affine deformations during the time interval $[t - \Delta t, t]$. To calculate this parameter, they defined the quantity $D^2(t, \Delta t)$ as:

$$D^2(t,\Delta t) = \sum_n \sum_i \left(r_n^i(t) - r_0^i(t) - A\right)^2 \quad (3.7)$$

$$A = \sum_j (\delta_{ij} + \varepsilon_{ij}) \times \left[r_n^j(t-\Delta t) - r_0^j(t-\Delta t)\right] \quad (3.8)$$

where the indexes i and j denote spatial coordinates and the index n runs over the molecules within the interaction range of the reference molecule (with index $n = 0$). The value of $D^2(t,\Delta t)$ is then minimized by calculating the strain $\varepsilon_{i,j}$ as:

$$\varepsilon_{ij} = \sum_k X_{ik}\, Y_{jk}^{-1} - \delta_{ij} \quad (3.9)$$

where:

$$X_{ij} = \sum_n \left[r_n^i(t) - r_0^i(t)\right] \times \left[r_n^j(t-\Delta t) - r_0^j(t-\Delta t)\right] \quad (3.10)$$

$$Y_{ij} = \sum_n \left[r_n^i(t-\Delta t) - r_0^i(t-\Delta t)\right] \times \left[r_n^j(t-\Delta t) - r_0^j(t-\Delta t)\right] \quad (3.11)$$

In their work, they claimed that the D_{min}^2 is an excellent diagnostic to identify local irreversible shear transformations and since then, it has been broadly used by many authors to characterize the initiation and propagation on the STZs [28], [36], [93], [94].

3.5) Overlap parameter

The Overlap parameter (Q) is an order parameter designed to compare two different glassy configurations [95]–[100] at times t and t_0. It is defined as:

$$Q(t) = \frac{1}{N}\sum_{i=1}^{N} \theta\left[d - |\vec{r}_i(t) - \vec{r}_i(t_0)|\right] \quad (3.12)$$

Where N is the number of particles, $\vec{r}_i(t)$ is the position of particle i, at a certain time t, d is a threshold or cutoff which depends on the phenomena under study and θ is the Heaviside step function, which is 1 when $d \leq |\vec{r}_i(t) - \vec{r}_i(t_0)|$ and 0 otherwise.

The value of Q goes from 1 (identical particle coordinates within the tolerance of *d*) to 0 (completely uncorrelated configurations). In other words, $1 - Q$ gives the proportion of particles that have moved more than d in a time $t - t_0$. Moreover, it is possible to extract a relaxation time by measuring the time at which the decay of Q reaches the value 1/e, similarly to the case of the self-part of the intermediate scattering function ($F_s(\vec{k}, t)$). In fact, the relaxation times obtained by means of Q and $F_s(\vec{k}, t)$ are very similar [97]. The advantage of Q over $F_s(\vec{k}, t)$ is that for $F_s(\vec{k}, t)$, one needs to specify a wave vector $\vec{k}$, which points at a specific direction whereas in the case of Q, it is enough to choose the cutoff *d*. Indeed, Q is more interesting for materials lacking a well-defined periodic lattice, as it is the case of glasses, because there are no predetermined directions along which the atoms will move, as opposed to the crystalline materials.

The value of Q depends heavily on the cutoff *d*, which is typically of the order of 0.3 Å [95], [97], [99], i.e. above the vibrational amplitude of the particles. In our case, we calculated Q for several values of *d*, which permitted us to obtain different relaxation times as a function of this cutoff. We also applied the Overlap parameter in two different ways, following the distinction we made between the MSD (comparting two configurations separated by a certain time delay, *dt*, and calculating time averages for the whole length of the trajectory) and the SD (comparing each configuration with the reference configuration at time $t_0 = 0$.

3.6) Jumps analysis

So far, we have seen the main tools used to analyse the system dynamics. Although all of these tools are very useful, they generally capture the average dynamics of the system, and it is often complicated to extract any information about local or individual dynamics. Even though these methods are normally applied on an atom by atom basis, the output is very noisy at that level and an average over all atoms in the system is generally required. In this work, we aimed in exploring the individual atomistic dynamics with an acceptable precision and more specifically, to analyse the atomic jumps taking place in the system. Additionally, we required a method that triggered a

clear signal when a jump takes place, allowing us to calculate jumps probabilities and frequencies. Unfortunately, none of the previous tools presented in this chapter is designed to do so.

In order to capture such events, we developed and applied our own method, based on the hypothesis that, if we build a histogram with all the positions that an atom occupies during an interval of time, the shape of that histogram would be Gaussian-like, with its average value situated at the position where the atom spends most of the time, i.e. the equilibrium position around which the atom is vibrating, and with its standard deviation indicating the mean amplitude of the atom vibration. Fig. 3.6(b) shows the mentioned histograms for each coordinate of the atom trajectory depicted in Fig. 3.6(a). Notice that no events are present in the x coordinate of that trajectory, i.e. the atom is not jumping in that coordinate. Once we obtain the histogram, we perform a non-linear minimization fitting to a Gaussian model function. The results are the average and standard deviation of the Gaussian-like distribution, i.e. the equilibrium position and the mean vibration amplitude for each of the atom's coordinates respectively. For non-jumping atoms, the evolution of their three coordinates in time is very similar to the evolution of the x coordinate shown in Fig. 3.6(a) and the Gaussian-distribution of the positions for each coordinate is practically the same as the one depicted in Fig. 3.6(b) that refers to the x coordinate.

If the atom vibrates around two different positions, A and B (as in coordinates y and z in Fig. 3.6(a)), then the histogram would show two peaks, one corresponding to the position A and another corresponding to the position B, indicating that the distribution was actually composed by two Gaussian-like distributions, as it can be seen in Fig. 3.6(b) for the coordinates y and z. In this case, the method is able to separate the two Gaussians-like distributions composing the histogram, and output, as a result of the fitting, two averages and two standard deviations, each corresponding to the each of the two Gaussians distributions. The standard deviation of each of the two Gaussians is then used to set up a threshold for the position, which indicates at any time whether the atom is vibrating around one position or the other. The capture of an event is triggered when the atom crosses the threshold, i.e. when a jump takes place. Notice as well that the areas of the distributions are representative of the probability of finding the atom in each of the two possible positions. In this example, position A is a more stable position while position B is rather metastable. To avoid false signals due to unsuccessful attempts of

atomic jumps (as the one that can be seen in the y coordinate in Fig. 3.6(a) when t ~ 35 ps), we impose a minimum residence time of 1.5 ps. Changes of positions below that time threshold are discarded. In the same fashion, we imposed a distance threshold of 0.6 Å between the two positions in order to consider them for the analysis.

The method as described lacks the ability of fitting more than two Gaussians functions per coordinate. In general, we observed that, at the temperatures at which we performed the analysis, atoms were mostly jumping between two fixed positions, so there was no need to increase the number of Gaussian functions that could be fitted. Atoms having more than two equilibrium position were observed for very large trajectories, but in that case, we split them into shorter ones and analysed them separately, thus reducing the probability of the atoms vibrating around three or more different equilibrium positions. Nevertheless, it would be possible to upgrade the method to include the possibility of fitting more Gaussians, so the jumps for atoms that vibrate around three or more equilibrium positions could be analysed more precisely. Such a modification would decrease the error in the measurements of the jumps and would also permit the application of the program to trajectories at temperatures higher than 600 K, which was the higher temperature of the systems studied in this dissertation.

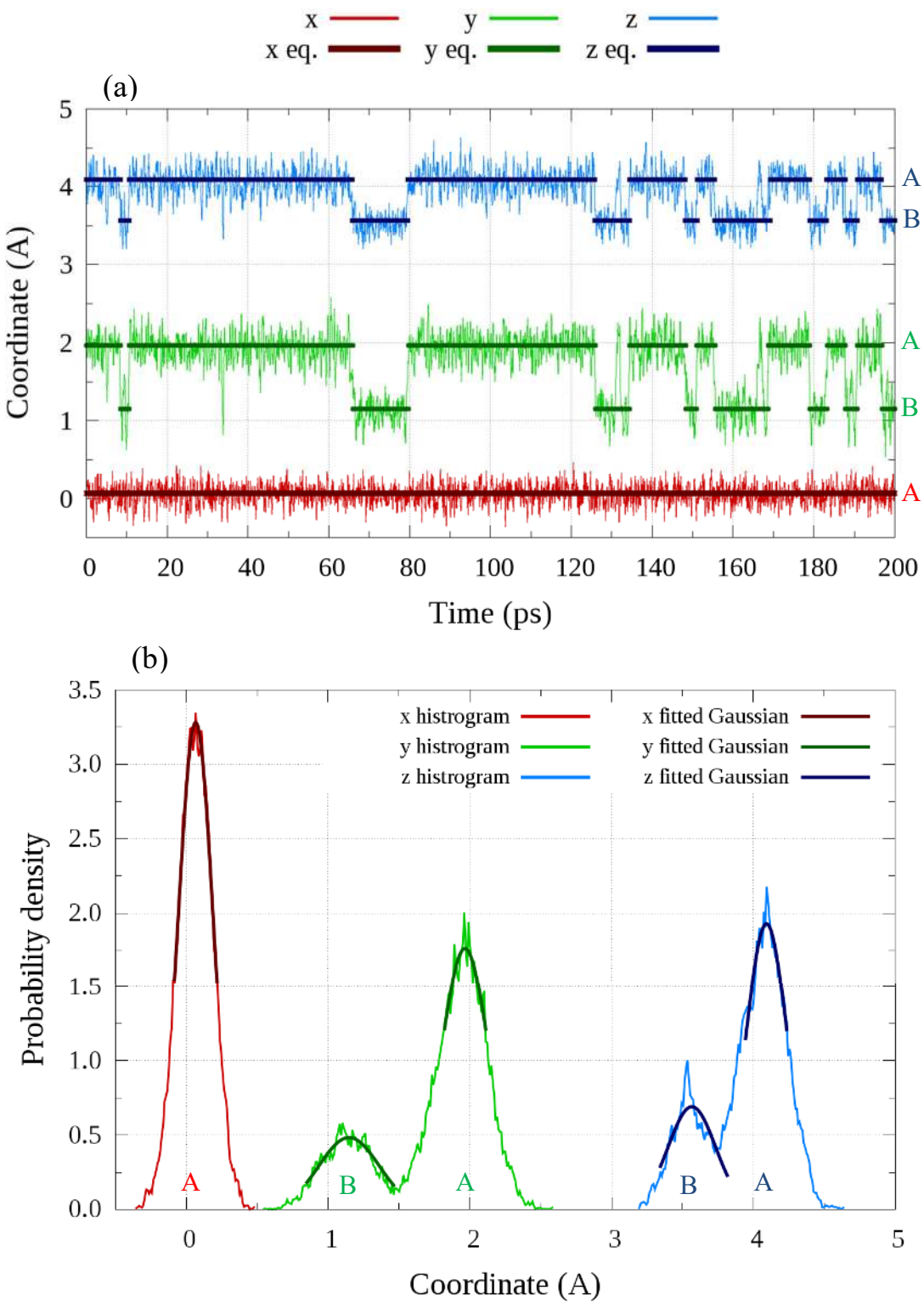

Fig. 3.6) (a) Atomic coordinates vs time of a rattling atom. The atom jumps in the y and z coordinates, but not in the x direction. The lines have been shifted on the y axis to start at 0, 2 and 4 Å, and the labels A and B are used to distinguish the stable and metastable positions respectively. (b) Probability density histograms for each coordinate. Notice the two peaks present in the histograms belong to the coordinates in which the atom is jumping (y and z) and the unique peak in the coordinate in which the atom does not jump (x). The labels A and B correspond to the same labels in (a).

4) The quiescent state

The results presented in this thesis were mostly obtained from two $Cu_{65}Zr_{35}$ (at %) systems quenched at different cooling rates. We will refer to them as the fast cooled system (FCS) and the slow cooled system (SCS). We chose the elements of our model glass to be Copper and Zirconium and the mentioned stoichiometry because of the large amount of data available to compare from experiments and simulations [15], [17], [18], [35], [65], [88], [89], [101]–[107]. These alloys exhibit a relatively good GFA, with a high glass transition temperature, high packing density, high yield strength and low ductility.

4.1) Thermodynamics and simulation details

The first system we prepared consisted of 6000 atoms and PBC in the three dimensions. It was possible to observe atomic rattling, although the statistics of the analysis were not good enough. We increased the number of atoms to 31250, which increased as well the number of observed rattling events, thus improving the statistics. After melting, the systems were kept at 2000 K for 250 ps and then quenched to 300 K in the isobaric-isothermal ensemble (NPT), using a constant cooling rate. The temperature was controlled using the Nosé thermostat [76] and the pressure was kept zero by means of the Andersen barostat [78]. For the FCS the temperature was decreased in steps of 100 K every 50 ps, resulting in a cooling rate of $2 \cdot 10^{12}$ K/s, while for the SCS we dropped the temperature in steps of 50 K every 500 ps, resulting in a cooling rate of $1 \cdot 10^{11}$ K/s. In both cases we used a timestep of 5 fs.

Fig. 4.1 depicts the temperature dependence of the volume during the cooling process for both systems studied. Although their cooling rates differ in more than one order of magnitude, the behaviour is very similar in both cases. Nevertheless, it is still possible to see that the FCS departs earlier from the linear behaviour upon cooling (indicating a slightly higher T_g) and ends up with a slightly larger volume, which translates into a lower density. In fact, the FCS had a density at room temperature of 7.490 g/cm^{-3}, while

for the SCS the density was 7.505 g/cm^{-3}. These results are in agreement with the values reported for the same system by experiments (7.75 g/cm^{-3} [101] and 7.55 g/cm^{-3} [108]) and MD simulations (7.36 g/cm^{-3} [88]). T_g was estimated as the point at which the plots of Fig. 4.1 deviate from the SCL expected volume, i.e. at approximately 750 K for the FCS and 745 K for the SCS. As mentioned in section 1.1), T_g depends on many factors, i.e. the way the glass was prepared, the cooling rate used, etc., and it is possible to find reported values ranging from 737 K [101] to 780 K [109] for the same composition, although most of them are close to 750 K, i.e. 745.3 K [110], 750 K [111] and 753 K [112], again in good agreement with our values.

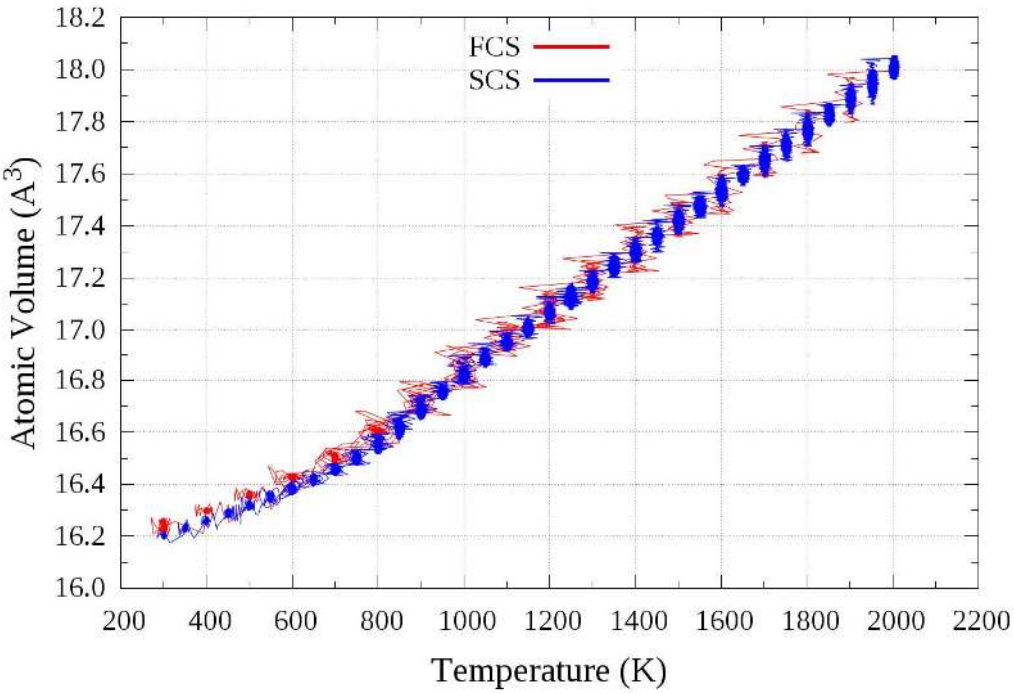

Fig. 4.1) Volume versus temperature upon cooling the system from the liquid state (2000 K) to room temperature (300 K) for the FCS and the SCS. The glass transition, situated at the temperature at which the curves bend, occurs at approximately 750 K for the FCS and 745 K for the SCS. The FCS has a slightly larger volume at 300 K and thus its density is a bit smaller.

After the cooling process, the systems were further equilibrated for 1 ns at 300 K, again in the NPT ensemble. The NPT simulations were followed by another run in the microcanonical ensemble (NVE), which is especially useful for checking whether the systems are well equilibrated or not (see section 2.4)). The timestep was reduced from 5 fs to 2 fs to better conserve the total energy and the simulations lasted 2.5 ns to ensure

sufficient equilibration. The Hamiltonian was constant up to the sixth decimal point over that time, implying variations of less than 0.001% over the nominal value and a good stabilization. At the end of those runs, we saved the atoms' trajectory for 200 ps in the case of the FCS and 1 ns in the case of the SCS, for their analysis, shown in the next section.

4.2) Structural analysis

In the previous section we saw that our systems underwent a glass transition upon cooling. For further confirmation of the glassy structure and the validity of our simulations, we calculated the PRDF for the Zr-Zr, Cu-Cu and Cu-Zr pairs as well as the total RDF, which is a weighted average of all the PRDFs (Fig. 4.2). The PRDFs and the RDF obtained were practically identical, regardless of the different cooling rates used to prepare the glasses, in agreement with the modest differences in volume reported previously in this chapter.

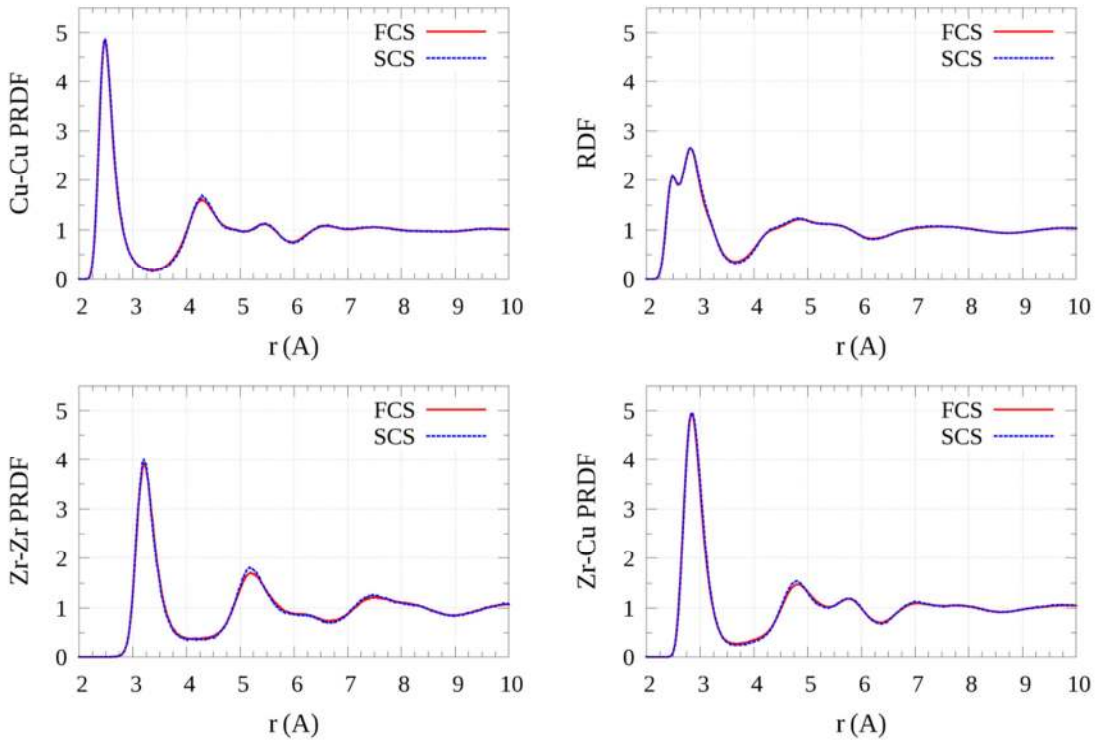

Fig. 4.2) PRDFs for the different pairs of elements and total RDF of the FCS and SCS at 300 K. There is clear evidence of the amorphous state of our simulated systems.

Furthermore, there are clear signatures of the liquid-like structure of our systems, i.e. the broad second peaks and the non-zero minima, and the split of the second peak provided further confirmation of the glassy state [113], which is particularly explicit in the Cu-Cu and Zr-Zr PRDFs. The soundness of our simulations was additionaly estimated by comparing the locations of the first peaks for the different PRDFs with other authors' values, obtained through experiments and MD simulations. Table 4.1 shows that our results are coherent with the expected values found in the literature.

$r_{Zr\text{-}Zr}$ (Å)	$r_{Cu\text{-}Cu}$ (Å)	$r_{Zr\text{-}Cu}$ (Å)	**Method**	**Ref.**
3.21	2.49	2.84	MD	This work
3.17	2.60	2.77	MD	[88]
3.04	2.55	2.72	X-ray scattering	[108]
3.08	2.63	2.75	EXAFS and RMC	[15]
3.12	2.48	2.72	XRD	[101]

Table 4.1) Nearest neighbour distances r_{ij} extracted from the first peak of the PRDFs along with other MD simulations and experimental results.

While the RDF is a key basic tool for the structural elucidation, it only yields a statistical projection of the structure into one dimension but it does not establish a unique description of the atomic configuration in real 3D coordinates. We continue with the inspection of the atomic microstructure by means of Voronoi tessellation and clusters fitting; this analysis yielded that the influence of the cooling rate is noticeable.

A first approach to the SRO of our systems is provided by applying the Voronoi tessellation procedure to one snapshot of the trajectory. Fig. 4.3 shows the most frequent Voronoi indexes separately for Cu and Zr, for the FCS and the SCS, normalized by the total number of atoms in the system. These results are in good agreement with the values reported by other authors by means of MD simulations [18], [83], [114], and differ considerably from the values reported by authors that used RMC

[15], [115], who in general tend to find lower percentages for all atomic configurations compared to the MD simulation results.

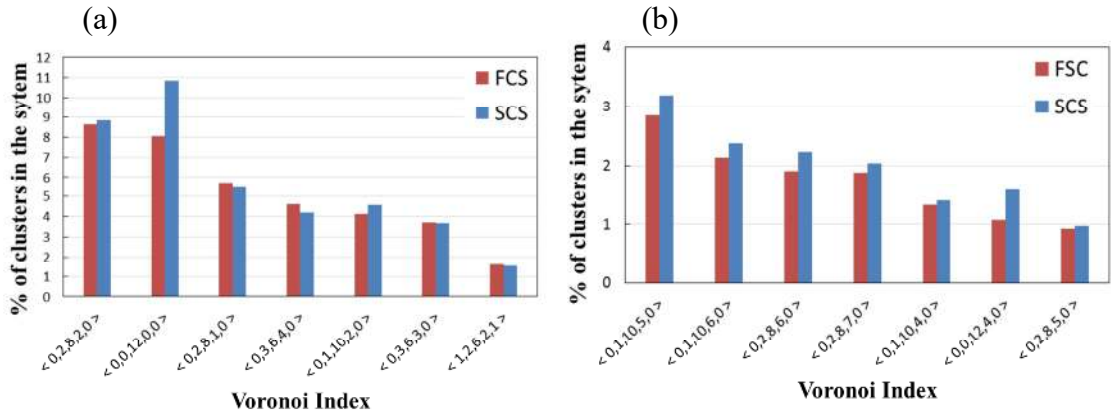

Fig. 4.3) The seven more frequent Voronoi indexes centred on Cu (a) and (b) Zr atoms for the FCS and the SCS. The CNs can be calculated by adding the corresponding Voronoi indexes (see section 3.2)

The first conclusion arises immediately: a slower cooling rate favours the formation of the most common clusters geometries, especially in the case of Zr centred ones and for the Cu clusters with Voronoi indexes (< 0, 0, 12, 0, 0 >), often called Full Icosahedral (FI) clusters. The FI Cu clusters have been well reported and our results for both, the FCS and the SCS, are in line with those presented by Li *et al*. [18], who found a proportion of 7.5% FI Cu clusters using a cooling rate of $6.6 \cdot 10^{13}$ K/s and Cheng and Ma [83], who reported proportions of 16% and 20% for cooling rates of $1 \cdot 10^{11}$ K/s and $1 \cdot 10^{10}$ K/s respectively, indicating the strong influence of the cooling rate regarding the proportion of FI Cu clusters in Cu-Zr alloys, suggesting an even higher proportion of such geometries in glasses quenched at experimental cooling rates. Besides the FI clusters, the most common Voronoi indexes for Cu correspond to the distorted ICO (< 0, 2, 8, 2, 0 >) followed by the truncated ICO (< 0, 2, 8, 1, 0 >), which, along with the rest of clusters types presented in the histogram, are not too affected by the different cooling rates used. In total, the Cu histograms of Fig. 4.3(a) represent 36.4% of the FCS's atoms (56.0% of the Cu atoms) and 39.1% of the SCS's atoms (60.2% of the Cu atoms). The rest of the Cu atoms are categorized in 371 different Voronoi indexes in the case of the FCS and 332 in the case of the SCS, each accounting for a very small fraction of the system's Cu clusters.

In the case of Zr centred clusters, the SCS contains slightly higher proportions for the most common cluster types. However, there is not an obviously dominant cluster type and the fact that the most common geometries appear only in a proportion equal or lower to 3% indicates that there are a lot more other types with even lower fractions. Indeed, only 12.1% of the FCS's atoms (34.5% of the Zr atoms) and 13.8 % of the SCS's atoms (39.4% of the Zr atoms) are represented in Fig. 4.3. The rest of the Zr atoms are categorized in 618 different Voronoi indexes in the case of the FCS and 549 in the case of the SCS, making the analysis of the SRO structure around Zr atoms even more complicated.

Nevertheless, the number of different Voronoi indexes may actually be read as an indication of the degree of SRO present in the system. It is then easy to see that the SCS is more ordered than the FCS, reinforcing the conclusion that the cooling rate has considerable impact in the SRO of the system and anticipating that laboratory made samples, quenched more slowly, would have even higher degrees of ICO order, i.e. they will be much more relaxed.

In addition, the domination of pentagonal faces is remarkable, especially for Cu centred clusters, but also considerable for the Zr centred ones, although in the case of Zr, the number of hexagonal faces (associated with the structural anisotropy [116] and with the formation and activation of STZ [117]) is significant as well. Interestingly, the fivefold symmetry (characteristic of pentagons) is believed to be associated with high packing density and shear resistance which could explain the high strength, modulus, hardness, GFA and lower plasticity reported for this particular Cu-Zr composition [114].

It is worth noticing as well that the CN around Cu atoms (12.23 in average) is clearly lower than around Zr atoms (16.60 in average), which is a consequence of the different atomic sizes: the larger Zr atoms can be surrounded by a higher number of the smaller Cu atoms.

Ding *et al*. [36] characterized the coordination polyhedra in their simulated $Cu_{64}Zr_{36}$ glass, distinguishing well-defined motifs (for example the full icosahedron with Voronoi index $< 0, 0, 12, 0 >$) from geometrically unfavored motifs (GUMs). Unfortunately, they did not provide a unique definition for the GUMs, but rather pointed to some common features shared by these kinds of clusters, i.e. polyhedra that deviates most significantly form the Frank-Kasper polyhedra ($< 0, 0, 12, 0 >$ for Cu and $< 0, 0, 12, 4 >$ for Zr) with unfavourable (too large or too small) CNs. In fact, they

referred to GUMs as all clusters in the system, except for those with the five most common Voronoi indexes for Cu and Zr atoms, but did not provide the total proportion of Cu or Zr GUMs present in their system.

By means of the Voronoi tessellation method it is rather easy to obtain a good approximation of the atomic volume in the system, which is presented in Fig. 4.4 for both, the FCS and the SCS. We used an atomic radius of 1.28 Å for Cu atoms and 1.6 Å for Zr atoms. The histograms were calculated averaging over 50 snapshots and normalized to the bin sized used (0.05) and the number of Cu and Zr in each case. In general, the distribution of the volume occupied by Zr and Cu atoms has a Gaussian-like shape and they do not exhibit significant differences for the cooling rates studied. The average atomic volume for Cu atoms is 12.6 $Å^3$ and for Zr atoms 22.8 $Å^3$ in agreement with Tang *et al*. [102]. The weighted average, taking into account the composition, is 16.17 $Å^3$, which is in very good agreement with the experimental values (15.7 $Å^3$ [101] and 16.0 $Å^3$ [103]) and other MD studies (16.2 $Å^3$ [104], [118]). Notice that both distributions deviate at the tails of the distributions, indicating an excess of atoms with large volumes and a deficiency of atoms with small volumes. This anomaly in the distribution of atomic volumes has not been reported previously and it will be revisited over this dissertation. We will refer to it as the 2STDL and 2STDR areas, i.e. the area of the Gaussians left under and over the average plus two times the standard deviation.

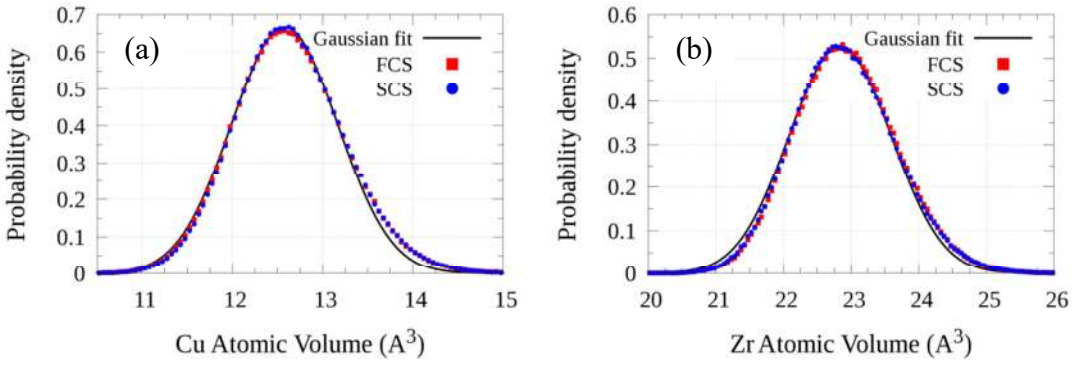

Fig. 4.4) Atomic Volume for Cu (a) and Zr (b) atoms for the FCS and the SCS, calculated by means of Voronoi tessellation, and fitted Gaussians.

Moving forward to the analysis of the microstructure, we now present the results of the cluster analysis. Fig. 4.5 depicts the histograms of ICO, RD and CUB clusters depending on the value of R (see section 3.3)) for the FCS and the SCS and separately for Cu and Zr. In order to smooth out the curves and obtain better statistics, we used 50 snapshots for both systems in the quiescent state. Also, the curves are normalized with respect to the number of atoms in the system, thus the areas under each curve represent the proportion of Cu (or Zr) that are centres of each specific cluster. The exact quantities for each category can be found in Table 4.2.

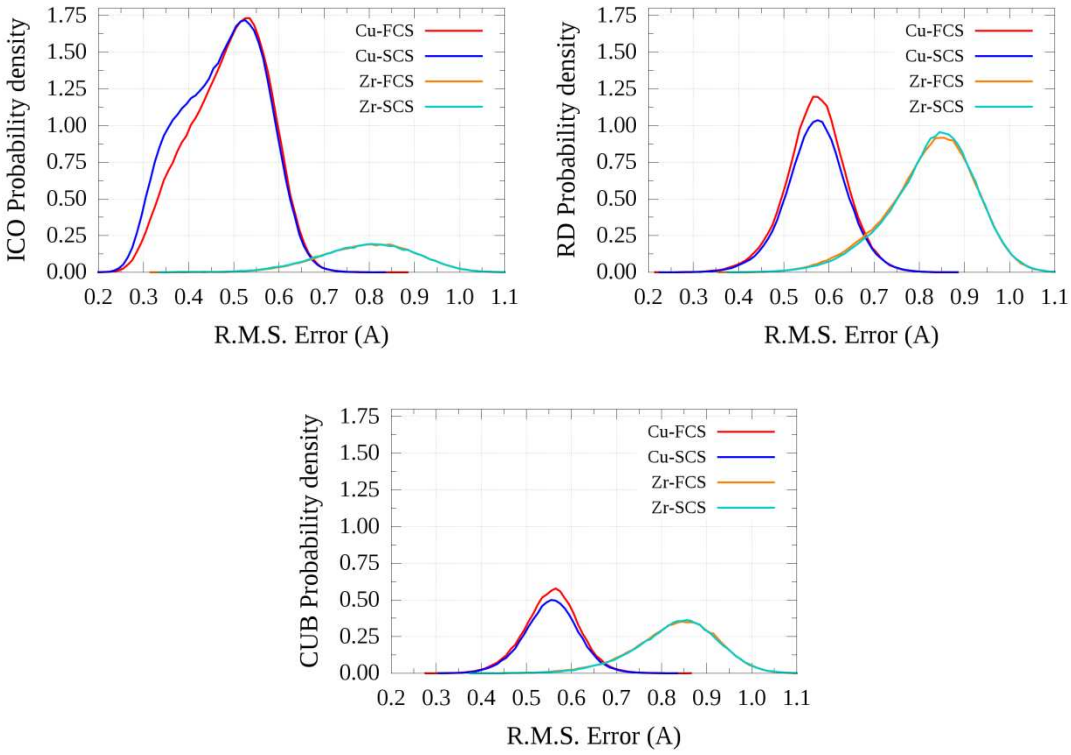

Fig. 4.5) Cluster analysis for the FCS and the SCS separately for Cu and Zr atoms and classified by Cluster type. The area under each graph represents probability.

Several conclusions can be quickly extracted from the plots. The most obvious is again the increase in the number of Cu ICO well fitted clusters (i.e. FI) when the cooling rate is slower, as indicated by the development of a shoulder in the left side of their distribution. Although this increase was already demonstrated by the Voronoi indexes distributions, here we can clearly see how the number of Cu RD and Cu CUB has decreased accordingly, indicating that, in fact, some of these clusters were transformed into ICO when the cooling rate was slower.

In addition, the preferred geometries for each element can be also extracted from the relative areas of each cluster type (see also Table 4.2(b)): Cu atoms form mainly ICO clusters (~60% of the Cu atoms are centres of ICO clusters), then the preferred cluster geometry is RD (with ~25% of Cu atoms at the centre of RD clusters) followed by CUB (with ~10% of Cu atoms as centres). For Zr centred clusters, the RD geometry prevails (with around 60% of the Zr atoms being a centre of an RD cluster), then CUB (with ~20% of Zr atoms forming CUB clusters) and in the last place we have the Zr ICO clusters (with ~15% of Zr atoms as centred of an ICO). These numbers are in agreement with the results previously reported for the same alloy [17], [88], [106]. However, a detailed comparison is not feasible because of the use of different parameters by each author. Nevertheless, the main conclusion is the same: Cu atoms are mostly centres of ICO clusters while Zr atoms tend to form mainly RD clusters and the reason behind these preferences is again the different sizes of Cu and Zr atoms. Bigger Zr atoms are able to accommodate more particles around them, thus the 15-atoms RD clusters are more appropriate than the 13-atoms ICO. In any case, these results support the accepted idea that the MGs are composed of short range ordered structures [119]–[122].

(a) Proportion of each cluster type over all system's Atoms (%)			
FCS	**Cu**	**Zr**	**Total**
ICO	38.3	5.0	43.4
RD	18.5	20.8	39.3
CUB	8.2	7.7	15.9
SCS	**Cu**	**Zr**	**Total**
ICO	41.7	5.1	46.8
RD	16.2	20.8	37.0
CUB	7.1	7.7	14.8

(b) Proportion of cluster types over Cu/Zr respectively (%)		
FCS	**Cu**	**Zr**
ICO	59.0	14.4
RD	28.5	59.5
CUB	12.5	22.1
SCS	**Cu**	**Zr**
ICO	64.2	14.6
RD	24.9	59.4
CUB	10.9	21.9

Table 4.2) Proportion of each cluster type for the FCS and the SCS, separately for Cu and Zr atoms and classified by cluster type.

It is particularly interesting the symmetry degree of some of the distributions presented in Fig. 4.5. While the distributions of Cu RD and Cu CUB are quite symmetrical, this is not the case for Cu ICO. As it has been mentioned before, some proportion of the Cu ICO clusters are expected to be FI, meaning that their error (R) should be pronouncedly small, giving rise to the particular shape on the left side of the distribution. In the case of Zr atoms, all distributions seem to have a longer tail on their left side, pointing to a certain proportion of clusters with abnormal good fitting compared with the average error for clusters centred on Zr atoms.

Finally, we investigated the MRO through the number of Superclusters as explained in section 1.2). It turned out that the number of Superclusters present in the SCS (containing 31250 atoms) was 3490. The evolution of this number will be shown in chapters 5 and 6.

4.3) Dynamics analysis

Crystalline solids have extended defects such as dislocations or point defects like vacancies, i.e. absence of atoms or molecules from certain positions that would normally be occupied. In the latter case, atoms around a vacancy have a certain probability for abandoning their equilibrium location and jump into the empty vacancy space. MGs however, are quite special in this sense because they lack defects such as vacancies, so one would not expect to find these kinds of atomic jumps, especially at low temperatures, in the solid state. Interestingly, we found a certain number of atoms in our systems with abnormally large SDs (Fig. 4.6) and MSDs (Fig. 4.7). Fig. 4.6 shows the SD at the quiescent state for all atoms in the SCS, separately for Cu and Zr and for a specific group of atoms with an SD that deviates considerable from the system average (jumping or rattling atoms). The diffusion coefficient is effectively zero in our system (i.e. a flat SD for long times) and atoms are trapped in cages. The value of dr^2 is approximately 0.08 Å^2, which indicates a vibration amplitude or cage size of $\sqrt{dr^2} = \sqrt{0.08} = 0.28$ Å. The volume in which atoms are confined can then be estimated by adding the cage size to the atomic radius: 1.28 Å for Cu atoms and 1.6 Å for Zr atoms.

This yields a confinement volume of radius 1.56 Å for Cu atoms and 1.86 Å for Zr atoms.

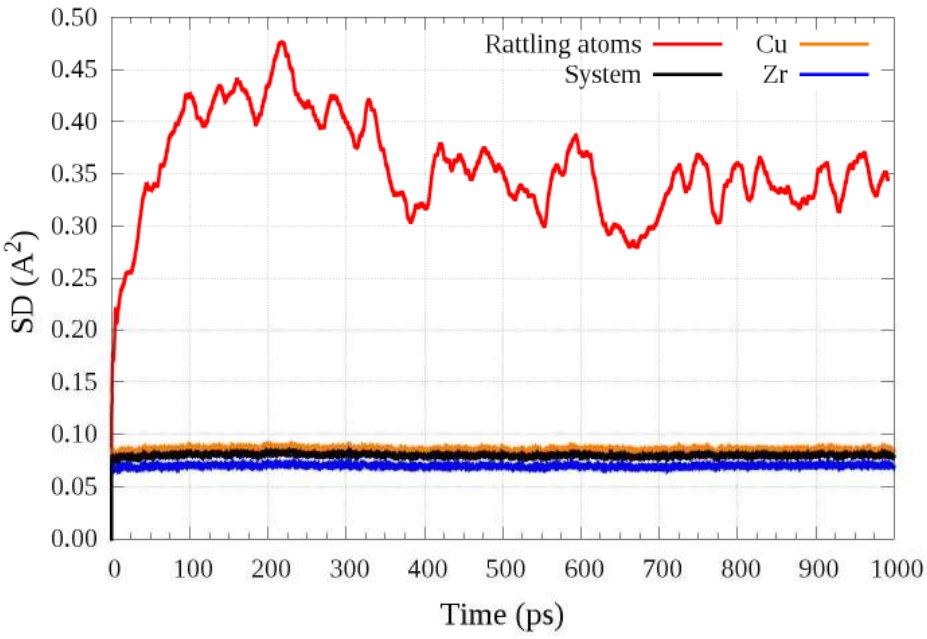

Fig. 4.6) SD at the quiescent state for all atoms in the system, separately for Cu and Zr and for rattling atoms. Atoms in the system are confined in a cage of ~ 0.3 Å, i.e. the average atomistic vibration amplitude.

Due to the small number of rattling atoms, the SD is very noisy and the MSD needs to be calculated. The MSD for rattling atoms is shown in Fig. 4.7. In average (green line in Fig. 4.7) it looks like the rattling atoms are diffusing. However, when we classify the rattling atoms by considering whether they jump more or less than 1 Å, it is possible to see that actually, atoms jumping less than 1 Å are indeed confined in a cage. Very interestingly, the value of dr^2 at the plateau is approximately 0.3 Å^2, which coincides with previously reported values for temperatures of 900 K and 950 K [89], [123], [124], implying that the jumping atoms are actually located in regions that resemble the liquid-like regions that other authors have reported and linked with high-mobility atoms and a defective (non ICO) structure [18], [107]. The cage size in the case of the jumping atoms is approximately 0.55 Å, which is almost double the value we found when we considered all atoms in the system (0.3 Å). Atoms jumping more than 1 Å are actually diffusing with a diffusion coefficient of $2 \cdot 10^{-8}$ cm^2/s, which, although it is on the limit of our accuracy, is again comparable to values obtained by other authors at temperatures of 900 K and 950 K [89], [123], [124]. Moreover, it is also clear that most of the rattling

atoms jump less than 1 Å, as indicated by the difference between the green and blue lines compared with the difference between the green and red lines). The SD of the system is also plotted for reference purposes.

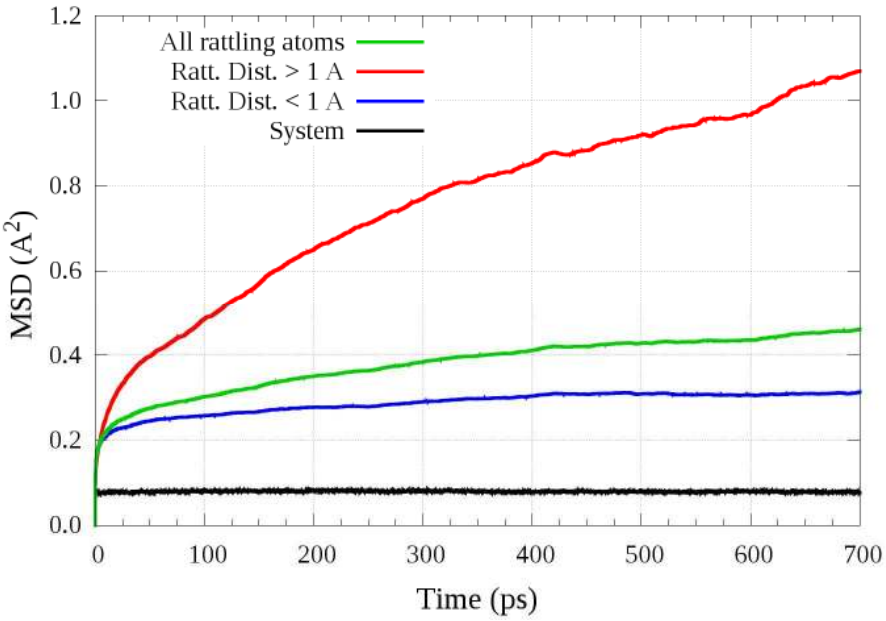

Fig. 4.7) MSD for all the rattling atoms, separately for atoms that jumps more or less than 1 Å. The system SD is also plotted for reference. Atoms jumping more than 1 Å diffuse with diffusion coefficient of $2 \cdot 10^{-8}$ cm^2/s, while atoms jumping less than 1 Å are confined in a cage of radius ~ 0.56 Å)

Subsequent examination of the rattling atoms' coordinates versus time yielded a key finding, depicted in Fig. 4.8: for some atoms there is a clear alternation between two positions at each of which, there is vibrational motion. The time dependence of atomic position seen in Fig. 4.8 is quite distinct from that found by Jakse *et al*. [35] while studying the boson peak, over very similar timescales and at the same temperature (300 K). In contrast with a crystal, the metallic glass does not have a lattice with well-defined equilibrium positions. As a consequence, the rattling between two sites shows a wide distribution of distances (from 0.1 to more than 1.5 Å) and life-times (from 1.5 to more than 100 ps). This distribution is wider than the range of amplitude (0.3-0.6 Å) found by Jakse *et al*. [35] to contribute to the boson peak. As it is emphasized in Fig. 4.8. The motion is to-and-fro; consequently the net mass flow is practically negligible. The rattling process revealed in Fig. 4.8(a) is shown with better time resolution in Fig. 4.8 (b). The alternation in atomic position is accompanied by changes in local

coordination: the polyhedron around the rattling atom alternates between ICO and RD or CUB states as the atom moves to and fro.

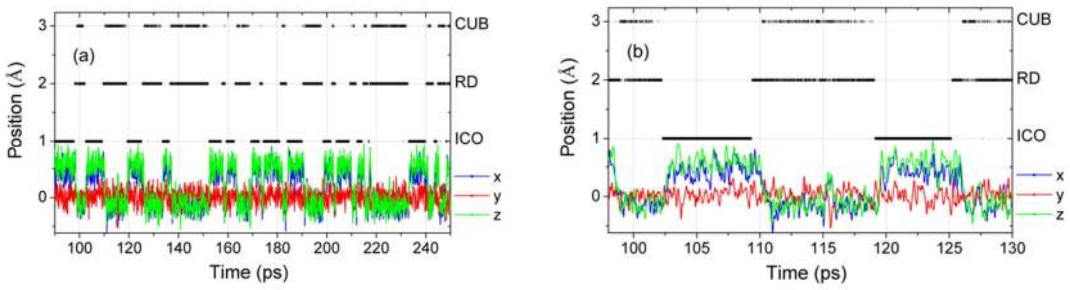

Fig. 4.8) (a) The time evolution of a representative atom's coordinates x, y and z, demonstrating rattling motion at 300 K. The bars at the top indicate the character of the atomic coordination polyhedra: icosahedral (ICO), rhombic dodecahedral (RD) and cuboctahedral (CUB). (b) Close-up view of the rattling motion shown in (a).

It is remarkable that such rattling motions (with some amplitudes exceeding 1.5 Å) can occur, given that metallic glasses are so densely packed. There are no vacancies in metallic glasses, and their structure is considered to consist of efficiently packed clusters as we saw in the previous section. Our MD simulations do, however, reveal how such large-amplitude rattling is possible. Fig. 4.9 shows atomic sites (with vibration eliminated) in a local region. This shows that two or three neighbouring atoms can perform concerted motions to accommodate large-amplitude rattling. In state 1 (Fig. 4.9 (a)), atoms A and B, separated by 3.8 Å, are the central atoms in two touching (i.e. face-sharing) polyhedral clusters. In the rattling, atoms B, D, A and C have coordinated displacements of about 1 Å, comprising a string-like movement. Atom F is displayed in white because it was a neighbour of atom B in state 1, but it is not its neighbour in state 2, after atom B rattles to its other site. In the next stage (Fig. 4.9 (b)), atom A does not move, while atom B returns to its initial location, and atom F becomes again part of its first-neighbour coordination shell. In this transition, five more atoms adjust their positions through small movements of the order of 0.3 Å. Finally (Fig. 4.9(c)), atom A returns near its initial location, followed by atom C. The movement is facilitated by atom D that moves downwards, followed by atom B. Again, a string-like movement can be identified. The atoms A and B are now first neighbours, at a distance of 2.7 Å, their two clusters are interpenetrating (i.e. the central atom of one is in the first-neighbour

shell of the other) and atom F is not anymore a nearest neighbour of atom B, showing how the local structure of nearest-neighbour polyhedra has changed through the coordinated rattling motion.

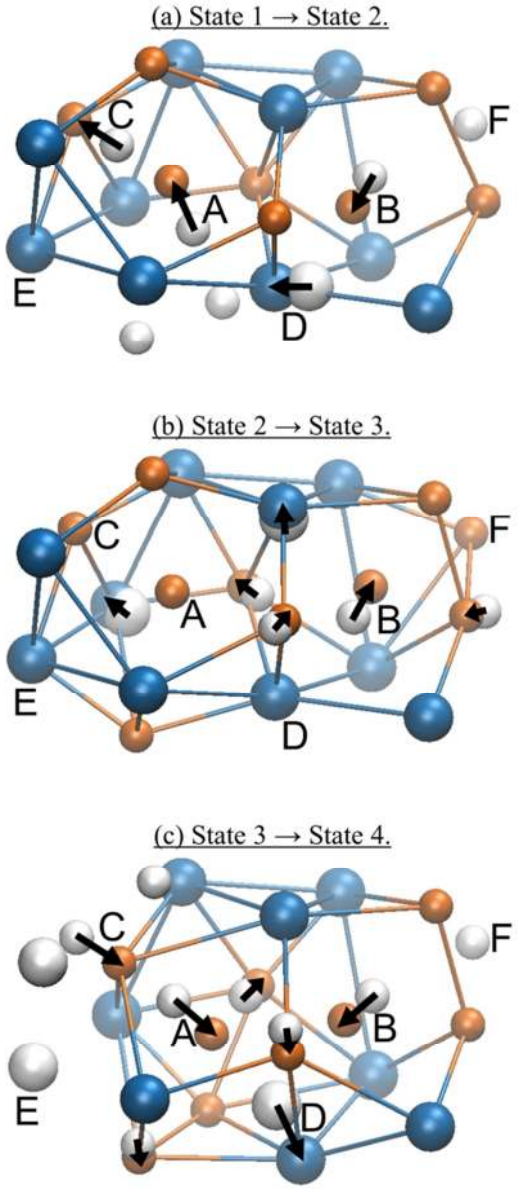

Fig. 4.9) Ball-and-spoke representation of a particular rattling event. In this region of the Cu65Zr35 glass, four states separated by tens of ps, are represented through three inter-state plots: a (from State 1 to State 2), b (from 2 to 3), and c (from 3 to 4). White spheres represent atomic positions 'before' (i.e. State 1 in plot a) and atoms that do not belong to the neighbourhood of the central atoms A and B. Coloured spheres (Cu in orange and Zr in blue) represent atomic positions 'after' (i.e. State 2 in plot a). Lower colour saturation indicates depth. Black arrows indicate the movement direction. (a) From State 1 to State 2: A and B are the central atoms of two face-sharing clusters. Atoms B, D, A and C participate in a rattling movement of about 1 Å, involving a string-like sequence. (b) From State 2 to State 3: neighbouring atoms readjust their positions through small movements of the order of 0.3 Å and atom B comes back to its initial position. (c) From State 3 to State 4: a different string-like sequence of movements can be identified. Atoms A and B are now first neighbours, and the coordinated rattling movements have changed the local atomistic structure.

To characterize the extent of the rattling throughout the system, we counted the total number of events, considering one event as the alternation from one site to another and back. Imposing a minimum distance of 0.6 Å and a minimum residence time of 1.5 ps, we calculated the frequency of occurrence (FOC) of rattling, normalizing the number of events with respect to the number of atoms in the system. The result was a FOC of 435 MHz at 300 K in the case of the FCS and 231 MHz for the SCS (Fig. 4.10). Although in

both cases, these frequencies are in the transition region between β-relaxation and the fast processes in the Lunkenheimer plot [23], the FOC in the SCS is half than in the FCS, demonstrating a considerable influence of the applied cooling rate during the glass creation.

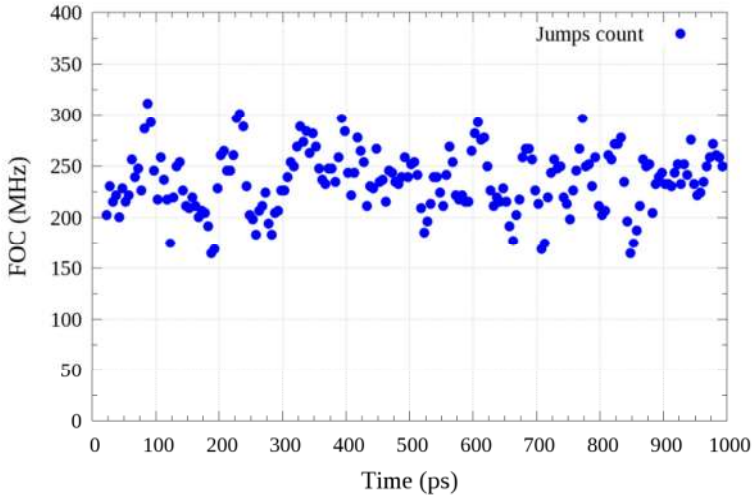

Fig. 4.10) Histograms of the Rattling movements vs time at the quiescent state for the SCS. The number of jumps is approximately constant in time and the FOC has a value of 231 ± 8 MHz.

Importantly, although the atoms performing rattling movements come back to their initial positions, showing reversibility, their neighbouring atoms may change positions, thus inducing local structural alterations. To quantify this, we performed an analysis of all the atoms involved in rattling in the quiescent glass (i.e. not subjected to any external load). About 8% of all events induced irreversible changes in the neighbourhood of the moving atoms, thus resulting in persistent local structural changes (Fig. 4.9 (c)).

Noting that the boson peak is associated with more loosely packed regions [35], we examine whether the rattling atoms in the present work show a similar association. To this end, we calculated the Voronoi Volume occupied by the rattling atoms in the same fashion as we did in the previous section. In both, the FCS and the SCS, the atomic volume around the rattling atoms is larger (by 1% for Cu and 1.5% for Zr in the FCS and by 1.8% for Cu and 0.5% for Zr in the SCS) than the average atomic volume in the system (Fig. 4.11). Of all atoms in the system, only 1.1% performs rattling motions, 1% of them being Cu and 0.1% being Zr in the FCS. In the SCS, 1% of all atoms in the system perform rattling motions, from which 0.9% are Cu atoms and 0.1% are Zr

atoms. The dominant role for the smaller atomic species is consistent with the link proposed [26] between the β-relaxation mode in metallic glasses and the self-diffusion of the smallest constituent atoms.

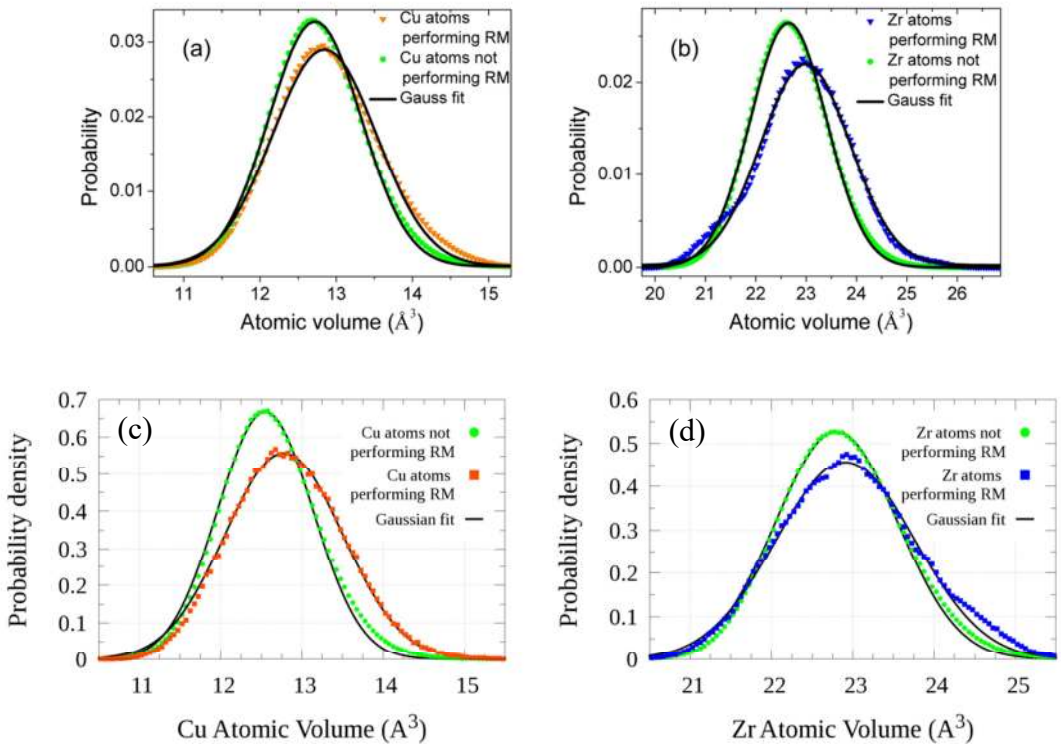

Fig. 4.11) Atomic volume, from Voronoi tessellation, around the atoms performing rattling motions (RM) and around the rest of the atoms in the system (green) for the FCS (a and b) and for the SCS (c and d). The solid black lines are fitted Gaussians.

We have demonstrated that the rattling atoms occupy a larger average volume than the non-rattling atoms. Following the characterization of polyhedra performed by Ding *et al*. [36], we proceeded to the calculation of the fraction of rattling atoms that are centres of the non-well defined motifs, i.e. the GUMS described the previous section. Using the FCS, we found that the fraction of Cu atoms at the centre of GUMs is 65% overall, but is 80% for those participating in rattling. The equivalent fractions for the Zr atoms are 80% and 90%. Thus, the rattling atoms are almost exclusively at the centres of GUMs, an even stronger association than that between soft modes and GUMs [36].

The rattling atoms are not homogeneously distributed. Instead, they are gathered together, forming regions which vary widely in size and number of atoms (Fig. 4.12). Given that rattling is concentrated in specific regions, it is interesting to consider the

frequency in terms of only the moving atoms; this is distinct from the FOC noted earlier, which was normalized with respect to all the atoms in the system. Normalizing with respect to the rattling atoms only, we obtain the frequency of the mechanism (FOM), which at 300 K yields a value of the order of 40 GHz for the FCS and 50 GHz for the SCS, indicating small dependence on the cooling rate and falling exactly where fast processes are expected [23].

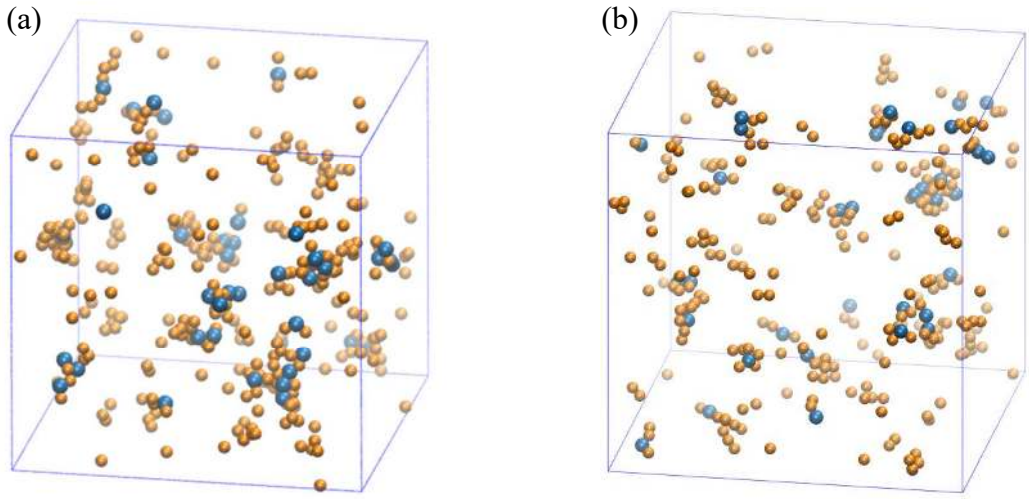

Fig. 4.12) Representative distribution of the rattling atoms (Cu in orange and Zr in blue) in the simulated glass. The cubic box represents the simulation boundaries and weaker colour indicates that the atoms are closer to the back of the box. Only 1.1% of the total atoms in the FCS (a) and 0.95% in SCS (b) perform rattling movements. The rattling atoms are inhomogeneously distributed in loosely packed regions.

In order to further investigate the relationship between the atomic rattling and the different relaxation modes present in MGs and described in section 1.3), we calculated the activation energy of the rattling events and compared it with the reported values for each mode. To that end, we equilibrated our systems at 200 K, 400 K, 500 K and 600 K and we proceeded by counting the atomic jumps as described before, thus obtaining the corresponding FOC and FOM for each system as a function of temperature, below T_g.

Interestingly, it came out that the FOM shows little or no dependency with temperature and remains at around 40~50 GHz for the studied temperature range and cooling rates, supporting the idea that the FOM, which should be regarded as the atomic frequency at which the rattling atoms oscillate between their two equilibrium positions, is indeed

intrinsic of the fast processes mechanism. On the contrary, the FOC, which should be regarded as the probability of having rattling events in the system, it is temperature dependent, rising exponentially as the temperature increases. In such a scenario, is then possible to model the FOM by an Arrhenius equation and to obtain the activation energy for the mechanism. In our case, the Arrhenius equation is formulated as:

$$f = f_0 e^{\frac{-E_a}{k_b T}} \tag{4.1}$$

where f is the FOC, f_0 is the pre-exponential factor and represents the maximum possible FOC of the rattling atoms, k_b is the Boltzmann constant, T is the temperature and E_a is the activation energy of the mechanism. Taking the natural logarithm on both sides of eq. (4.1) yields:

$$ln(f) = \ln(f_0) - \frac{E_a}{k_b T} \tag{4.2}$$

Consequently, plotting the natural logarithm of the FOC versus the inverse of the temperature (Fig. 4.13), should result in a straight line with a slope of value: $\frac{-E_a}{k_b}$. We found activations energies of 66 meV and 64 meV for the FCS and the SCS respectively, indicating a small dependency on the studied cooling rates.

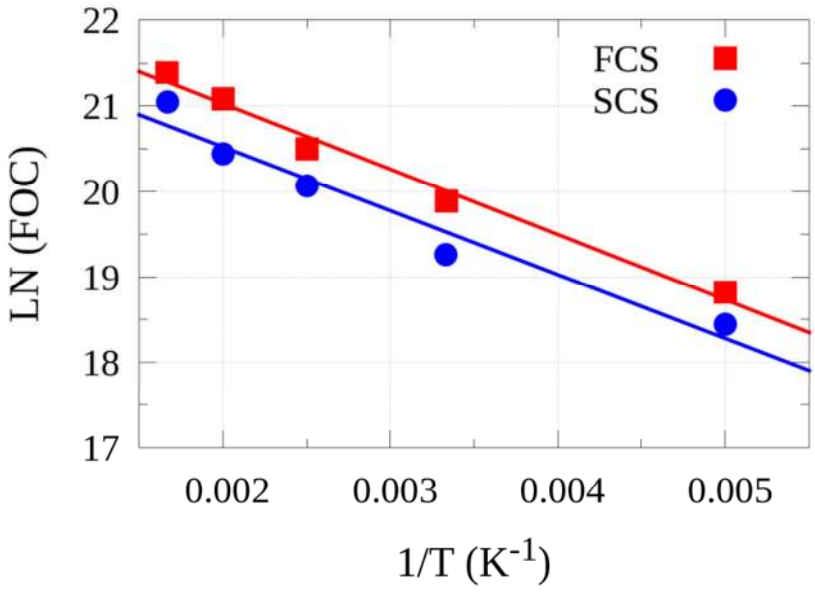

Fig. 4.13) Arrhenius plot for the natural logarithm of the FOC vs temperature for the FCS and the SCS and fitted straight lines.

Fig. 4.14 represents an example of the variations on the potential energy of the system while a rattling movement is taking place. To obtain this figure, we performed the following procedure: first, we selected a rattling atom and localized the two positions around which it was rattling. These positions were situated 1.0 Å away from each other: the more stable position, A (located at 1.0 Å in the x axis of Fig. 4.14) and the metastable position B (located at 0.0 Å in the x axis of Fig. 4.14). Second, we fixed the location of all atoms in our simulation box, aiming in eliminating the noise of the potential energy induced from the other atoms of the system. Finally, we manually moved the rattling atom, following a straight line from position B – 0.2 Å to position A + 0.2 Å, in steps of 0.05 Å. We started at position B – 0.2 Å in order to capture the left potential barrier, i.e. the first 5 points in Fig. 4.14 (the value of the potential energy was then shifted to start at 0). Similarly, we ended the movement at position A + 0.02 Å to capture the right potential barrier i.e. the last 5 points in Fig. 4.14.

After each step in which we moved the rattling atom 0.05 Å, we performed energy minimization, in which we allowed the 50 closer atoms to the rattling one to find their lowest energy positions. The procedure yielded potential energy barriers of 20 meV and 40 meV, as depicted in Fig. 4.14. The values of the potential energy barriers are of the same order as the average activation energy obtained through the Arrhenius fit performed in Fig. 4.13 and moreover, Fig. 4.14 matches very well the representative plots of the β relaxation process depicted in Fig. 1.3(b) and also in the literature [24], [34].

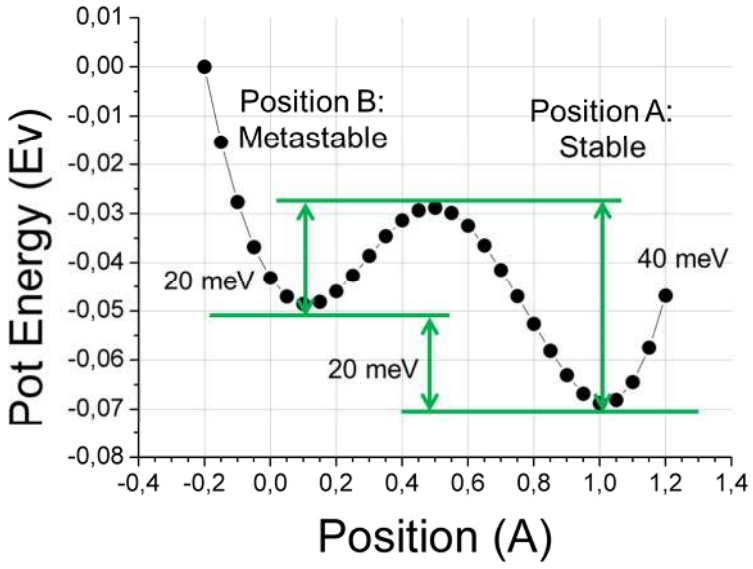

Fig. 4.14) Calculated potential energy landscape of the system versus the position of a rattling atom.

As we have seen in section 1.3), for β relaxation in metallic glasses, the activation energy is 26(±2)RTg [24], [27]; for fast β' and near-constant-loss modes, it is roughly half this value [20]–[22]. Regarding the case of the $Cu_{65}Zr_{35}$ alloy, it is possible to estimate β relaxation activation energy as 1.6 eV by using a value for T_g of 750 K. However, for fast β' and near-constant-loss modes there are no reported value for this alloy, neither a broadly accepted relationship to permit us calculate it. However, since for others reported compositions the activation energy of fast β' was roughly half of the activation energy for β, we could assume a value of the order of 0.8 eV for fast β' processes in the $Cu_{65}Zr_{35}$ alloy, which is still more than an order of magnitude higher than the values we reported for the rattling movements. Recently, Küchemann and Maass [125] claimed to have found another dynamic mode of relaxation in MGs, the so called Gamma (γ) relaxation, which was again studied through DMA analysis, as the other authors who reported values for β and β' modes. The γ relaxation is present at low temperatures and "high" frequencies of 100 Hz (high compared to the typical DMA frequencies). The activation energy of the relaxation mode they found was reported to be of the order of 0.3 eV.

As mentioned in section 1.3), the PEL of MGs is composed by a broad distribution of energy barriers between basins. However, the activation energy values, on which we have commented so far, were all calculated through the Arrhenius equation, which is implicitly averaging over all energy barriers in the PEL. In order to access the complete distribution of activation energies and not only its average, a different method must be used, e.g. to explore directly the underlying PEL of MGs by identifying the saddle points separating neighbouring PEL minima. Obviously, this is only possible by computer simulations. Fan *et al*. [126] applied this method and obtained the distribution of activation energies, as a function of the atomic displacements, for a model $Cu_{56}Zr_{44}$ metallic glass. From their work, it is possible to extract the range of activation energies, which goes from very low values (as low as 0.01 eV) to a few eVs. Interestingly, the lower tail of the activation energies distribution corresponds to very short displacements, between 0.3 Å and 1 Å, similar to the rattling moves present in our system. Furthermore, the activation energy that we found is surprisingly close to the energy difference between a FI cluster and a "fragmented" cluster (i.e. a loosely packed cluster) of 70 meV, reported by Cao *et al*. [127] and similar cluster energy differences (50 meV) have been reported by Wu *et al*. [128] independently of the system's

temperature. These results strongly reinforce the idea that the rattling of atoms is the primary mechanism to destroy a densely packed ICO and leave behind a loosely packed RD, and correlate very well with the fact that the FOM is temperature independent.

The distinctive atomic motions detected in the present work, and depicted in Fig. 4.8, fit the term "rattling" rather better than other modes. The rattling is identifiable as the 'fast processes' in Fig. 1.4, with a high frequency of mechanism (40 GHz) that is essentially independent of temperature. The rattling atoms are congregated in loosely packed zones (Fig. 4.12(a)) that resemble those proposed as the sites of the different relaxation modes in metallic glasses [20]–[22], [34]. String-like motion (Fig. 4.9) that permits the rattling has also been suggested to be the fundamental event underlying β relaxation [129], and has been used to explain the link between β relaxation and the diffusion of small atoms in metallic glasses [26]. Yet, in these studies the string-like motions are clearly thermally activated, unlike the rattling.

The rattling, involving some string-like coordination of the atomic movements, is thus most easily interpreted as a small-amplitude (and possibly shorter-string) precursor to fast β' and later to β relaxation. Such hypothesis is very well supported by the work of Fan *et al*. [126], who focused on the initial triggers of the STZs rather than on the different relaxation modes and presented values of activation energies versus atomic displacements which are in very good agreement with our results.

The spatial distribution of rattling atoms in the glass (Fig. 4.12) resembles to the fraction of atoms participating in the soft modes in $Cu_{64}Zr_{36}$ glass, as found by Ding *et al*. [36]. In each case, the correlation length of the soft spots is ~1 nm. Ding *et al*. [36] show that the sites of shear transformation zones (STZs, the mediators of plastic flow in metallic glasses [130]), are strongly correlated with GUMs and their associated soft spots. The spacing between STZs found by Ding *et al*. [36] is ~2.5 nm, indeed similar to that between clusters of rattling atoms in the present work (Fig. 4.12).

The presence of loosely packed regions in the glass could be attributed to insufficient relaxation. But incomplete relaxation is intrinsic to glasses. Greater degrees of relaxation would reduce the population of loosely packed regions, and reduce the frequency of occurrence of rattling motions, but would not eliminate them.

Finally, we evaluated the time evolution of the Overlap parameter (Q) in the SCS with respect to a fixed reference configuration for several thresholds *d* (see section 3.5). The

results are presented in Fig. 4.15. As foreseeable, the system is not relaxing and once Q arrives to a certain value, depending on the used cutoff, it remains constant.

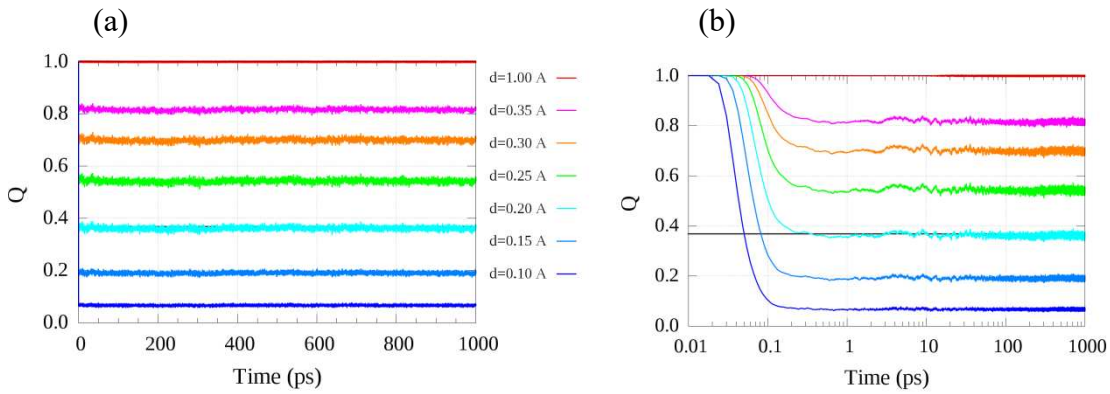

Fig. 4.15) (a) System's Overlap parameter versus time at the quiescent state for different thresholds and (b) same as in (a) with logarithmic scale in the x axis.

However, if we calculate the Overlap parameter by taking into account only the rattling atoms (Fig. 4.16), it is then possible to see a certain degree of relaxation on time, even in the quiescent state and with threshold values significantly larger than the ones used to calculate Q taking into account all atoms in the system (Fig. 4.15)

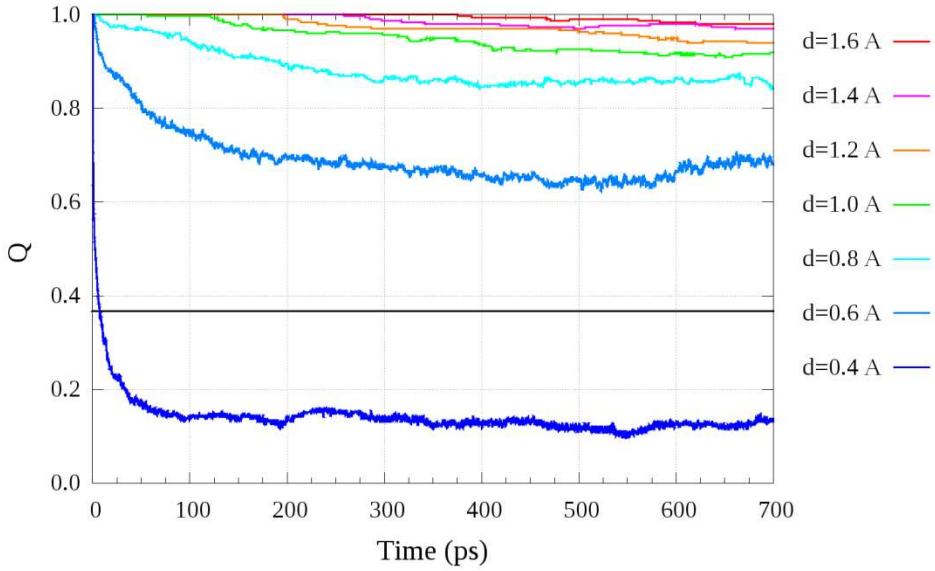

Fig. 4.16) (a) Rattling atoms' Overlap parameter versus time at the quiescent state for different thresholds. Notice the different thresholds with respect to Fig. 4.15.While in average, there is not relaxation in our system in the quiescent state (Fig. 4.15), there is local relaxation around the rattling atoms.

5) Straining process

Metallic Glasses (MG) are well known for their mechanical performances, e.g. high yield stress and elastic strain limit under uniaxial load [6], [7], [127]. The usual drawback concerning the mechanical properties of the MGs refers to the lack of ductility under tensile solicitation, contrary to their significant plasticity under compression or bending [131]–[133]. These particularities are closely related with the structural characteristics of the MGs, and the alterations they suffer under the different types of deformation. The basic structural features of the MGs are the absence of long range order and periodicity, resulting in fundamentally different mechanisms acting under a mechanical solicitation from those referring to conventional engineering alloys, e.g. dislocation or grain boundary movements, etc. We have seen in the previous chapter that MGs consist of tiny clusters of atoms (mostly of Icosahedral-like structure), that may be interconnected and/or interpenetrating, forming Superclusters. Moreover, structural alterations are found to occur also upon annealing of the MGs leading to more loose density and "rejuvenation" of the MGs [112], [134], while relaxation effects have been observed even in as cast samples (in the opposite direction, i.e. ageing [112]), a result that has important consequences in properties like brittleness and toughness fracture. It turns out, therefore, that understanding the structural and dynamical behaviour of the MGs during these relaxation processes is crucial for eventual control and improvement of their properties.

The present chapter aims in a thorough Molecular Dynamics simulations (MD) study of the mechanisms acting upon deformation and the associated atomistic dynamics that are responsible for the structural alterations, including the reshaping of the aforementioned clusters, which results in the deformation accommodation that is accompanied with local density changes [41], [127], [135]. To this end, we performed a deep structural and dynamical analysis, while monitoring the thermodynamics of the response exhibited by the $Cu_{65}Zr_{35}$ metallic glass during the uniaxial tensile straining process.

All graphs included in this chapter representing strain refer to true strain, which is calculated as:

$$True\ strain = \varepsilon_t = ln\frac{L}{L_0} \qquad (5.1)$$

where L_0 represents the initial sample length and L the actual sample length. Similarly, all graphs representing stress in this, and the next chapter, refer to true stress, i.e.:

$$True\ stress = \sigma_t = \frac{P}{A} \qquad (5.2)$$

where P refers to the applied load and A to the cross section where the load P is applied.

5.1) Thermodynamics and simulations details

Using the equilibrated FCS and SCS studied in the previous chapter, we applied uniaxial tensile deformation up to 10% strain, at a strain rate of 10^8 s^{-1} in the Isothermal ensemble while imposing a Poisson ratio of 0.34 in the lateral dimensions [106], [136]. We also performed simulations with different strain rates, 10^7, 10^9 and 10^{10} s^{-1}, for which we used an equilibrated system at 300K.

Fig. 5.1 depicts the stress-strain curve of the FCS and the SCS upon deformation. The inset is a zoom of the curve up to a strain of 2.5%. We fitted the stress-strain curves up to 1% strain in order to obtain the Young modulus of the model glasses and to establish a limit for the linear region (typically associated with the elastic region of materials). The measured Young moduli were 71.6 GPa for the FCS and 75.5 GPa for the SCS, below the reported Young modulus in the literature, obtained experimentally, for the same alloy, under tension (86 GPa and 97 GPa [136]) and compression (88 GPa [137] and 92 GPa [138], [139]). The FCS departs earlier from the linear regime, at around 1.2% strain, compared to the SCS, which exhibit a linear behaviour up to approximately 1.4% strain, indicating a shorter elastic regime for the FCS. However, the major differences on the stress-strain curves of both systems occur from 2% strain up to 8%, i.e. in the plastic deformation region, where it can be clearly seen that the FCS is considerably softer, due to the higher cooling rate used during the glass preparation. In any case, both systems exhibit strain hardening from 6% up to 10% strain. For the rest of the chapter, the results we present refer to the SCS unless otherwise specified.

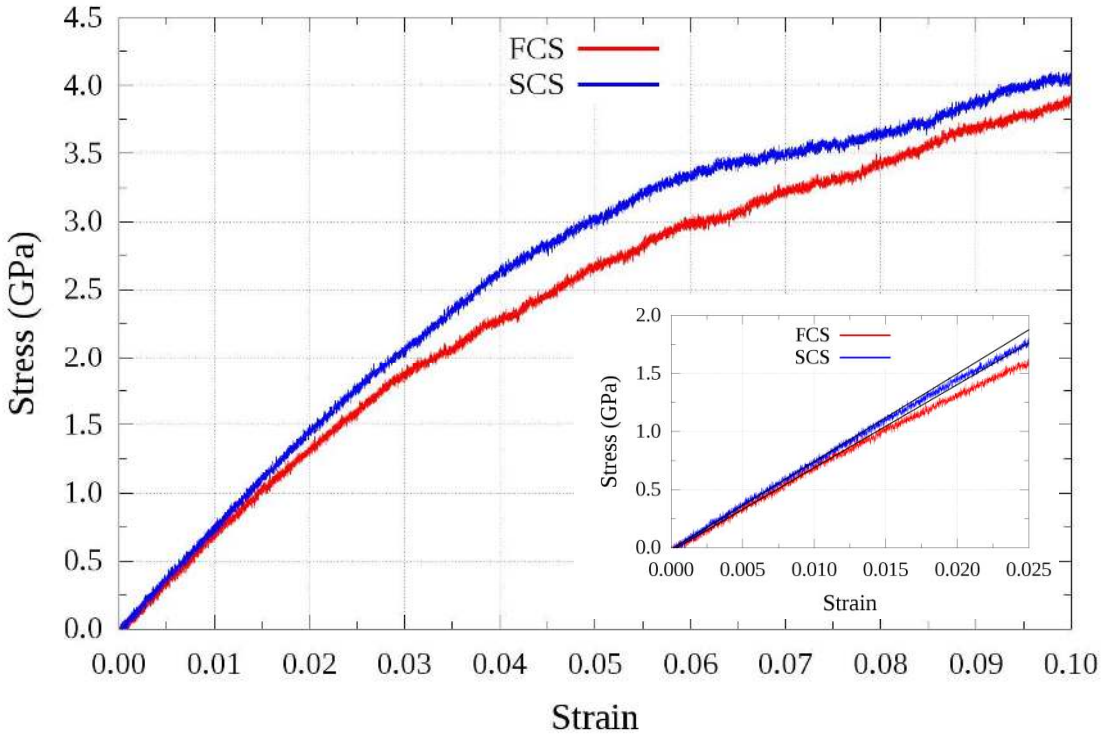

Fig. 5.1) Stress-strain curves for the FCS and the SCS. The inset shows a zoom up to 2.5% strain and straight lines for each system fitted up to 1% strain. The Young modulus is 71.6 GPa for the FCS and 75.5 GPa for the SCS. The Stress-strain curve of the FCS departs slightly earlier from the linear behaviour (At around 1.2% ε_t) than the SCS (at around 1.4% ε_t). During the plastic deformation region (from 2% to 6% strain) the FCS is visibly softer. Both systems present strain hardening after 6% strain.

In our simulations we monitored the kinetic energy (and thereby the temperature) during the application of uniaxial tensile strain. Because of the presence of the thermostat, the kinetic energy (K) of the system was constant and equal to 38.78 meV per atom (Black line in Fig. 5.2), corresponding to a temperature of 300 K. We monitored as well the K_m energy (light blue curve in Fig. 5.2), as explained in section 2.4). Very interestingly, it came out that this mechanical solicitation resulted initially in a small, but consistent, decrease of the K_m of the system, linearly up to 4.5 % strain, reaching a plateau value up to 6% strain, to increase with a constant rate until the end of the straining process. Fig. 5.2 also includes the stress-strain curve of the process (right axis). We can see that this endothermic behaviour of the glass extends beyond the elastic regime and that the slope of the stress-strain curve decreases at 4% and 6% strain, just before and at the end of the K_m plateau. Besides the main bulk systems simulations studied (PBC in the three axes), we performed simulations for a surface (PBC in two axes) and a wire (PBC in one axis). The endothermic behaviour was not present in those simulations, which can be expected

as those systems disposed of mechanism to relax in the axes in which the PBC were not being applied.

Aiming in ensuring that the presence of the thermostat does not affect the resulting system's response, we simulated the straining process with exactly the same conditions and parameters in the microcanonical ensemble, i.e. without the thermostat. The results are included in Fig. 5.2 as well (light green curve). It turned out that the effect is present without significant differences. Indeed, both the total magnitude of the effect and the trends remained unchanged.

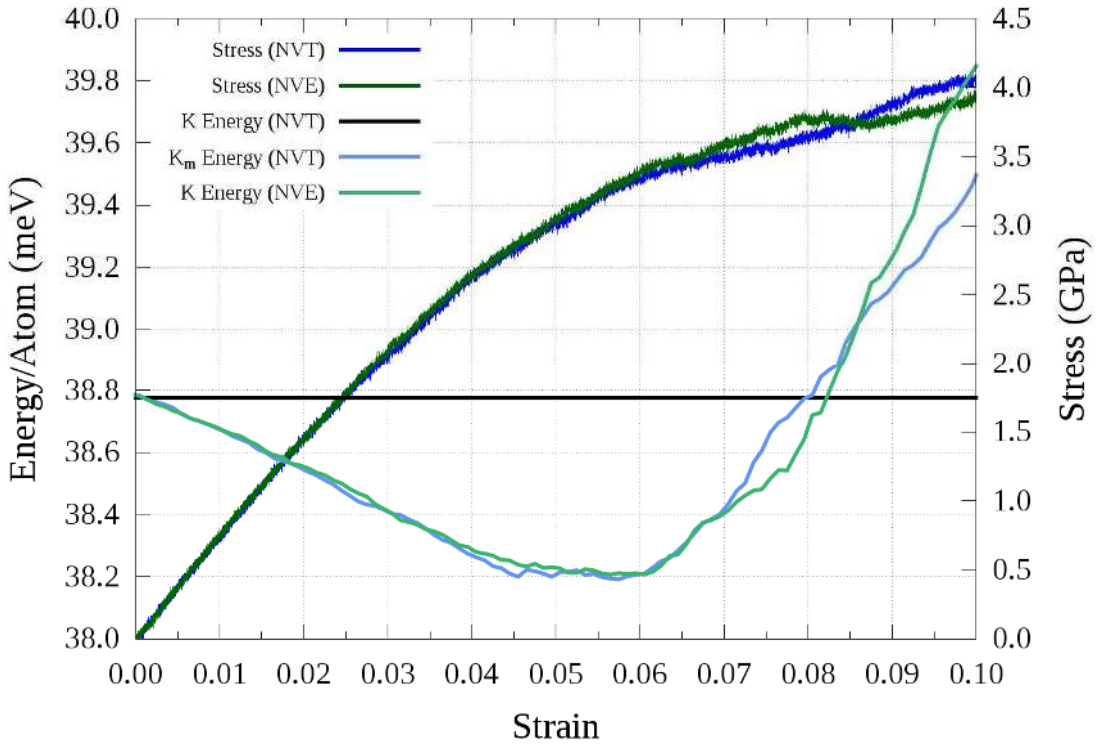

Fig. 5.2) K (kinetic) and K_m (Kinetic without thermostat) energies per atom and stress-strain curves for the SCS with and without thermostat. K is constant when the thermostat is on. K_m decreases linearly up to 4.5 % strain. Then it remains constant up to 6% strain and from there it increases linearly until the end of the straining process. The stress-strain curve shows a linear region up to 1.4% strain. Then the material becomes softer as it enters the plastic region. At 4.5%, 6% and 8% strain the slope of the curve changes significantly.

Given that this endothermic behaviour affects slightly the temperature of the system when we simulated it in the microcanonical ensemble, it is interesting to explore its dependence on the initial temperature of the sample. We performed the same uniaxial tensile process at different initial temperatures below T_g, ranging from 200 K to 600 K.

Fig. 5.3 depicts the variations of K_m, normalized with respect to the initial kinetic energy (K_0). We found that the magnitude of the drop in K_m shows light temperature dependence, being approximately 1% of K_0 for the system a 200 K, 1.5% of K_0 for the systems at 300 K, 400 K and 500 K and 2% of K_0 for the system at 600 K. It is also relevant that the strain at which the plateau starts and ends shifts towards higher strains upon increasing K_0, indicating that the endothermic effect is not unequivocally related with the elastic and plastic regimes, since for higher temperatures the yield strain is lower [135], as it can be seen in the stress-strain curves in Fig. 5.3 (right axis). Moreover, the rate of the K_m increase after the plateau is higher for the systems with lower K_0, as expected, since systems at lower temperature require more energy and develop higher stress upon straining.

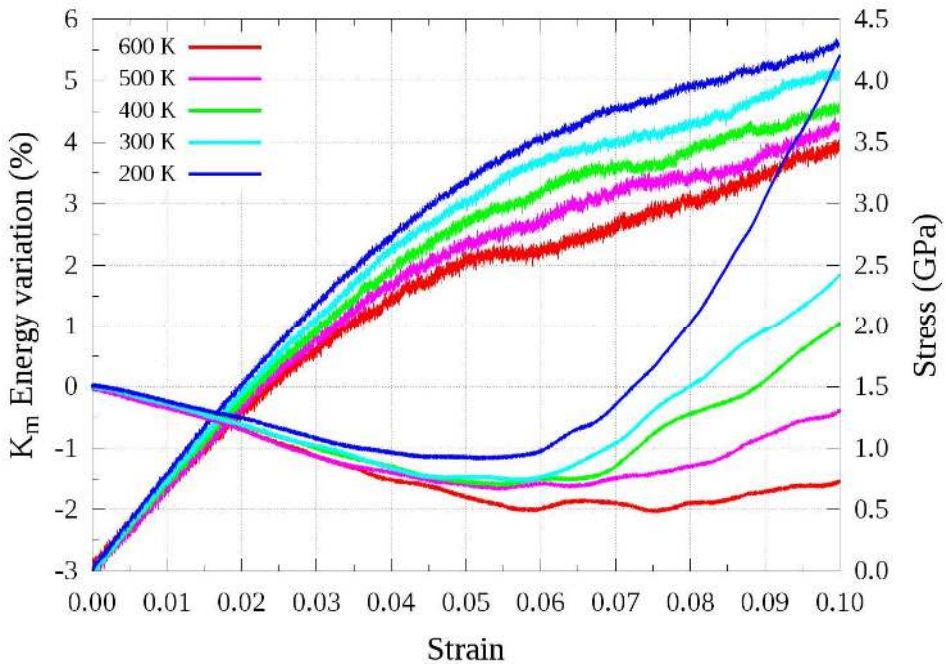

Fig. 5.3) K_m dependence on temperature, ranging from 200 to 600 K, (the variations are in % with respect to the initial kinetic energy (K_0)) and the corresponding stress-strain curves for each temperature (right axis). The drop in K_m is approximately proportional to K_0 and it goes from 1% for the system at 200 K to 2 % for the system at 600 K. The strain at which the drop reverses increases for higher initial temperatures, from approximately 5.5 % strain for the system at 200 K to 7.5% for the system at 600 K. The stress-strain curves reveal the expected dependence on temperature.

Next, we studied the influence of the strain rate on this endothermic behaviour. We used a system equilibrated at 300 K and we imposed the same maximum strain at rates of

10^7, 10^8, 10^9 and 10^{10} s^{-1}. The results are presented in Fig. 5.4 along with the respective stress-strain curves (right axis). It came out that the K_m drop is more pronounced and lasts longer as the strain rate increases. Nevertheless, the rate at which the sample heats up after the plateau is almost the same, i.e. independent of the applied strain rate. The stress-strain curves indicate a higher yield strain for faster strain-rates which is expected as well.

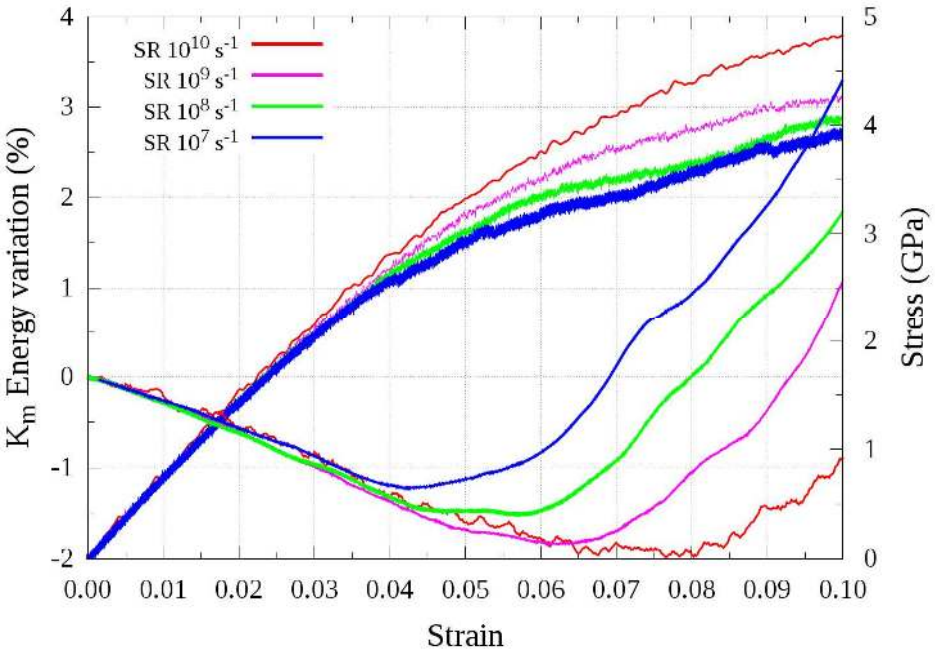

Fig. 5.4) Strain rate (ranging from 10^7 s^{-1} to 10^{10} s^{-1}) dependence of the K_m (drop in percentage with respect to K_0) and the stress-strain curves (right axis). The drop of K_m increases with the strain rate, from approximately 1 % for a strain rate of 10^7 s^{-1} to 2% for a strain rate of 10^{10} s^{-1}. The strain at which the drop reverses also increases for faster strain rates. The stress-strain curves reveal the expected dependence on strain rate.

Finally, we analysed the drop of K_m for target strains of 2%, 4%, 5%, 6%, 8% and 10%. In order to observe the recovery of K_m, especially for the low target strains, once the straining process finished, we kept each system at the corresponding target strain for 1000 ps. The results are presented in Fig. 5.5, where the vertical black lines indicate, for each system, when the target strain was reached. After the vertical black lines, the systems remained strained at the corresponding target strain. The line for the 10% target strain up to 1000 ps is the same as the blue light line in Fig. 5.2 and the behaviour is very similar to the one observed when the target strain is 8%. For a target strain of 6%, K_m recovers exponentially after the target strain is reached, in a very different manner

from the systems with target strains of 8% and 10%. Surprisingly, when we keep decreasing the target strain, the recovery of K_m is markedly distinct. Already at 5%, once the straining process finishes, K_m starts increasing, however, it does it in a rather slower way compared to the system that was strained up to 6%, and the value of K_m does not reach the value of K during the 1000 ps that the system was under fixed strain. At 4% target strain, the recovery of K_m is even slower, and certainly, it does not seem that K_m would reach the value of K, at least in the time scale proper of our MD simulations. A similar scenario seems to hold for the case of a target strain of 2%, where there is almost no recovery of K_m during the 1000 ps that the system remained under a fixed 2% strain.

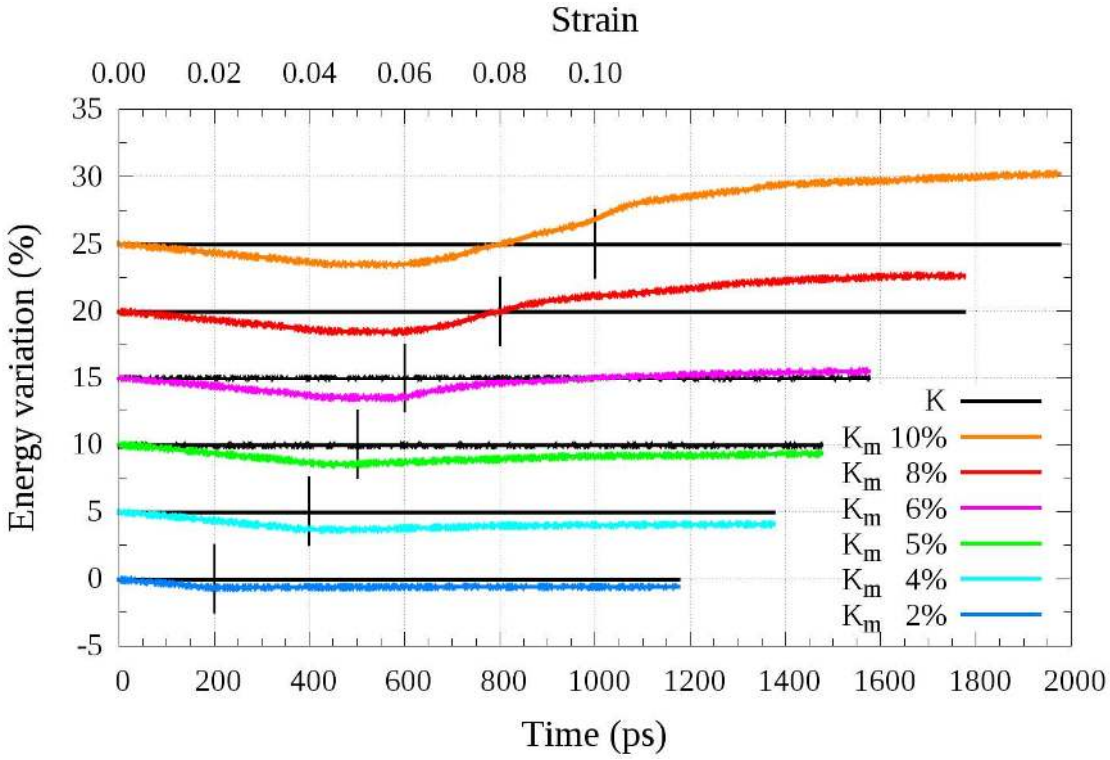

Fig. 5.5) Target strain dependence of the K_m (drop in % with respect to K_0) ranging from 2% to 10%. After the vertical black lines, the systems are restricted at the corresponding strain for 1000 ps. Interestingly, the K_m of the systems is not recovered up to K for target strains lower than 6%, when the endothermic trend is reversed (see Fig. 5.2). Lines for target strains of 4% and higher have been shifted on the y axis to start at 5, 10, 15, 20 and 25 %.

The behaviour of K_m for different target strains is interesting and it is a clear indication of two different processes taking place in the system. On the one hand, there is a process of relaxation, or aging, which seems to be critical up until 6% strain. On the

other hand, there is a process of rejuvenation, which apparently starts being considerable from around 4% strain. Actually, both processes coexist locally at all times in MGs [106], [112]; however, their "magnitude" or influence on the system is not equal at all times. We can see how the aging process is more accentuated during the early stages of the strain, i.e. up to 4%, while the rejuvenation process starts being dominant after 6% strain, well within the plastic deformation region. In between 4% and 6% strain, both processes contributions are approximately equal, which would explain the plateau displayed in Fig. 5.2, Fig. 5.3 and Fig. 5.4. The fast recovery of K_m after the SCS reaches the target strain of 6% but not for lower target strains, is a patent sign that the aging process is vanishing.

The results we present here are in very good agreement with the work on the initialization of STZ upon straining of Cao *et al* [127]. They suggested that upon initial loading, STZs are activated in the sample, even in the elastic region, which they identified to be up to 4% strain. After that, their stress-strain curve deviates from the linear region, which they associated with more and more irreversible shear transformations occurring in their model MGs. At 7.4% strain, their system yielded, coinciding with the spontaneous shear localization into a narrow band. They argued that what they called "fragmented clusters" (similar structures to what we call "loosely packed clusters" in section 5.2)) are intrinsically more ready to undergo local environment changes. However, in the as-quenched glass, these clusters are embedded into the full icosahedra (FI) environment, so they are not free to deform. The "rigid" network of FI needs to be disrupted to allow for the structural rearrangements that carry the strain. In that sense, mechanical work is required to destroy the FI and to prepare the structure for plastic flow. Moreover, they suggested that the localized shear strain generates heat, which becomes very significant when their shear band forms at 7.4%. We suggest that the endothermic behaviour reported in this dissertation is a clear proof of their arguments, where the decrease of K_m at the initial straining stage corresponds with the system destroying the FI network, and the recovery of K_m observed after 6% strain corresponds with the STZ being fully activated and generating heat. In any case, the reason for such a drop and recovery of K_m must be related with the microstructure of the glass, which will be analysed in the next section.

5.2) Structural analysis

Aiming in enlightening and understanding these findings, we analysed the microstructure and its evolution upon straining. First, we compared the RDF and PRDFs of the SCS at the quiescent state (i.e. unstrained system) and once the system reached 10% strain (Fig. 5.6). The differences were rather small and mostly visible only for the Zr-Zr and Zr-Cu PRDFs on the second neighbourhood. It is rather surprising that the interatomic distances show such insignificant differences considering such a substantial applied strain.

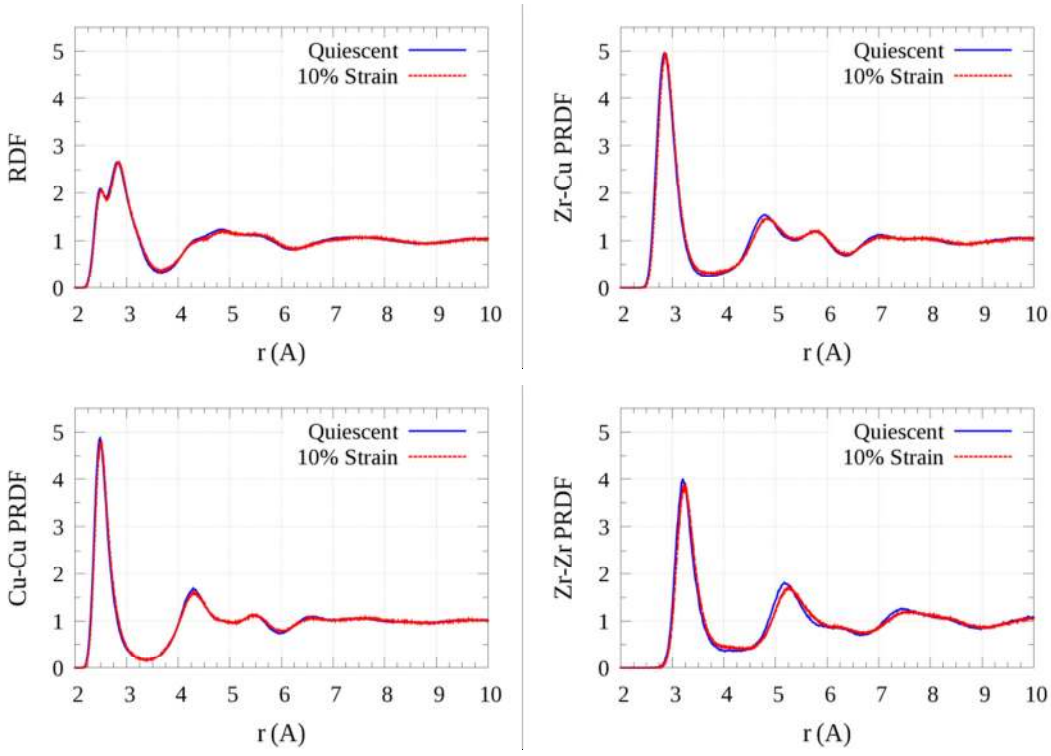

Fig. 5.6) PRDFs for the different pairs of elements and total RDF of the SCS at the quiescent state and under 10% strain. The RDF and PRDFs of the strained system are slighty shifted towards the right. The Zr-Zr and Zr-Cu PRDFs are more influenced by the applied deformation, specially in the second neighbourhood.

Second, we studied the evolution upon straining of the SRO in our system by means of the clusters fitting method. Fig. 5.7 depicts the evolution of the different types of clusters found as a function of the applied strain. It worth's to recall that these atomic clusters, which are characteristics of the MGs' microstructure, are being created and

destroyed, at equal rates when the system state is quiescent. Out of the quiescent state, the difference between the rates of creation and destruction of clusters accounts for the overall proportion of clusters in the system [106], [107]. The plots of Fig. 5.7 demonstrate that the rate of creation of ICO clusters (densely packed) is less than their rate of destruction. This unbalance, induced by the applied load, results in the overall net destruction of ICO clusters, leading the system to a higher energy state and eventually resulting in rejuvenation [106], [112]. This is a rather general scenario, i.e. under mechanical deformation, densely packed ICO clusters are being destroyed and RD clusters (loosely packed) are being created [106], [107], [140]. However, careful inspection of the microstructural response of the system allows for some interesting observations. In the beginning of the straining process, the number of clusters from the quiescent state (0% strain) and up to 2% strain does not change significantly, and in some cases, we can even find the opposite trend to the aforementioned general scenario: RD clusters are destroyed and ICO clusters created, reinforcing the conclusions extracted from Fig. 5.5, i.e. that the system is relaxing in the early strain stages. In the next phase, from 2% to 4% strain, we observe that the rate of creation of loosely packed RD clusters is higher from that of destruction, thus the system starts rejuvenating locally, while it keeps aging also locally, again in accordance with Fig. 5.5. This trend continues in most cases from 4% to 6% strain. Finally, from 6% up to 10% strain, the rate of disordering overwhelms the rate of relaxation and the massive creation of loosely packed RD clusters at the expense of densely packed ICO ones dominates, in agreement, once again, with the ideas extracted from Fig. 5.5.

A similar behaviour for similar stages during the strain process was reported, only for the ICO clusters, by Zhang *et al*. [107] for the same model glass at room temperature. Furthermore, the evolution of the microstructure presented on this dissertation turns out to be in very good agreement with the idea of Cao *et al*. [127] discussed in the previous section, where mechanical work is required to destroy the densely packed ICO clusters and to prepare the system for plastic flow.

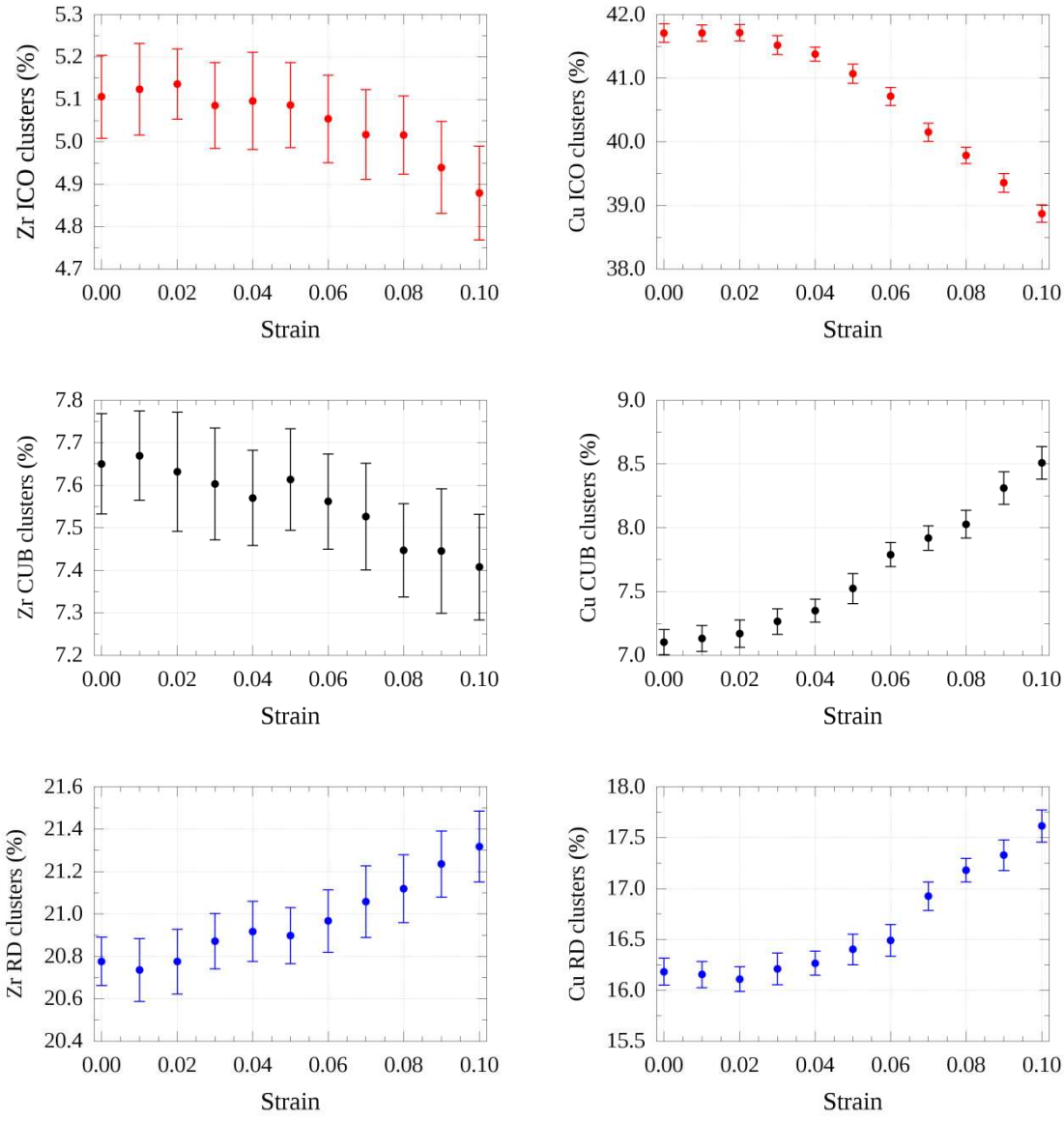

Fig. 5.7) Clusters evolution upon straining. CUB and ICO clusters centred on Zr exhibit small variations up to 6% strain and a considerable decrease after. The number of RD centred on Zr atoms increases from 1% up to 4% strain and then again from 6% up to 10% strain. The number of clusters centred on Cu exhibit little variation up to 2% strain. From 2 to 4% strain, Cu ICO clusters decrease while Cu CUB and RD increase. From 4% up to 10% strain the same trends of creation of loosely packed and destruction of densely packed clusters are present but at higher rates.

The question of whether CUB clusters are loosely or densely packed arises immediately, considering that they are, overall, being created in the case of the Cu centred clusters but destroyed in the case of the Zr centred ones. Taking into account the radius of Zr atoms (1.60 Å) in comparison with the radius of Cu atoms (1.28 Å), it is undeniable that Zr-centred clusters can accommodate more neighbours, and indeed, the CN of Zr atoms it is known to be higher than the CN of Cu atoms [66], [83], [138].

Given that both ICO and CUB clusters allow for a maximum of 12 near neighbours, while RD clusters (preferred by Zr atoms) permit an accommodation of 14 neighbours, it is easy to consider CUB clusters as densely packed when centred on Zr atoms. In the case of Cu centred CUB clusters, the trend shown in Fig. 5.7 is very similar to the one followed by Cu centred RD clusters, suggesting that indeed Cu centred CUB clusters should be considered as loosely packed clusters, at least, when we compare them with Cu centred ICO clusters. Further confirmation for this argument can be derived from Fig. 4.5, which shows that the fit for Cu ICO clusters is better than the one for Cu CUB clusters and that the ICO clusters is preferred in the case of Cu atoms, suggesting that Cu CUB clusters are indeed less energetically favourable, less stable and so, more loosely packed.

A more complete picture of the SRO in our glass can be extracted from the error histograms of the clusters fit method. The state of the SRO is compared for the quiescent system (0% strain) and the strained system in Fig. 5.8. It is possible to observe how the histograms are shifted to the right in all cases, which means that the microstructure of the glass have been distorted due to the straining procedure. If we combine the information provided from Fig. 5.7 and Fig. 5.8, it is clear that not only the number of clusters was decreased in the case of densely packed clusters and increased in the case of loosely packed ones, but the remaining clusters of each type are now more deformed in average. In other words, Fig. 5.7 indicates that the proportion of Cu ICO clusters decreased from 41.7% (with respect to all atoms in the system) to 38.8%, while Fig. 5.8 is suggesting that the remaining 38.8% Cu clusters deviate more from the prototype ICO than the 41.7% at the quiescent state. The same reasoning can be applied to both Cu and Zr and all cluster types, regardless whether their proportion was increased or decreased upon straining. Nevertheless, as depicted in Fig. 5.8, the deformation with respect to the prototypes is more pronounced for Cu atoms, in line with the larger changes in the population of each cluster type for Cu than for Zr atoms, shown in Fig. 5.7. Furthermore, the shoulder on the left part of the Cu ICO clusters is significantly less pronounced when the system is under 10% strain, which indicates that a large number of the Cu FI clusters have been destroyed, suggesting that the deformation of the glass severely affected this particular atomic arrangement.

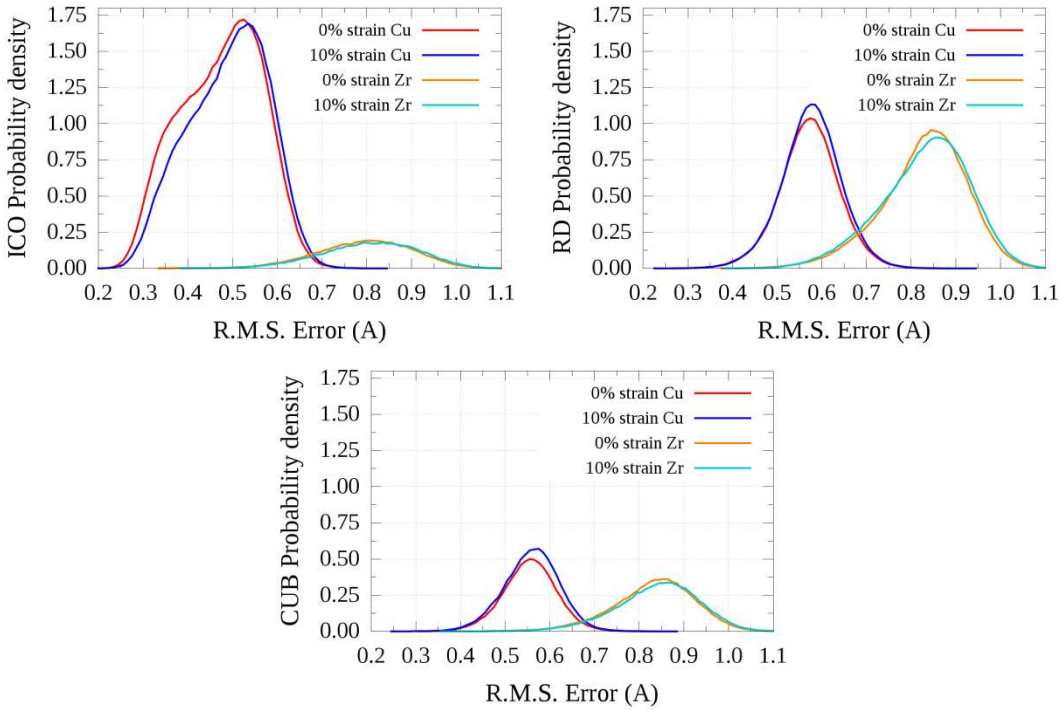

Fig. 5.8) Comparison of the clusters error histograms before and after the straining process. The areas under each of the lines represent the probability. Changes in the microstructure are more accentuated for Cu atoms, as already shown in Fig. 5.7. In all cases, a shift towards the right is also visible, indicating that the microstructure has been deformed upon straining. Note the decrease in the Cu FI clusters (the left shoulder of the Cu ICO error histogram)

Moreover, we investigated the evolution of the MRO through the number of Superclusters present in our glass (Fig. 5.9). At the quiescent state, the number of Superclusters in our system (containing 31250 atoms) was 3490. Upon straining, this number was consistently reduced at different rates during each of the strain intervals established previously in this chapter. Namely there is small decrease during the early stages of the straining process, followed by a plateau in between 3% and 4% strain. Interestingly, the higher destruction rate occurs between 4% and 6% strain, coinciding with the plateau of K_m in Fig. 5.2. From 6% to 10% strain, Superclusters keep being destroyed at a slightly slower rate. Curiously, the higher rate of destruction for the Superclusters take place before the higher rate of destruction of the densely packed clusters (Fig. 5.7), which suggest that the Superclusters are being affected ahead of the clusters by the transition between aging dominance and rejuvenation dominance phases taking place in our glass. Zhang *et al*. [107] studied the MRO of the same model glass upon loading in terms of the Bergman-type clusters [141]. They found a very similar

behaviour at very similar strain stages to the one presented here through the analysis of the MRO in terms of the Superclusters.

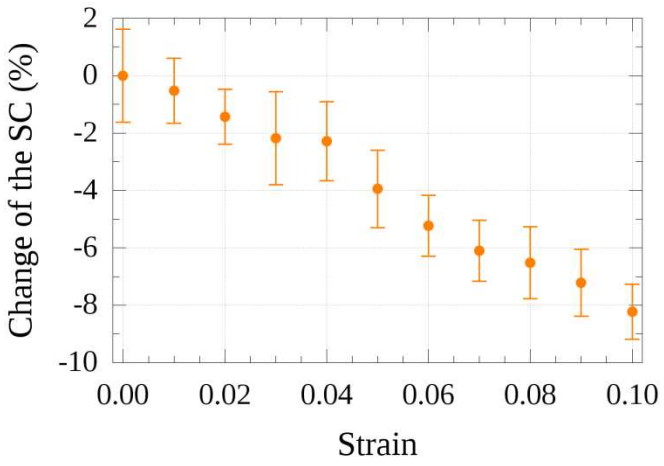

Fig. 5.9) Evolution of the total number of Superclusters (SCs) upon strain. The Superclusters are being consistently destroyed, as the densely packed clusters. 2% of the Superclusters present at the quiescent state are eliminated once the system reaches 4% strain. The destruction rate of Superclusters changes dramatically after 4% strain and slightly after 6% strain, indicating a strong correlation between the endothermic process and the MRO.

Fig. 5.10 depicts the volume increase upon deformation. We measured a total increase of 3.4% with respect to the initial volume. Obviously, such an increase is entirely determined by the applied Poisson ratio. More interesting is the proportion of that volume directly associated with cluster transformations from ICO to RD and CUB, which turned out to be a 30% for the FCS.

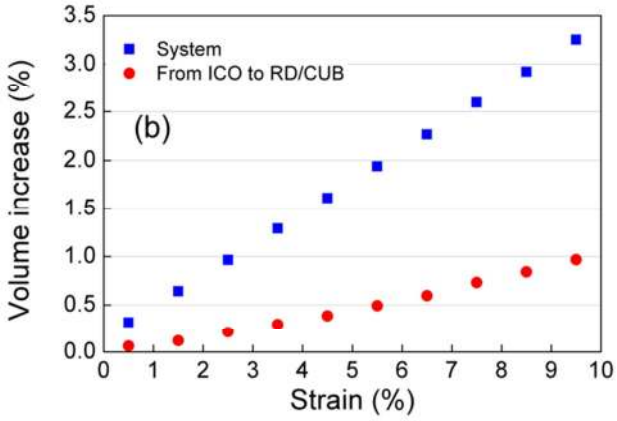

Fig. 5.10) Volume evolution of the FCS upon straining: at an imposed tensile strain of 10%, the volume increase directly associated with the transformation of ICO clusters to RD and CUB types accounts for nearly one third (30%) of the total volume increase of the glassy system. Calculated errors are smaller than the points' size.

Because the microstructure of the system is evolving towards a higher number of loosely packed clusters, it is foreseeable to find an increase in the number of first neighbours for each atom, i.e. the atomic coordination number, which can be accessed by measuring the number of Voronoi faces per atom [18], [83], [84] (Fig. 5.11). As expected, the average number of Voronoi faces for both Cu and Zr atoms increases upon straining, although the increase is certainly not very significant. Cu atoms start with an average CN of 12.23 which increases up to 12.27. In the case of Zr atoms the increase is slightly more accentuated: from a starting CN of 16.60 to a CN of 16.73 at the end of the straining process. Despite of the total increase being almost negligible, especially for Cu atoms, the rates at which this increase occurs (the slopes in Fig. 5.11) at the different straining stages can provide some insight of the material response to such stages. In the Zr case, the critical points at which those rates become faster precede the critical points that characterize the endothermic behaviour in Fig. 5.2, i.e. 3.7% and 5.75% strain. For Cu atoms, the rate at which the CN increases occurs even before, at approximately 3.5% strain. Then, there is a small decrease taking place between 6% and 7% strain, when the rejuvenation process in our system become more dominant. The change of the CN depicted here is correlated with the decrease of the densely packed clusters and the increase of the loosely packed ones on which we have commented previously. Moreover, this increase in the CN is associated with the development of the STZs [127].

In the previous chapter, it was demonstrated that the atomic volume distributions, obtained by means of Voronoi analysis for Cu and Zr, were Gaussian-like shaped and slightly skewed to the right, indicating an excess of atoms with a bigger volume than normal. Here, we analyse the evolution of such anomaly upon straining, by evaluating the area of the Gaussian distribution of atomic volume left under and over two standard deviations from the average (2STDL and 2STDR respectively), and comparing it with the same area in the case of a perfect Gaussian, i.e. 2.1% on the left of the average minus two standard deviations and 2.1% on the right of the average plus two standard deviations. The results are presented classifying the atoms by element (for Cu and Zr separately) in Fig. 5.12. As we saw in the previous chapter, already before any strain is applied, the proportion of Cu atoms with an anomalous large volume (2STDR in Fig. 5.12(b)) is more than 2.95 %, and slightly less than 2.85% for Zr atoms. In addition, the proportion of Cu atoms with an anomalous small volume is approximately 1.7% for Cu

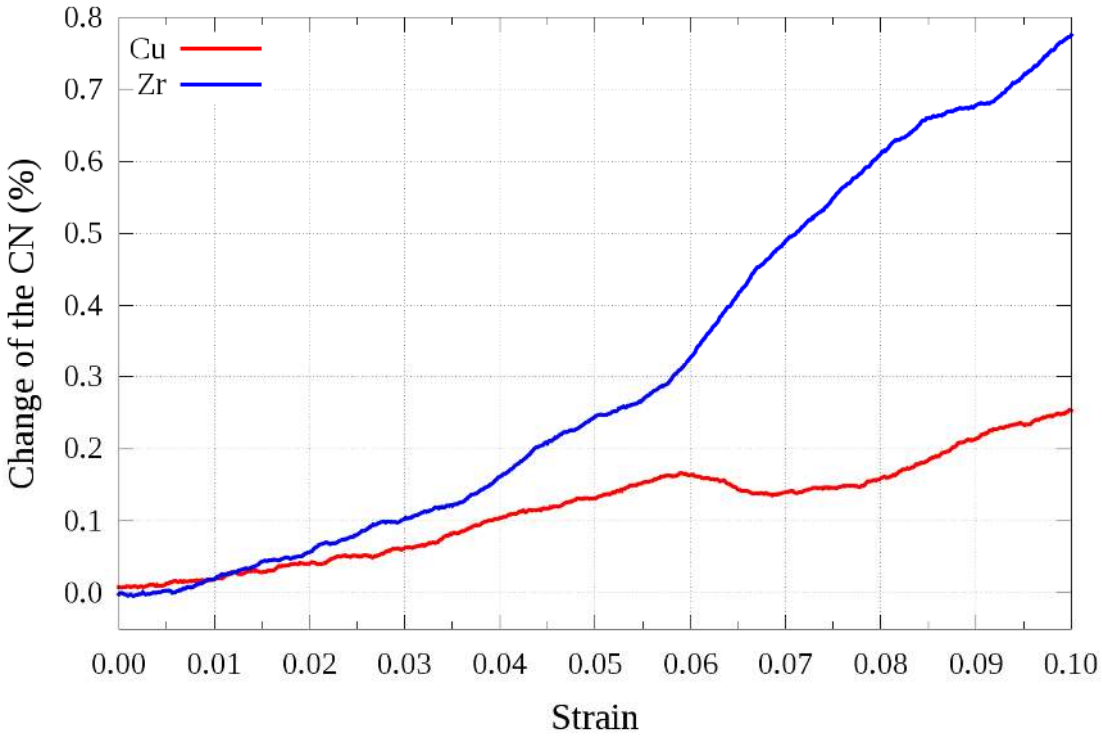

Fig. 5.11) Variation of the number of Voronoi faces (i.e. CN) upon straining. Cu, in red, starts with an average of 12.23 neighbours. The CN increases up to 6% strain. The slope of the curve changes slightly at 3.5% strain, just before the endothermic behaviour reaches a plateau. At 6% strain there is a small decrease that last up to ~ 7% strain. Then it rises again until a total increase of 0.25% when the strain is 10%. Zr, in blue, starts with an average of 16.60 Voronoi faces and it increases during the whole strain process, Notice that the rate at which it increases is higher from 3.7% strain and even higher when the system reaches 5.76% strain, coinciding with the end of the K_m plateau.

atoms and 1.65% for Zr atoms (2STDL in Fig. 5.12(a)). The evolution of these areas seems to be different for Cu and Zr and for the 2STDL and 2STDR as well. On the one hand, for Zr atoms, the behaviour of both the 2STDL and the 2STDR areas seems to be rather oscillatory and slightly correlated. On the other hand, this is not the case for Cu atoms, which exhibit a rather steady decrease of the 2STDL area and increase of the 2STDR area. Interestingly, both the 2STDL and 2STDR Cu atoms areas change at a faster rate when the system reaches 4% strain, coinciding with the point at which the aging is not dominant anymore. It is remarkable that in all cases there are not significant changes during the first straining stage but as the strain increases, the deviations become more pronounced, showing a rise in the number of atoms with larger than expected volume and a decrease for the ones with smaller than expected volume. The anomaly in the atomic volume distributions presented here and its evolution upon strain is a clear

indicator of the structural anisotropy, which have been reported even within the elastic regime [136] and it is considered to be associated with the formation of STZs [117].

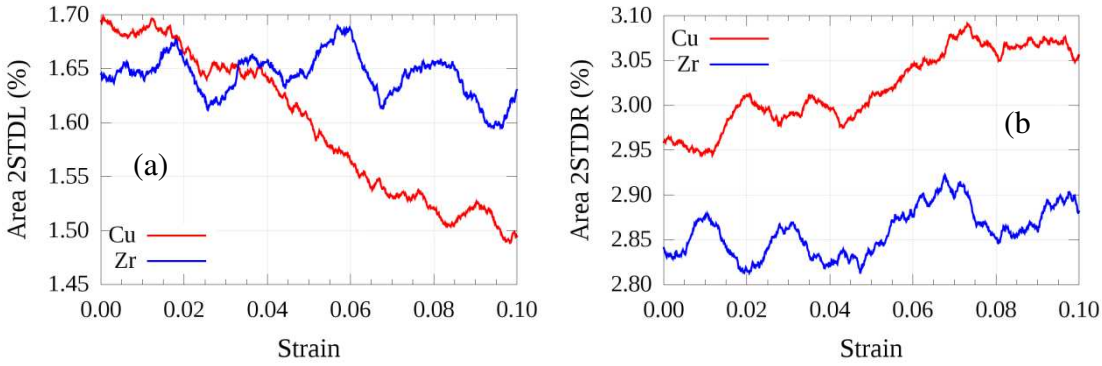

Fig. 5.12) Evolution upon strain of the area of the Voronoi Volume Gaussians under (a) and over (b) 2 standard deviations (2STDL and 2STDR respectively) for Cu and Zr. The system shows for both, Zr and Cu, an excess of atoms with a very large volume and a lack of atoms with a very small volume, indicating that the distribution of their atomic volume are right-skewed Gaussians that are further skewed to the right as the straining process progresses.

5.3) Dynamics analysis

We continue now with the analysis of the dynamics of the SCS upon tensile strain. As described in section 3.4), the SD is a very interesting tool to quantify the dynamics of a system for a simulation in which several stages can be identified, because, rather than performing an average between the different stages, we compare the atomic displacements with respect to the initial configuration, thus the different dynamic phases emerge from this analysis. Furthermore, the procedure to simulate the straining process of a system involves the modification of the atomic coordinates. In our case, a small quantity is added to the coordinate corresponding to the axis in which the system in being stretched out and that small quantity multiplied by the Poisson ratio (0.34 for our system) is removed from the two others atoms coordinates. Those coordinates modification are usually referred to as affine displacements. For the study of the dynamics in this section, we have removed the affine displacements from the coordinates of the atoms in the system. Moreover, since the straining process occurs at a constant rate, there is a linear correspondence between strain and time, where an

increase of 1% strain corresponds to 100 ps. In addition, the classification of the rattling atoms in this chapter have been done including all atoms that jumped at least once, at any time, during the straining process, and following the same rules as in the previous chapter (i.e. jumps of at least 0.6 Å and residence times of at least 1.5 ps in the new position). This, yielded a number of rattling atoms of 2506, from which 1943 were Cu atoms and 563 were Zr atoms, which means that 8% of the atoms in the systems were rattling, from which 6.2% were Cu atoms and 1.8% were Zr atoms. By comparing these proportions with the ones obtained at the quiescent state (0.9% for Cu atoms and 0.1% for Zr atoms), it is clear that the rattling mechanism is significantly enhanced by the applied strain. Zhang *et al*. [107] reported as well a significant increase regarding their mobile atoms in deformed models with respect to the undeformed one. On the other hand, the fractions of their mobile atoms are not directly comparable with ours because they performed their measurements at a different temperature (600 K), with a different definition of the mobile atoms (e.g. a MSD cutoff of 4 Å) and with different simulation conditions (a cooling rate of 10^{10} K/s, a strain rate of 10^{7} s^{-1}, etc.)

The SD of the SCS is represented in Fig. 5.13, separately for Cu and Zr and for the rattling atoms. As we saw in the previous chapter, the lighter and smaller Cu atoms have a larger SD than the Zr atoms, however, they follow the same trends, i.e. they remain caged up to 4% strain, where the slope of the SD increases indicating faster dynamics. Interestingly, the SD slope increases again at around 6% strain, matching the two critical points that characterize the endothermic behaviour exposed in section 5.1). On the contrary, rattling atoms start having faster dynamics after 250 ps (i.e. with the system being under 2.5% strain) although once again the SD slope increases at approximately 4.2% and 6.2% strain. The change in the slope, however, is considerably more significant than the one referring to all atoms in the system. At 7.5% strain there is a slight decrease of the SD slope, for both, the system and the rattling atoms. In average, the atoms break the cage just after 100 ps, as indicated by the upturn in the inset of Fig. 5.13, where the x axis is represented in logarithmic scale. The rattling atoms, on the other hand, break the cage after 50 ps, which support the idea of the rattling atoms being centres of defective (or loosely packed) clusters in liquid-like regions from which it is easier to escape. Similar changes in the slope of the atomic displacements as the ones reported here for the rattling atoms were found by Cao *et al*. [127] for groups of atoms inside a Shear band.

The Overlap parameter (Q) of the SCS calculated upon straining (Fig. 5.14) is markedly different from the picture at the quiescent state (Fig. 4.15). A decline is observable for all values of the threshold *d* and relaxation times can be obtained from the time at which Q reaches the value 1/e (see section 3.5)). For values of *d* below the average thermal vibrational amplitude (i.e. from 0.1 Å to 0.2 Å), the relaxation times (Table 5.1) are less than 1 ps. For values of *d* around the average thermal vibrational amplitude (i.e. 0.25 Å to 0.35 Å) we obtain relaxation times of the order of a few hundred ps. When the value of *d* is very large (1.0 Å) there is not full relaxation at our time scales.

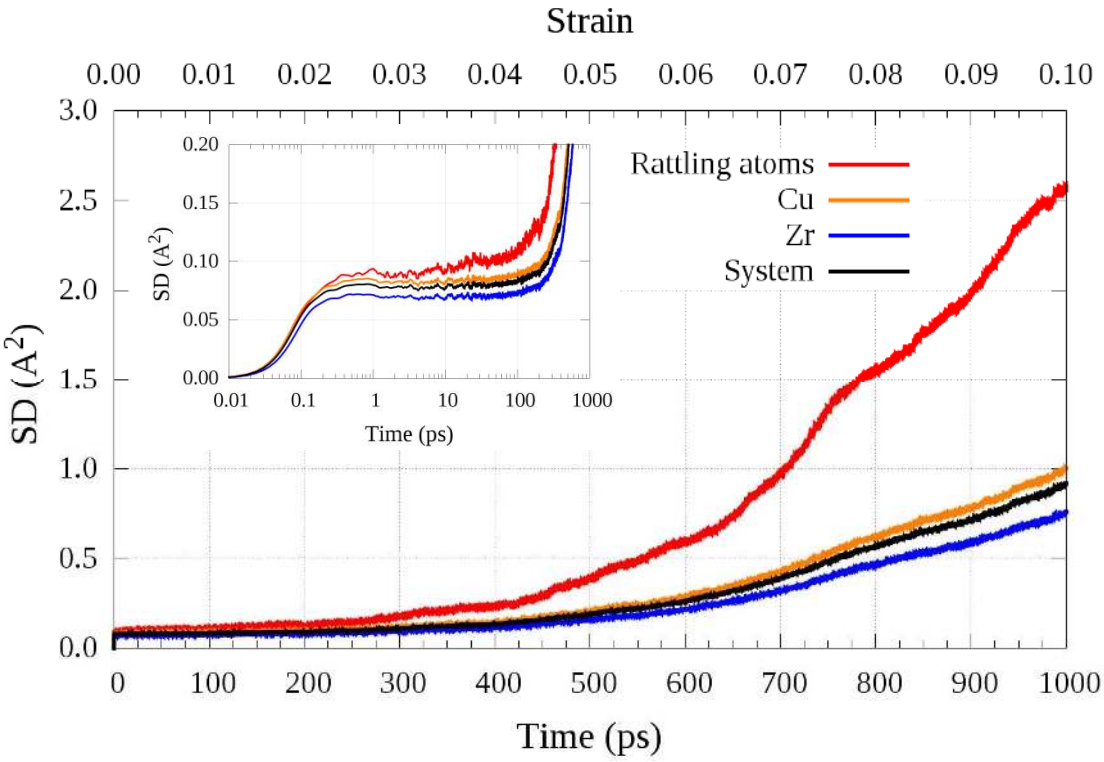

Fig. 5.13) SD for all atoms in the system, separately for Cu and Zr and for the rattling atoms upon straining. In the inset the x axis is in logarithmic scale. Affine displacements have been removed from the atomic trajectories. Rattling atoms break the cage at around 50 ps, as indicated by the upturn in their SD in the inset. They start diffusing at 250 ps and their dynamics become faster at 420 and 620 ps, corresponding with the system being under 4.2% and 6.2% strain. The slope of the SD decreases slightly at 750 ps, indicating a slowdown of the dynamics. The rest of the atoms in the system start breaking the cage after the rattling atoms, at around 100 ps and similar trends can be observe regarding their SD with that of the rattling atoms, although considerably less pronounced and in a lower magnitude.

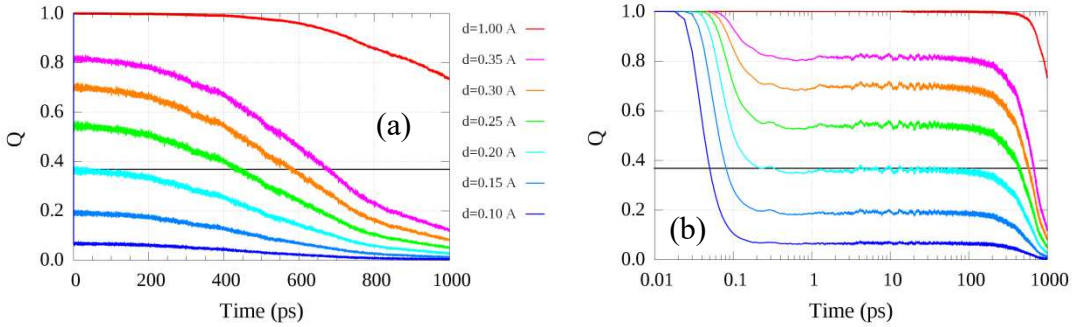

Fig. 5.14) (a) System's Overlap parameter versus time during the straining process for different thresholds and (b) same as in (a) with logarithmic scale in the x axis. For very short distances below 0.2 Å, the relaxation times are below 1 ps and correspond to the atomic thermal vibration. For values of d of the order of the average amplitude, 0.3 Å, the relaxation times are of the order of a few hundred ps. All the relaxation times obtained are summarized in Table 5.1.

The picture is rather different when we calculate Q only for the rattling atoms (Fig. 5.15), specially taking into account the different values of *d* that we used. Again for a cutoff of 0.2 Å we find a relaxation time lower than 1 ps. As the cutoff is increased, the relaxation times become of the order of hundreds of ps.

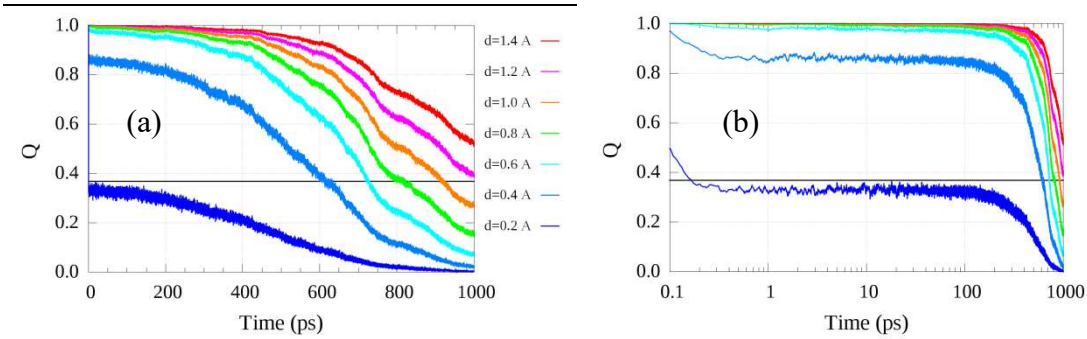

Fig. 5.15) (a) Overlap parameter versus time for the rattling atoms for different thresholds (longer than in the previous figure for the whole system) and (b) same as in (a) with logarithmic scale in the x axis. All the relaxation times obtained are summarized in Table 5.1.

Next, we calculated the MSD for the rattling atoms (Fig. 5.16) and we also classified them according to whether they jump more or less than 1 Å. The outcome is that, contrary to what we saw in the previous chapter, all rattling atoms are diffusing, regardless of the distance of their jumps. We found that they diffuse in average, for all time delays *dt*, with a diffusion coefficient of $3.6 \cdot 10^{-8}$ cm^2/s, which is slightly higher than the one reported at the quiescent state ($2 \cdot 10^{-8}$ cm^2/s). It is relevant to recall that the MSD averages in time for the whole trajectory, and in that sense, we cannot say from the results depicted in Fig. 5.16 when do they start diffusing, in the same fashion as we

did with their SD (Fig. 5.13). Nevertheless, we can observe that they break the cage in less than 5 ps, but once again, this time is an average that includes both, the elastic and the plastic regimes.

Fig. 5.17 represents the Overlap parameter (Q) for rattling atoms as a function of the configurations delay, *dt*, which yields lower relaxation times than those from Fig. 5.15. This behaviour is expected, since for the calculations of Q for a delay e.g. of 1 ps, all pairs of configurations separated by 1 ps were averaged, which includes the ones with slow dynamics at the beginning and the ones with fast dynamics at the end of the straining process (similarly to the stated differences between the SD and the MSD).

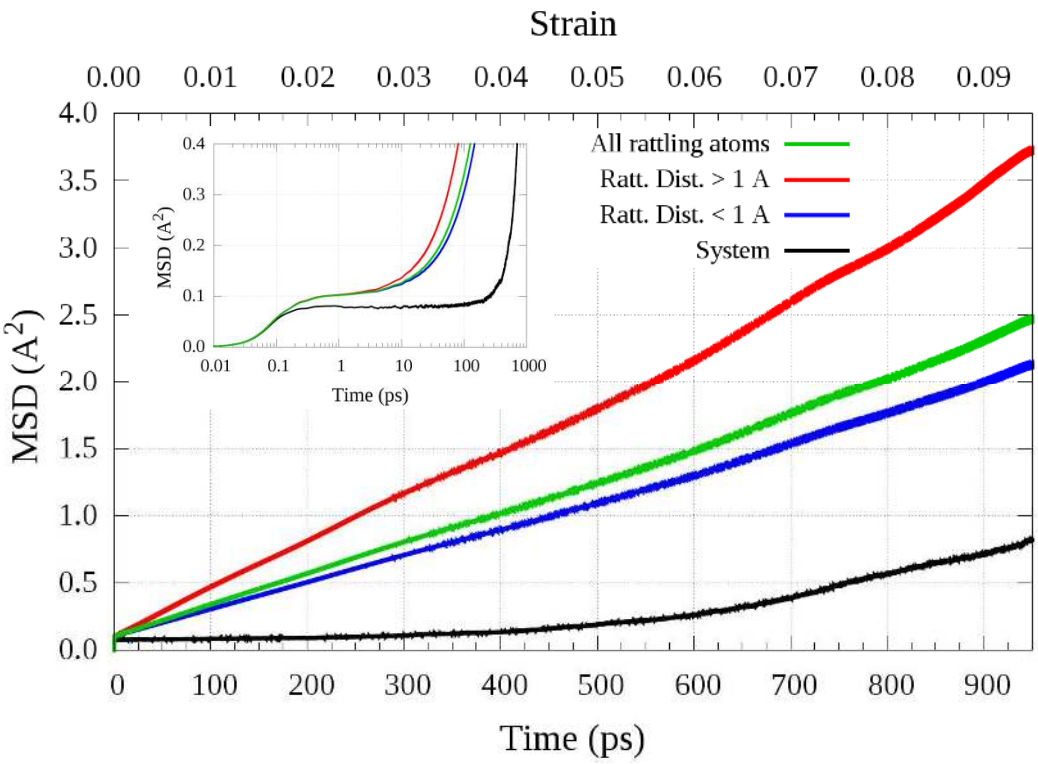

Fig. 5.16) MSD for all the rattling atoms and separately for atoms that jumps more or less than 1 Å. The system SD (black line) is also plotted for reference. In the inset, the x axis is plotted using a logarithmic scale. Rattling atoms diffuse with a diffusion coefficient of 3.6 ·10^{-8} cm^2/s. Most of the rattling atoms perform jumps of less than 1 Å. The inset shows that rattling atoms breaks the cage in less than 5 ps (in average along the entire trajectory, i.e. including all the stages of the straining process). Atoms jumping more than 1 Å break the cage even sooner, at around 2.5 ps.

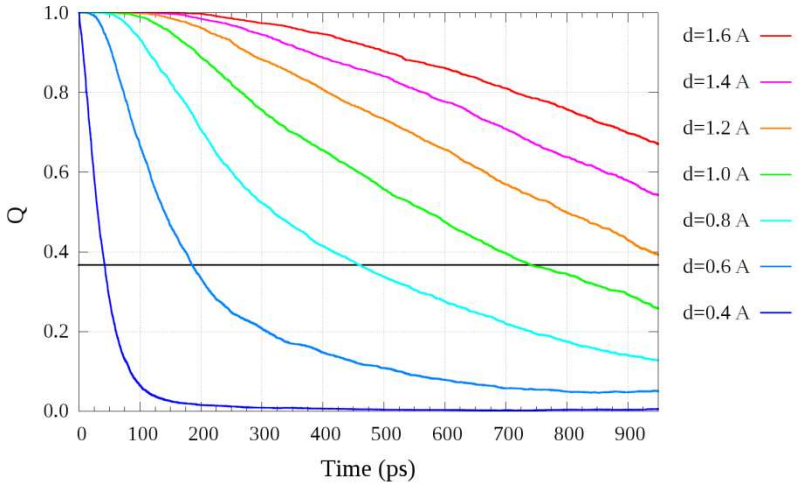

Fig. 5.17) (a) Overlap parameter versus time for the rattling atoms using their MSD (i.e. averages over the entire strain process) for different thresholds. All the relaxation times obtained are summarized in Table 5.1.

The different relaxation times obtained through the overlap parameter using the system and the rattling atoms SDs and the rattling atoms MSD (see section 3.5) are summarized in Table 5.1. Very short relaxation times of less than 1 ps correspond to distances below the atomic vibrational amplitude. Rattling atoms have relaxations times of a few hundred of ps for larger distances, from 0.4 Å to more than 1 Å. The fact that the relaxation times of rattling atoms obtained by means of the MSD are shorter than those corresponding to the ones obtained by means of the SD (for the same distance cutoff) strengthens the idea that the dynamics of the system become markedly faster as the applied strain increases.

The acceleration of the system dynamics correlates very well with the increase of the frequency of occurrence (FOC) of the rattling moves. Fig. 5.18 represents the histogram of the atomic jumps upon straining. It must be clarified that, because the affine displacements have been removed, the magnitude of the FOC depicted in Fig. 5.18 is significantly underestimated, especially for larger strain values. Nevertheless, it is still possible to extract some conclusions by just looking at the trend. It is rather clear that the FOC increases upon straining, particularly after 6% strain, coinciding with the end of the plateau of K_m. It is also noticeable that at the very beginning, the value of the FOC is even lower than at the quiescent state, reinforcing the idea of a slowdown of the dynamics due to the relaxation process associated with the endothermic behaviour. The quiescent value of the FOC is recovered at around 4.5% strain, when K_m reaches the plateau.

System		SD Rattling atoms		MSD Rattling atoms	
Cutoff *d* (Å)	**Rel. time τ (ps)**	**Cutoff *d* (Å)**	**Rel. time τ (ps)**	**Cutoff *d* (Å)**	**Rel. time τ (ps)**
0.10	0.05	0.2	0.1	0.4	42
0.15	0.08	0.4	618	0.6	184
0.2	0.23	0.6	725	0.8	458
0.25	438	0.8	815	1.0	738
0.3	582	1.0	918	1.2	1020
0.35	675	1.2	1020	1.4	--
1.0	--	1.4	--	1.6	--

Table 5.1) Relaxation times obtained from the overlap parameter decay upon straining

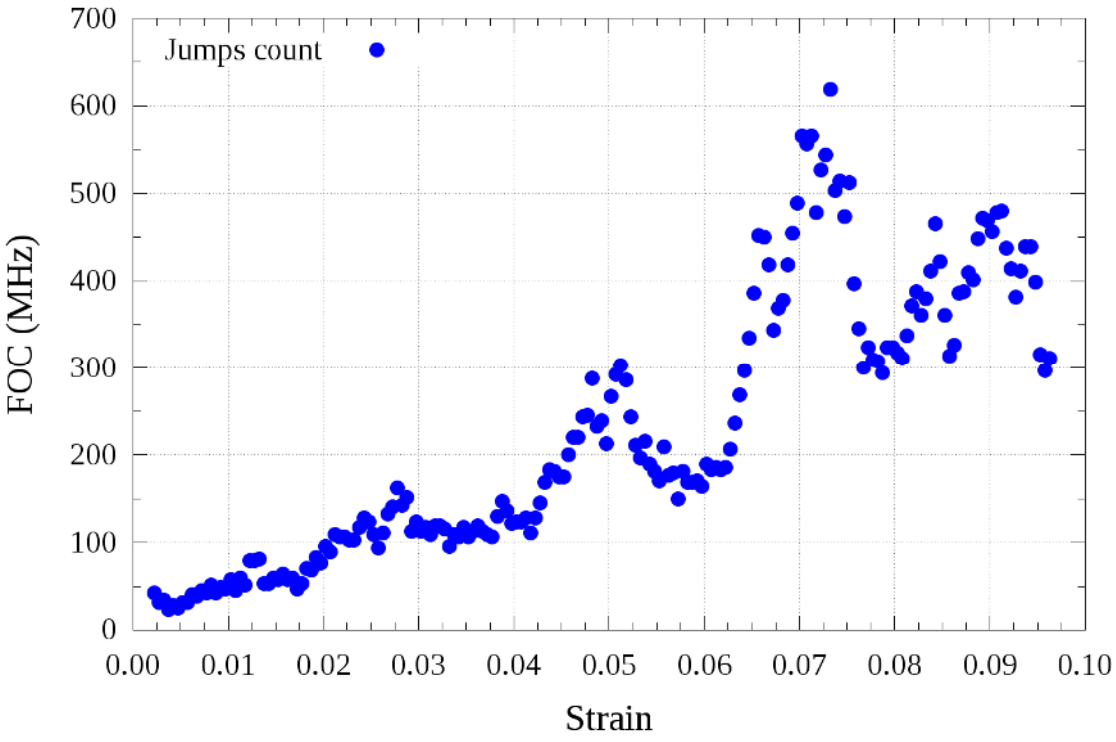

Fig. 5.18) Histogram of the Rattling movements vs strain. The FOC on the atomic rattling increases with strain. This histogram is calculated based on a trajectory for which the affine displacements of the atoms were removed, thus causing considerable inaccuracies and generally an underestimation regarding the number of jumps. These inaccuracies and the underestimation become more pronounced at higher strains, however, general trends can still be extracted. Interestingly, at the beginning, the FOC is lower than at equilibrium, which could be connected with the endothermic behaviour. The equilibrium FOC is recovered at around 4.5%, when the drop in K_m reaches the plateau.

Aiming into further enlighten the relationship between the rattling atoms and the STZs we calculated the D^2_{min} parameter defined by Falk and Langer [42] as described in section 3.4). We used the unstrained system configuration as reference and calculated the D^2_{min} upon straining. The results are depicted in Fig. 5.19. Column (a) includes all atoms in the system, column (b) includes only the rattling atoms and column (c) includes those atoms in the system with an extreme large value of D^2_{min} (i.e. more than 35 Å^2). Each of the five rows corresponds to strain intervals of 2%, from the interval [0%, 2%] represented in row 1 to the interval [8%, 10%] represented in row 5. Each atom is then coloured depending on their D^2_{min} value, which was averaged over 200 configurations from the corresponding strain interval. For example, the plot (a3) represents the D^2_{min} value of each atom in the system, averaged over 200 configurations from 4% to 6% strain. In the plot (b3) only the atoms that jumped during the strain interval [4%, 6%] are represented, again coloured by their averaged D^2_{min} value. Finally, the plot (c3) includes only the atoms for which their averaged D^2_{min} value was larger than 35 Å^2. In all cases, the vertical axis corresponds to the direction of the applied strain field (i.e. the z axis) and the colour bar goes from 0 Å^2 (blue) to 25 Å^2 (red). Notice that the box size does not increase in the z axis because the homogenous box deformation is removed when the non-affine displacements are extracted from the atoms coordinates. The length of the box in each axis is 79.7 Å. Furthermore, the simulation box has not been sliced while producing these images, which means that the plots are projections on the plane xz. Finally, it worth recalling that PBC are applied in all directions, the system do not have surfaces, thus, although the column (a) represents one of the sides of the box, it should be regarded as an internal slice of the system.

During the first strain interval (row 1, from 0% to 2% strain), the D^2_{min} value is very small and only a few atoms are rattling, mostly concentrated in small regions. The situation is quite similar during the second strain interval, although some regions (bottom and top left in the plot (a2)) start showing a rise of the D^2_{min}. In this region, our system is rejuvenating, as suggested previously in this chapter when we analysed the thermodynamics and the atomic structure. From 4% to 6% strain (row 3), there is a sudden increase in the number in the number of rattling atoms, which is accompanied by the growth of the regions that showed a rise of the D^2_{min} in the previous strain interval and the appearance of new regions with high D^2_{min} in the centre of the plot (a3).

However, the high mobility liquid-like zones of the system are still concentrated on isolated regions, indicating that the system is locally aging and rejuvenating, which coincides with the K_m plateau. As we keep straining the system in the next interval from 6% to 8% strain (row 4), we start observing the percolation of the aforementioned liquid-like regions, indicating that STZs are actively forming in the system, which is now predominantly rejuvenating, in accordance with the K_m behaviour. In fact, the upturn of the K_m that takes place at 6% strain, indicates that the system temperature would increase (locally) if it was not coupled with a thermostat, as demonstrated when the strain process is simulated in the microcanonical ensemble (light green line in Fig. 5.2, [127]). Interestingly, the regions of atoms with the larger D^2_{min} value (c4) seem to grow with a preferred orientation, of approximately 45º, with respect to the direction on which the tensile strain is applied. This is a well-known characteristic of the formation of shear bands [94], [127], [132], [142]. In the last stage, from 8% to 10% strain, almost all liquid-like regions percolate as if the system itself was inside a shear band. Also the preferred percolation orientation aforementioned is now clearer. Notice that a well-defined shear band cannot be form in our system because the size of our simulation box is not large enough. Moreover, there are no surfaces in our system to facilitate their initiation [127], [142]. Finally, it should be noted that the rattling atoms could be considered as reasonably reliable predictors of where the STZs will appear on the system. To see this correlation, one can compare the plots from column (b) with the plots of column (c) one row below, i.e. plot (2b) with (3c), (3b) with (4c), etc. It is then possible to observe a certain degree of correlation between the jumping atom and the future formation of STZs.

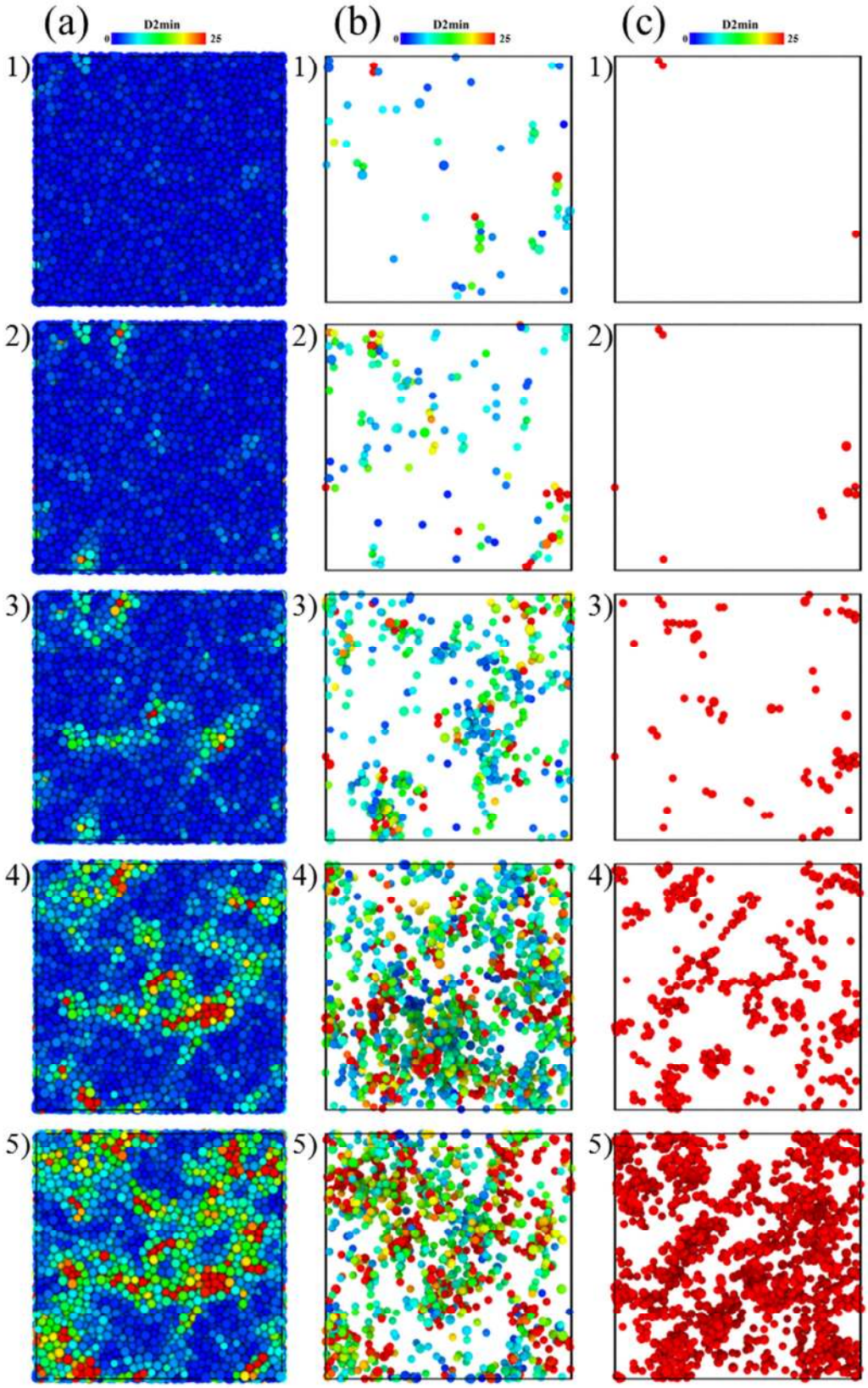

Fig. 5.19) D^2_{min} plots upon straining. Column (a) includes all atoms in the system, column (b) includes only the rattling atoms and column (c) includes those atoms in the system with an extremely large D^2_{min} value (i.e. more than 35 $Å^2$). Each of the five rows corresponds to strain intervals of 2%, from the interval [0%, 2%] represented in row 1 to the interval [8%, 10%] represented in row 5. Each atom is coloured depending on their D^2_{min} value as indicated in the top scale bars, from 0 $Å^2$ (blue) to 25 $Å^2$ (red).

To conclude this chapter, we present a similar set of plots as those illustrated in Fig. 5.19, referring now to the shear stress. It should be noticed that in average, there is not shear stress in our system, i.e. $\sigma_{xy} \approx \sigma_{xz} \approx \sigma_{yz} \approx 0$, where σ_{ij} are the cross terms of the stress tensor, which oscillate around zero. On the other hand, there is local shear stress in regions typically associated with FI [36], [83], [107] or well-shaped, densely packed ICO clusters. In the present work, the shear strain has been calculated as:

$$SH = \frac{|\sigma_{xy}| + |\sigma_{xz}| + |\sigma_{yz}|}{3} \tag{5.3}$$

where the brackets representing the absolute value were introduced to avoid stress cancelations from perpendicular axes. The results are depicted in Fig. 5.20, following a similar scheme as the one of Fig. 5.19, i.e. column (a) includes all atoms in the system, column (b) includes only the rattling atoms and column (c) includes those atoms in the system with an extremely large value of SH (i.e. more than 0.15 MPa). Each of the five rows corresponds to strain intervals of 2%, from the interval [0%, 2%] represented in row 1 to the interval [8%, 10%] represented in row 5. Each atom is coloured depending on their SH value, which was averaged over 200 configurations from the corresponding strain interval. The colour bar goes from 0 MPa (blue) to 0.12 MPa (red). Notice the slight increase of box size in the z direction (vertical) and the reduction of x axis (horizontal). The y axis is not shown since the plots are projections on the xz plane. The length of the box in the z axis goes from 79.7 Å in the quiescent state to 88.1 Å once the strain process is completed, while in the x and y axes, the box length starts, as well, being 79.7 Å and end being 77.0 Å, corresponding to the applied Poisson ratio of 0.34.

As represented in the column (a) of Fig. 5.20, the SH is approximately 0.6 MPa in average for most of the system's atoms. However, it is clear that there are regions where the local SH is considerable larger, almost three times the average value, i.e. 0.15 MPa as depicted from the plots in column (c). Very interestingly, the SH in the system decreases as the strain process progresses and once again, there seems to be more significant differences between the stages represented by the rows 2 to 3, and 3 to 4, than between the stages represented by the rows 1 to 2 or 4 to 5, as in the case of the D^2_{min} plots, remarking again the transition from aging or relaxation to rejuvenation or

disorder that take place when the system is between 4% and 6% strain. Additionally, since there exist a connection between the FI clusters and the local stress in MGs [36], [83], [107], it is possible to consider the regions with the lowest shear stress, i.e. those without plotted atoms in the column (c) of Fig. 5.20, as the regions where the FI are being destroyed, which permit us to locate spatially in the system the regions where the destruction of ICO clusters, monitored in Fig. 5.7, and particularly, the well-fitted ICO, corresponding to the vanishing of the left bump in the ICO error histograms of Fig. 5.8, is happening.

Furthermore, the correlation between low shear regions and rattling atoms is even stronger than that of the rattling atoms and the D^2_{min} depicted in Fig. 5.19. Moreover, the *SH* of the rattling atoms is in general quite similar or even smaller than the average *SH* of all atoms in the system. These two observations further demonstrate that the ICO clusters are destroyed by the atomic rattling movements before the STZs can be formed [107], [127].

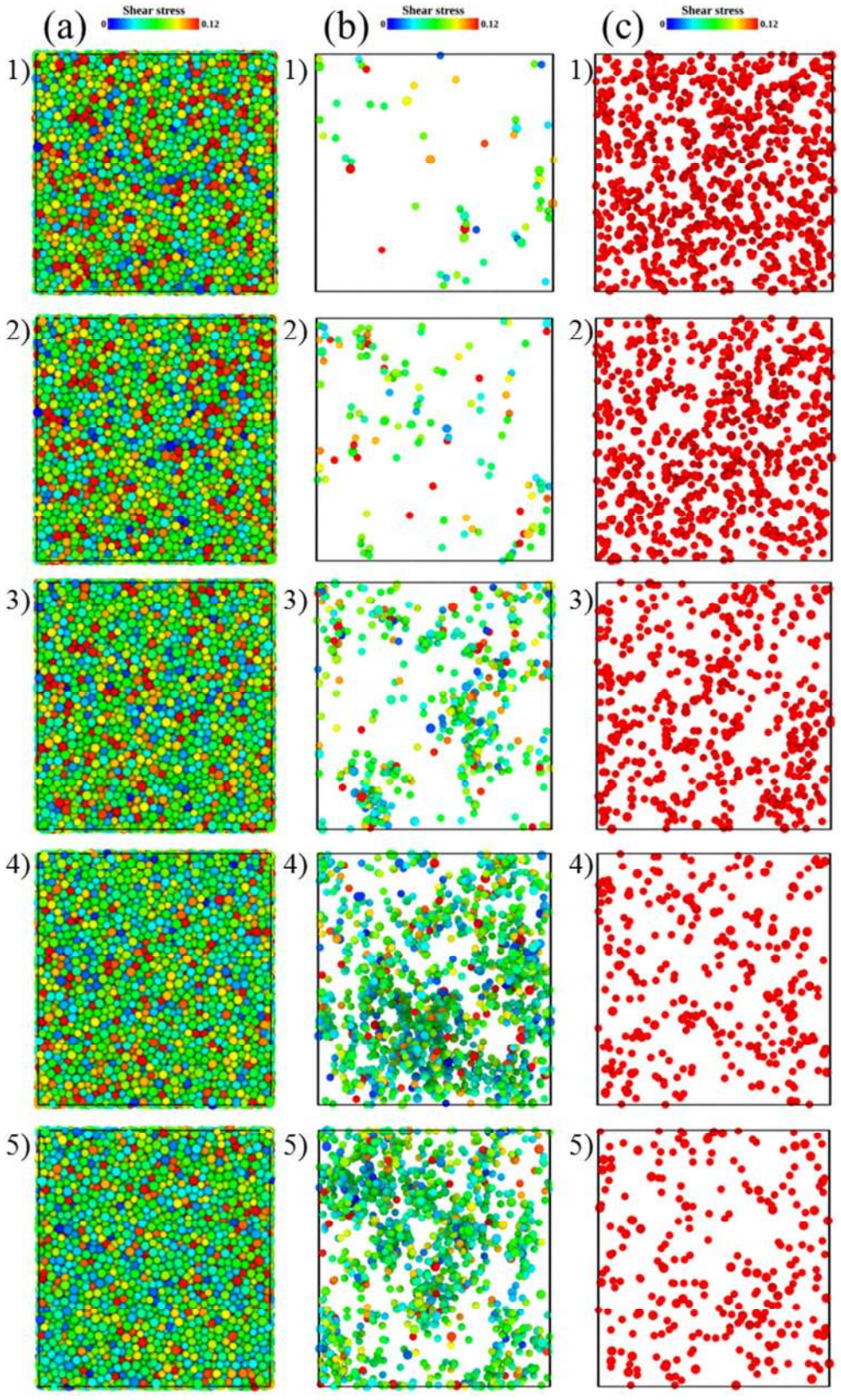

Fig. 5.20) Atomic Shear stress (SH) plots upon straining. Column (a) includes all atoms in the system, column (b) includes only the rattling atoms and column (c) includes those atoms in the system with an extremely large SH value (i.e. more than 0.15 MPa). Each of the five rows corresponds to strain intervals of 2%, from the interval [0%, 2%] represented in row 1) to the interval [8%, 10%] represented in row 5). Each atom is coloured depending on their SH value as indicated in the top scale bars, from 0 MPa (blue) to 0.12 MPa (red).

6) Stress Relaxation

A material shows stress relaxation when the stress decreases with time while a fixed strain is maintained. The study of the structural and dynamical properties at the atomistic level during the stress relaxation may help in gaining insight regarding the viscoelastic and plastic properties of the MGs and, in particular, the aging and rejuvenation mechanisms exhibited by these materials, which would allow to further understand their macroscopic mechanical characteristic.

As a first approximation, we modelled the stress relaxation process by using the Maxwell viscoelastic (or spring-dashpot) model [143]. The Maxwell viscoelastic model states that the stress dependence on time during a relaxation process follows the equation:

$$\sigma(t) = \sigma_0 e^{-\frac{t}{\tau}} + C \qquad (6.1)$$

where τ is the relaxation time, σ_0 is the initial stress and C is a necessary constant introduced in the cases in which the stress does not tend to zero for long (MD) times. Additionally,

$$\tau = \frac{\eta}{k} \qquad (6.2)$$

Where η is the viscosity of the material and k represents its Young modulus. We found that the stress relaxation process taking place in our model glass cannot be characterized by just one relaxation time but rather, by a distribution of relaxation times. For such situations, is it more convenient to fit the data with a stretched exponential or Kohlrausch-Williams-Watts (KWW) model [144], which has the form:

$$\sigma(t) = \sigma_0 e^{-\left(\frac{t}{\tau}\right)^{\beta}} + \sigma_\infty \qquad (6.3)$$

where, τ is the average relaxation time, σ_0 is the initial stress and a stretched parameter, β, is introduced, which accounts for the dispersion of the relaxation times distribution with respect to τ. Notice that for a value of β equals to 1, we recover the Maxwell model. When β is equals to 2, the expression (6.3) becomes a Gaussian function. σ_∞ serves the same purposes as the constant C introduced in the expression (6.1).

For the rest of the chapter, we will use the KWW model to fit the different curves involved in the stress relaxation process. It is important to note that, although the KWW model have been used by many authors to describe relaxation processes in MGs [145]–[149], it is just a phenomenological model without a solid mechanistic argument behind. The main advantage is that it can fit a broad distribution of relaxation times with just three parameters. Additionally, the relaxation time obtained from the KWW model corresponds to the average relaxation time, which may not be the best descriptor of a distribution by itself, especially if the distribution extends over several orders of magnitude. The aforementioned studies refer almost exclusively to experimental results over very different time scales compared to those studied in this dissertation, thus direct comparisons are generally not easily done. Although the relaxation we observed in our systems is orders of magnitude faster than those observed macroscopically, the strain rate we used was also several orders of magnitude faster than the ones generally used in experiments, so it is logical to expect such faster system responses. In fact, the qualitative behaviour of the simulations actually resembles closely to those observed experimentally. Nevertheless, the complete understanding of the stress relaxation processes in MGs is still far from being accomplished. More experimental and MD simulations results are needed to further develop this field and to obtain a more clear picture of the mechanisms behind the macroscopic performances of the MGs.

6.1) Thermodynamics and simulations details

After the straining process, the simulations continued in the Isothermal Isochoric ensemble (NVT) for another 1000 ps, during which the strain was fixed at 10%. Very interestingly, it came out that the systems relaxed part of the stress and the energy accumulated during the straining process (Fig. 6.1). We note at this point that the observed stress and energy relaxation were not found in a test simulation referring to crystalline pure Cu. As a first approximation, we modelled this relaxation process by using the Maxwell viscoelastic (or spring-dashpot) model [143] (orange line in Fig. 6.1). Yet, as it can be seen in Fig. 6.1, the fitted line is not able to capture the complex relaxation dynamics completely, especially at the beginning of the stress relaxation

process, for the reasons mentioned previously in this chapter. The fit line obtained through the KWW model is closer to the data, as depicted with green lines in Fig. 6.1. The Maxwell model fit yielded a relaxation time of 230 ps for the SCS. The KWW model fit yielded as well a relaxation time of 230 ps in the case of the SCS and 210 ps for the FCS, suggesting a slightly faster relaxation time for the system cooled down at a slower rate, which accumulated more stress during the straining process as we saw in the previous chapter. The value of the relaxation time we found differs considerably from the one reported by Qiao *et al*. [28] (approximately 1.5 ns at 350 K), which is understandable, considering the different system temperature and the fact that they performed the fit over 50 ns of stress relaxation data, driving their average relaxation time towards higher values since other mechanisms, with characteristics longer relaxation times, arise.

Notice that the relaxation time obtained through the Maxwell model and the KWW model for the SCS is the same, which is logical if we consider that the Maxwell fit is acceptable for most of the curve length. Under this condition, it represents the main or average characteristic relaxation time of the system, which explains the matching between the two models. If we introduce this relaxation time in equation (6.2) together with the Young modulus (75.5 GPa) obtained in section 5.1), we find a viscosity of 17.35 Pa·s, several order of magnitude away of the typical viscosity of solids (10^{12} Pa·s). Interestingly, the viscosity we obtain for our MG is comparable to the value 10 Pa·s, reported by Zhang *et al*. [89], for the same model glass at 1000 K, which strongly suggest that the stress relaxation we observe is mostly taking place in the liquid-like regions of the system, which have been linked several times in this work with the location of the rattling atoms and the location of defective or loosely packed clusters structures. Additionally, this viscosity is 3 orders of magnitude smaller than the shear viscosity value, of approximately 10^4 Pa·s, reported by Wang *et al*. inside a propagating shear band [135] in $Cu_{50}Zr_{50}$ MGs and by Kang *et al* [118] for the $Cu_{65}Zr_{35}$ model glass under a shear strain of 10%.

The β coefficient was 0.38 for the SCS and 0.74 for the FCS, which indicates, as it is visible in Fig. 6.1, that the different cooling rates have a considerable influence regarding the dispersion of relaxation times from the average. Similar values of β were found by Qiao *et al*. [28] in a $Cu_{46}Zr_{46}Al_8$ model glass over a large range of temperatures: from 350 K to 800 K and by Wang *et al*. [146] at room temperature.

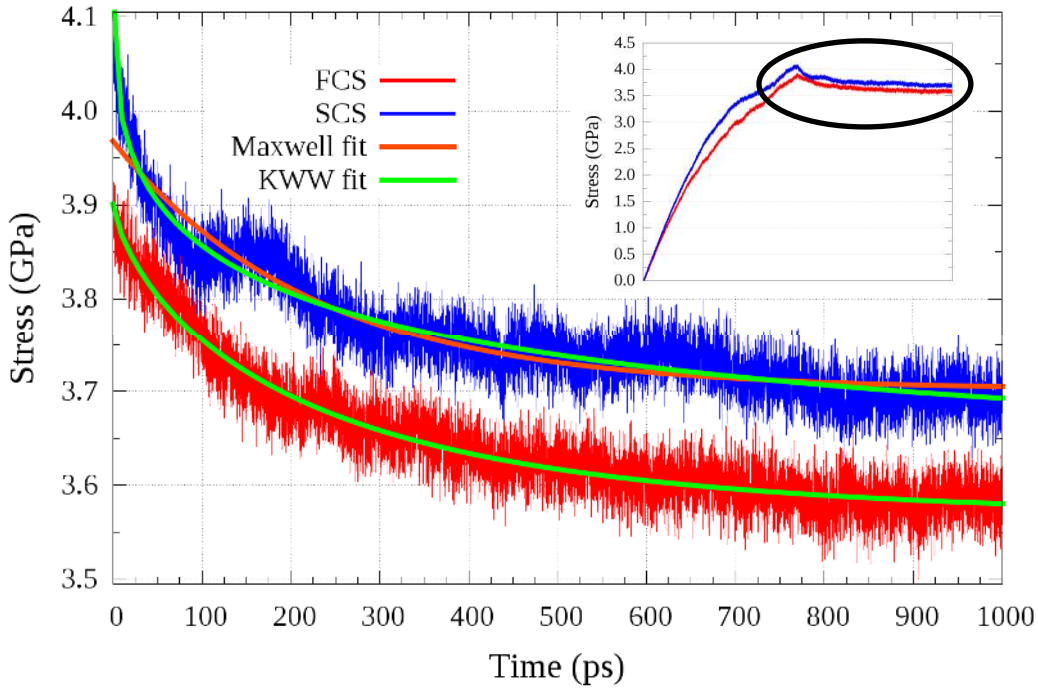

Fig. 6.1) Stress relaxation for the FCS and the SCS while keeping the systems under 10% strain. The SCS Stress decay was fitted to the Maxwell and the KWW models. The FCS was fitted only to the KWW model. In the inset, it is represented the stress for both: the straining and the stress relaxation processes.

Similar decay as the one observed for the stress was also exhibited by the total energy per atom for both, the SCS and the FCS, as illustrated in Fig. 6.2. Although we provide only the total energy, the relaxation is practically the same for the potential energy, suggesting that it is actually the potential energy the one that decreases, given that the kinetic energy was kept constant due to the presence of the thermostat. The KWW fit yielded longer relaxation times in this case: 435 ps and 666 ps for the SCS and the FCS, respectively. The β parameter resulted to be the same in both cases: 0.65. Notice that the total energy per atom was lower by 10 meV in the SCS with respect to the FCS, at the quiescent state (inset of Fig. 6.2), before the straining process, supporting the idea that it was better relaxed due to the slower cooling rate. Interestingly, this difference was reduced to 3 meV per atom once the straining process was completed, which means that the SCS stored more energy during such process. For the rest of the chapter, the results will refer to the SCS unless otherwise specified.

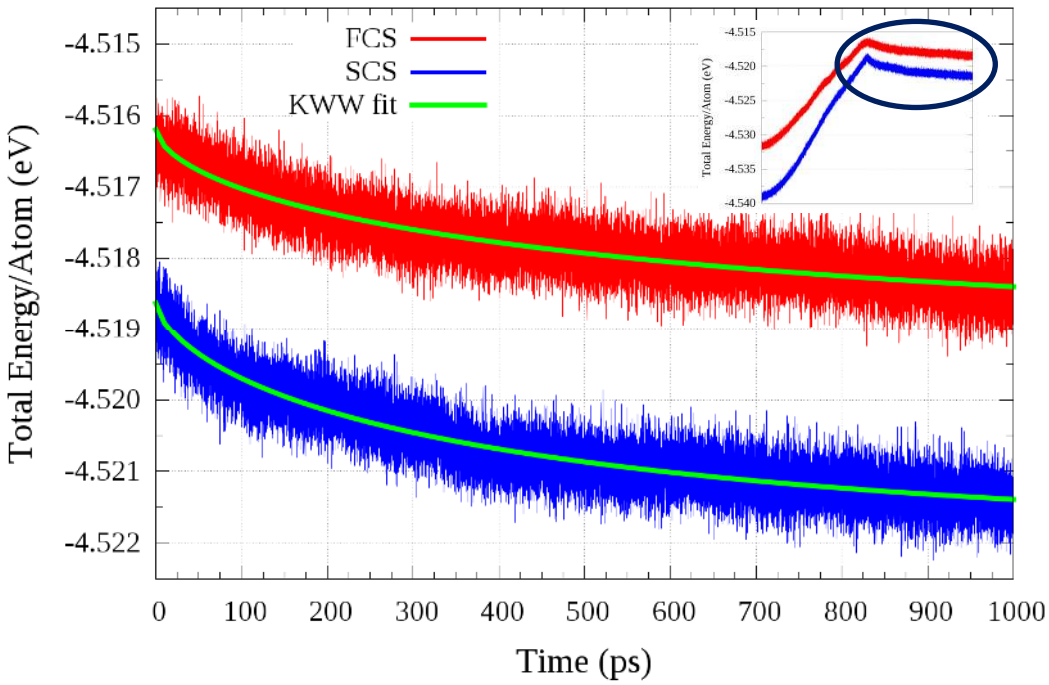

Fig. 6.2) Total energy decay during stress relaxation for the FCS and the SCS while keeping the systems under 10% strain. The curves were fitted to the KWW model. In the inset, it is represented the total energy per atom for both: the straining and the stress relaxation processes.

The influence of the temperature in the stress relaxation process was evaluated for the SCS, and the results are presented in Fig. 6.3 and Table 6.1. In general, it is possible to observe a soft increase in the stress relaxation times with temperature, from 170 ps at 200 K to 380 ps at 600 K, indicating faster stress relaxation for the systems at lower temperatures, which were also more stressed during the straining process.

Furthermore, we studied the impact of the strain rate at which the straining process was performed on the stress relaxation that takes place once the strain is fixed at 10%. The results are illustrated in Fig. 6.4 along with the KWW model fit. The parameters of the fit are summarized in Table 6.1. It came out that this impact is massive and the relaxation times are reduced by orders of magnitude as the strain rate increases (also by orders of magnitude), from 2 ps for a strain rate of 10^{10} s^{-1} to 1000 ps for a strain rate of 10^{7} s^{-1}. Nevertheless, the effect is still present for the slower strain rates, which is expected, as it is also present at experimental time scales and strain rates [28]. The changes of the β parameter from the KWW model are also significantly related with the different strain rates used and they decrease from a value close to 1 for a strain rate of 10^{7} s^{-1} to a value of 0.24 when the strain rate is 10^{10} s^{-1}, which implies that the

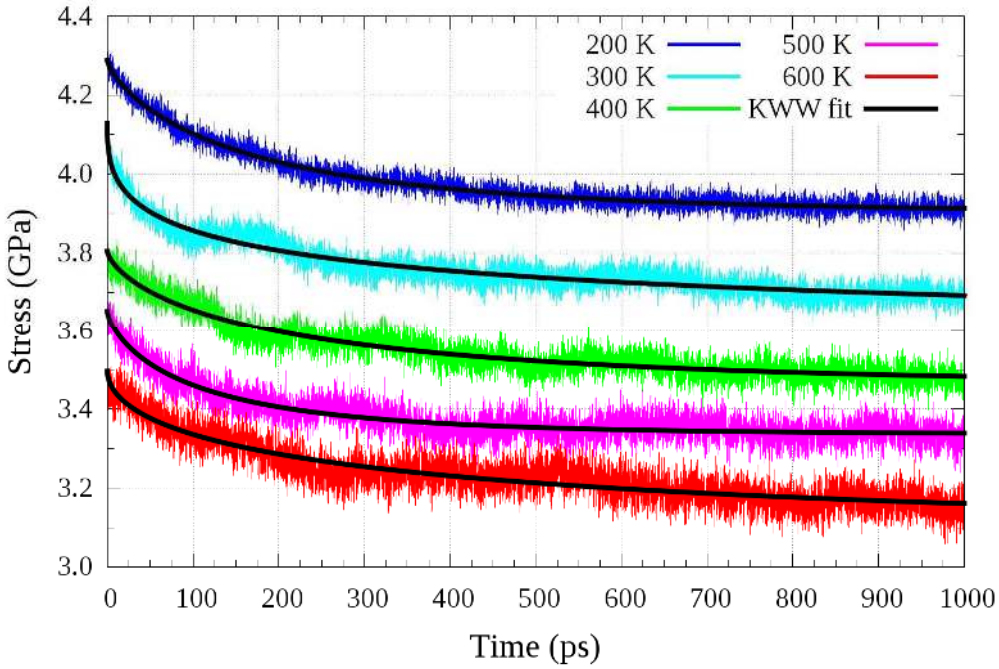

Fig. 6.3) Temperature dependence of the Stress relaxation, ranging from 200 to 600 K. Systems with lower temperature were considerably more stressed at the end of the straining process (see inset of Fig. 5.3) and they relaxed the stress faster. Notice the "bumps" in the stress relaxations curves, indicating a collection of different relaxation times taking place.

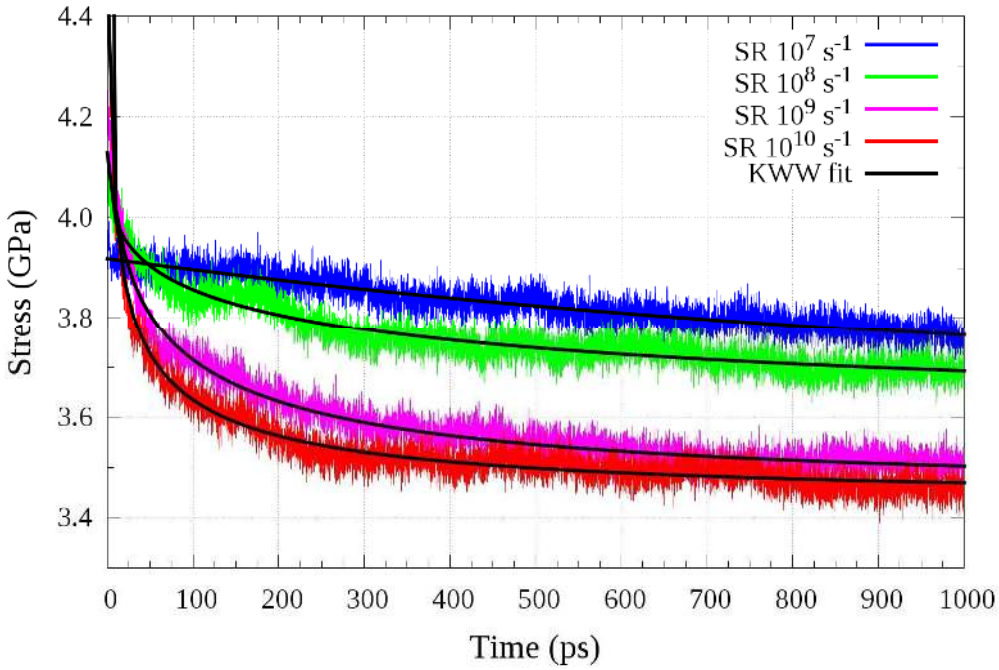

Fig. 6.4) Dependence of the Stress relaxation for different strain rates (ranging from 10^{7} s^{-1} to 10^{10} s^{-1}) during the straining process. Faster straining rates induce faster stress relaxations.

dispersion of relaxation times with respect to the average is small when the strain rate is low but very significant for faster strain rates. Curiosly, it appears that the difference between strain rates of 10^8 s^{-1} and 10^9 s^{-1} is considerable larger than between strain rates of 10^9 s^{-1} and 10^{10} s^{-1} or of 10^7 s^{-1} and 10^8 s^{-1}, suggesting that, in order to extract conclussions that are closer to the experimental situation it is significanlty better to use a strain rate of 10^8 s^{-1} instead of a strain rate of 10^9 s^{-1}.

We close this chapter section presenting the dependency of the stress relaxation regarding the target strain reached during the straining process (Fig. 6.5 and Table 6.1). For a target strain slightly higher (2%) than the elastic regime of our system (~1.4%) the stress relaxation is barely visible, with a relaxation time of 110 ps and a very large β parameter of 1.77. As we increase the target strain, the relaxation time increases as well and the β parameter decreases significanlty, which complicates the comparison of the relaxation times for the different target strains. Nevertheless, it is clear from Fig. 6.5 that the stress relaxation is more pronounced for target strains of 6% and higher, when the endothermic behaviour of the system is completed and the system is well inside the plastic regime. In fact, a "step" of the β parameter of the fit is appreciable for a target strain of 6%: from β equal to 1.77 for a target strain of 2%, to β equal to 0.57 for a target strain of 5%, then the value of β increases slightly to 0.68 for a target strain of 6% and from there it decreases again until it reaches the value of 0.38, corresponding to a target strain of 10%. This behaviour reinforces the idea that there are indeed strong differences in the system below and over 6% strain, as stated in the previous chapter.

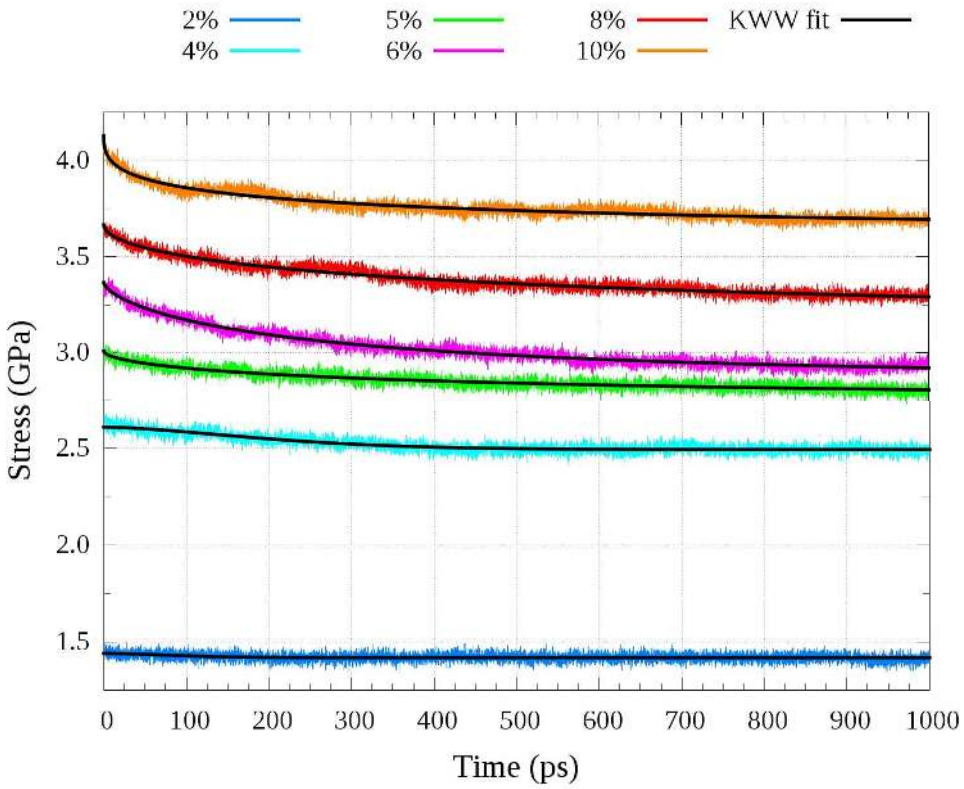

Fig. 6.5) Stress relaxation curves for systems strained up to different target strains. The stress relaxation of the system strained a little further (2%) than the elastic regime of our system (1.4%) is barely visible. The stress relaxations for target strains of 6% and higher (i.e. when the endothermic behaviour presented in the previous chapter finished) are considerably more pronounced than in the case of the systems that were strained up to less than 5%.

Fitting parameters on T.		
T (K)	**τ (ps)**	**β**
200	174	0.75
300	232	0.38
400	225	0.69
500	111	0.71
600	377	0.53

Fitting parameters on SR.		
SR (s^{-1})	**τ (ps)**	**β**
10^7	1003	1.03
10^8	232	0.38
10^9	41	0.36
10^{10}	2	0.24

Fitting parameters on target strain		
Target Strain (%)	**τ (ps)**	**β**
2	110	1.77
4	242	1.58
5	426	0.57
6	272	0.68
8	556	0.54
10	232	0.38

Table 6.1) Parameters of the KWW fit for the SCS for different temperatures, strain rates and target strains.

6.2) Structural analysis

Similarly to the previous chapters, we focus now on the analysis of the structural evolution of the SCS upon stress relaxation. First, we calculated the RDF and PRDFs at the end of the stress relaxation process and compared it with the ones calculated at the end of the straining process (Fig. 6.6). The output is that they are practically identical in all cases, which means than the distances between atoms have not changed, in average, inside the system. Notice that if there were local changes, they would be hardly perceptible in the RDF and PRDFs due to the fact that the volume of the system was kept constant upon stress relaxation, thus local density increases must be compensated with local density decreases somewhere else in the system, resulting in a constant average density.

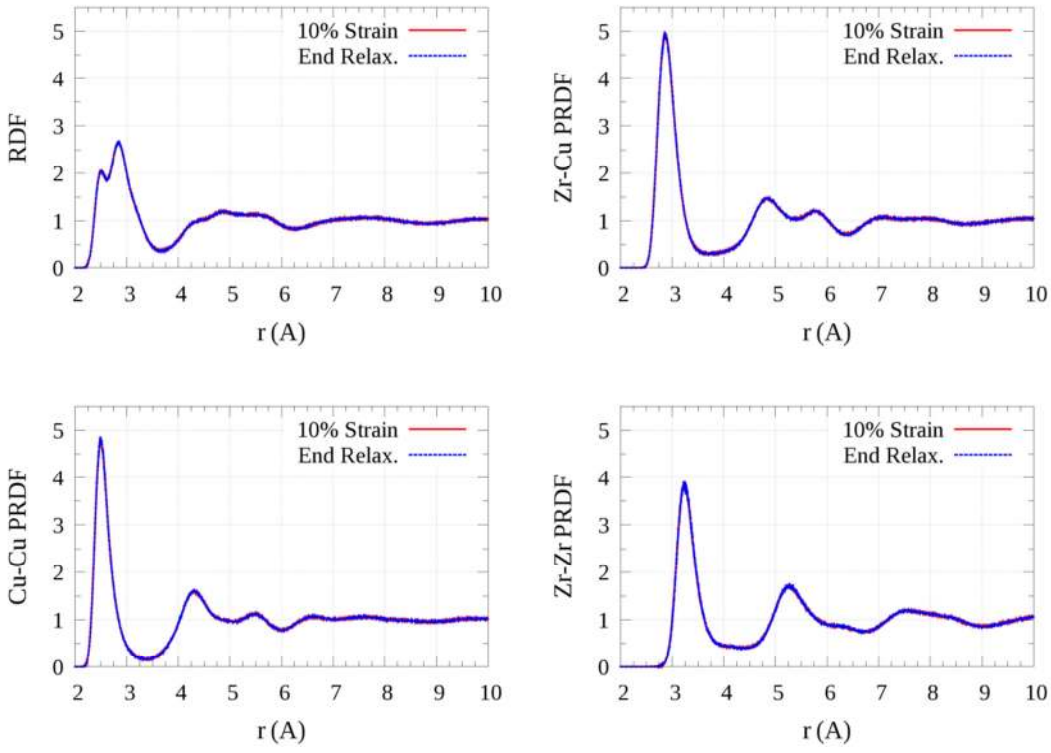

Fig. 6.6) PRDFs for the different pairs of elements and total RDF of the SCS under 10% strain and at the end of the relaxation process. No differences can be observed.

Second, we studied the clusters evolution in time during the stress relaxation (Fig. 6.7). Once again, the differences are hardy visible and they are well inside the error bar in all

cases. In any case, the number of Zr RD and ICO clusters remains practically equal. The number of Zr CUB clusters seems to decrease at the end of the relaxation process, although the difference between the starting and ending populations is only 0.1%. In the case of Cu atoms, the trends in the very beginning of the stress relaxation process look like a continuation of the trends exhibited by the system during the straining process (Fig. 5.7), i.e. an increase of the number of loosely packed clusters (RD and Cu centred CUB) and a decrease of the densely packed ones (ICO and Zr centred CUB), suggesting that the disordering (or rejuvenation) of our system, initiated during the straining process, extends into the stress relaxation process, which may indicate a certain inertia that disappears after 300-400 ps, when the very fast initial stress relaxation have been completed.

The differences on which we commented in the previous paragraph are generally inside the error bars and they are so small that cannot be seen when we compare the histograms of the clusters fit errors at the beginning and at the end of the stress relaxation process, as depicted in Fig. 6.8, where no significant changes can be appreciated.

The destruction of Superclusters continues too during the first 100 ps of the stress relaxation process, indicating that the existent inertia exhibited in the number of clusters seen in Fig. 6.7 affects the Superclusters as well. However, it seems to be less intense in the case of the Superclusters, which show signs of recovery from 100 to 300 ps. Nevertheless, the number of Superclusters seems to be oscillating around the same quantity reached at the end of the straining process. In any case, once again, all changes are inside the error bars.

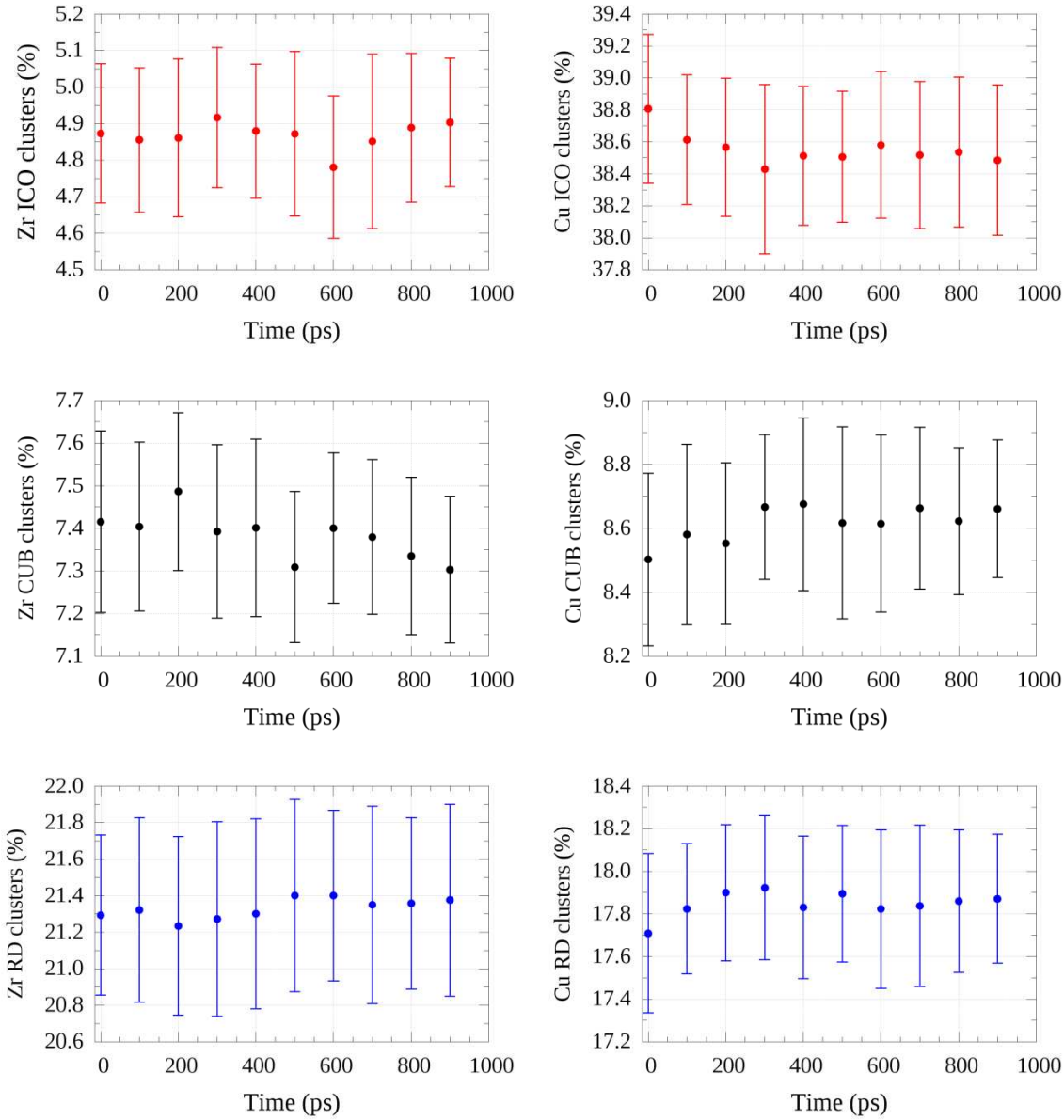

Fig. 6.7) Clusters evolution upon relaxation. All changes are inside the error bar. The trends observed during the straining process continue, more markedly, for the Cu centred clusters indicating that there exists some kind of inertia. In general there are no significant changes.

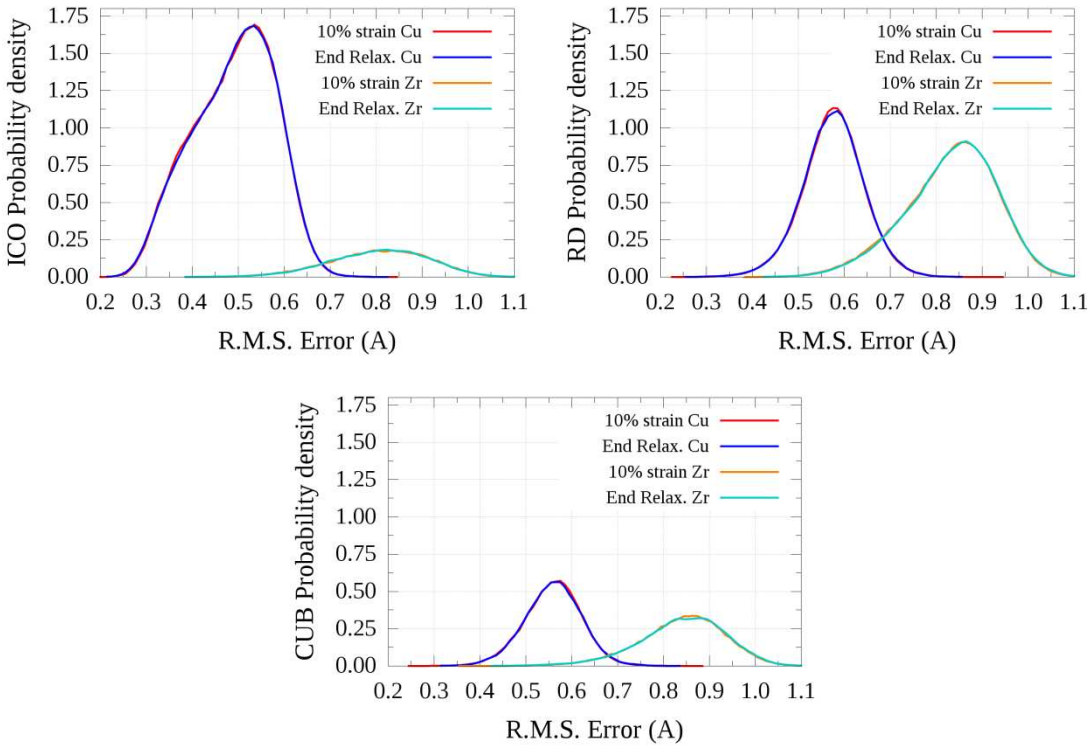

Fig. 6.8) Comparison of the clusters error histograms before and after the relaxation process. No significant changes can be observed.

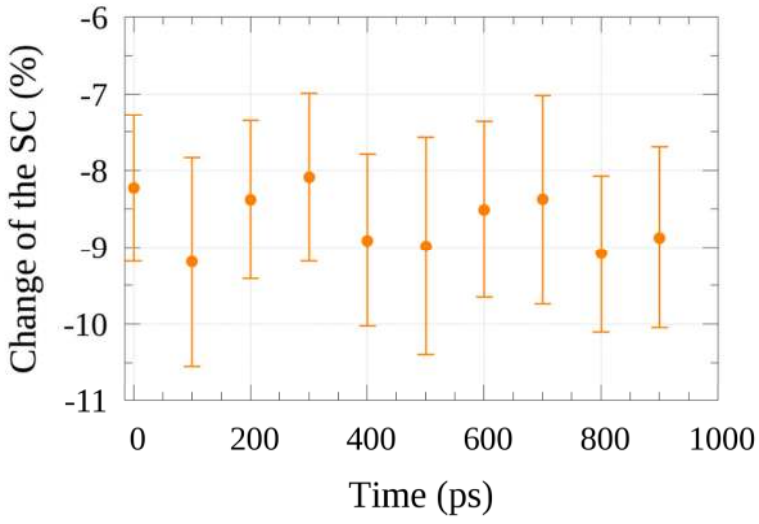

Fig. 6.9) Evolution of the total number of Superclusters (SCs) upon relaxation with respect to the total number of Superclusters at the quiescent state). Superclusters keep being destroyed during the first 100 ps of the relaxation process. Then, there is a moderate recovery of 1% during the following 300 ps. However these changes are inside the error bar and they are not very significant.

Fig. 6.10 is an extension of Fig. 5.11 into the stress relaxation process. The CN of Cu atoms drops towards the value at the quiescent state during the first 500 ps and then it reaches a plateau, indicating that the number of neighbours of Cu atoms is 0.15% larger at the end of the stress relaxation process with respect to the quiescent state. In the case of Zr atoms, the inertia previously mentioned in this chapter seems to be present as well, since the CN keeps increasing a little further over a change of 0.8% with respect to the quiescent state. After that there are not many changes. In general, it seems to exist a certain degree of correlation between the bumps on the stress illustrated in Fig. 6.1 and the CN for both, Cu and Zr atoms.

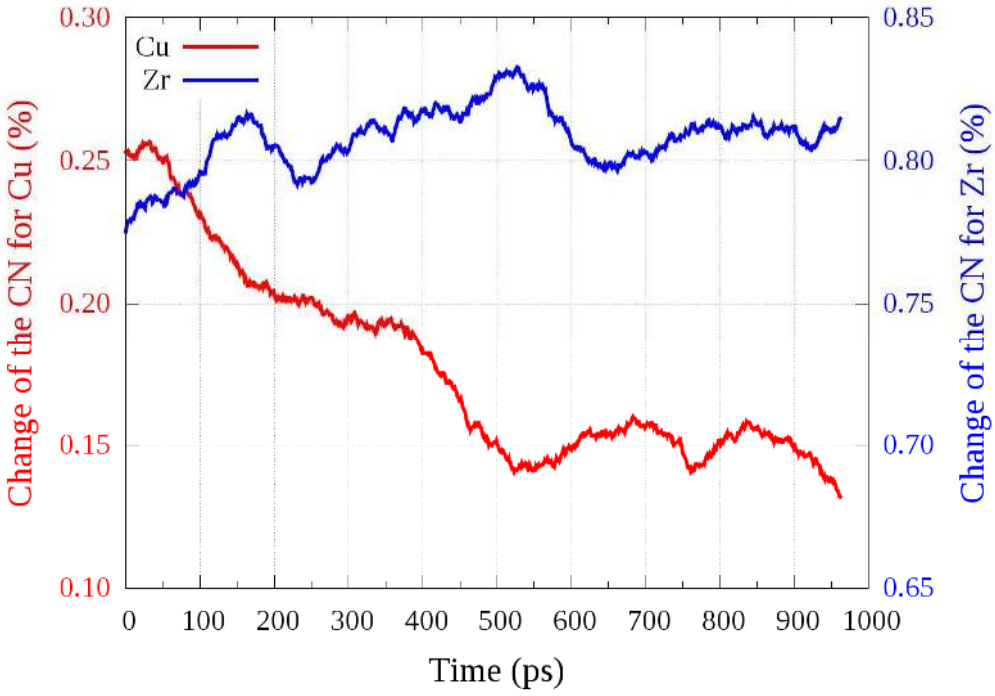

Fig. 6.10) Variation with respect to the number of Voronoi faces (i.e. CN) upon relaxation. A 0% change represents the number of VFs at the quiescent state. During the first 500 ps of the relaxation process, the CN of Cu atoms decreases in 0.1 % and remains 0.15 % higher than at the quiescent state. The CN of Zr atoms remains approximately at the same value reached during the straining process.

A partial recovery of the 2STDL and 2STDR areas anomaly is also observable during the stress relaxation process with respect to the trends exhibited for the strain process. However, the total differences are rather small compared to the changes that took place during the straining process.

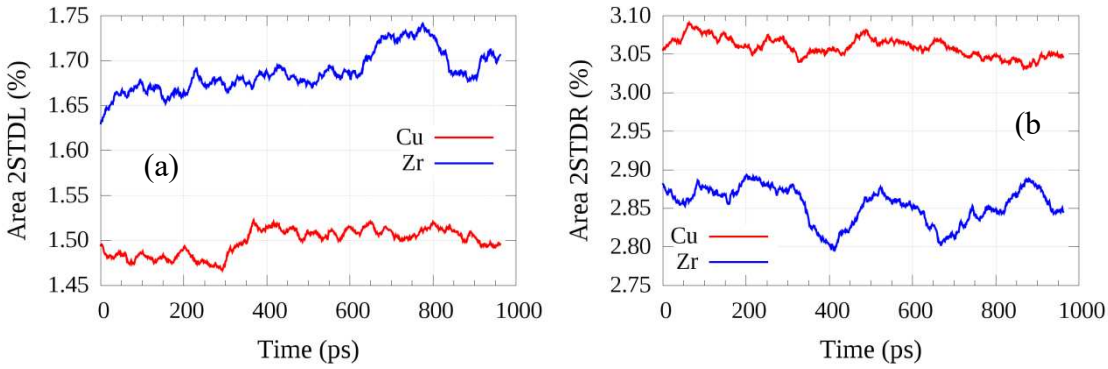

Fig. 6.11) Evolution upon relaxation of the area of the Voronoi Volume Gaussians under (a) and over (b) 2 standard deviations for Cu and Zr. Opposite trends to those found during the straining process can be observed, although they are significantly less pronounced

6.3) Dynamics analysis

In the previous section, we have analysed the structure of the SCS and we have seen that, despite the considerable stress and energy relaxation occurring in the system just after the conclusion of the straining process, there are not significant changes concerning the SRO and MRO at the studied time scales. Nevertheless it was possible to observe a slight recovery of the volume anomaly (measured through the 2STDL and 2STDR areas) and the CN of Cu atoms with respect to the trends observed during the straining process. It was also manifested, through the destruction of densely packed clusters and creation of loosely packed ones, some degree of inertia regarding the rejuvenation process that took place in the medium to the last stages of the strain procedure. Since the relaxations of stress and energy are not obvious in the microstructure analysis, they must be related with the dynamics of our system, which will be evaluated in this section. Once again, as in section 5.3), the rattling atoms are those atoms that jump at least once during the whole stress relaxation process. Following that classification, 16.3% of the atoms in the system are rattling atoms, from which 12.5% are Cu atoms and 3.8% are Zr atoms.

First, we present the results of the SD calculated for all atoms in the system, for Cu and Zr separately and for the rattling atoms (Fig. 6.12). The SD during the stress relaxation process is markedly different from the SD calculated for the straining process (Fig.

5.13). In this case, we observed very fast dynamics at the beginning of the stress relaxation process and they progressively slow down. The SD slope of the rattling atoms decreases at approximately 50 ps and 350 ps. On the other hand, the SD of the system in average exhibits a response having the opposite trend depicted for the stress relaxation in Fig. 6.1, i.e. and increases up to 100 ps, followed by a small plateau and a new increase at around 150 ps. The slope of the SD for the system diminishes again at approximately 350 ps, coinciding with the end of the second decline of the stress observed in Fig. 6.1. From the inset of Fig. 6.12, in which the x axis is in logarithmic scale, it is possible to appreciate the cage breaking effect, first for the rattling atoms at around 5 ps and then for the rest of the atoms in the system at around 10 ps.

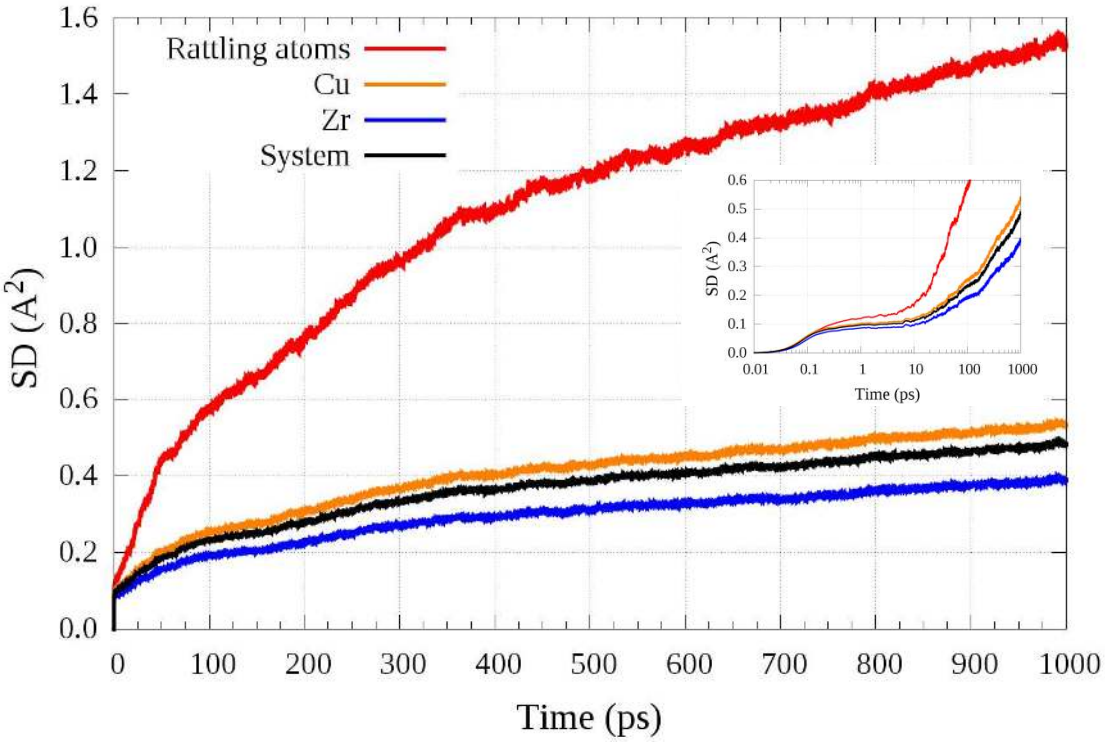

Fig. 6.12) SD for all atoms in the system, separately for Cu and Zr and for the rattling atoms upon relaxation. In the inset the x axis is in logarithmic scale. Rattling atoms break the cage at around 5 ps, as indicated by the upturn in their SD in the inset. They are diffusing from the very beginning (the were diffusing at the end of the straining process) and the slope of their SD decreases at 50 and 350 ps, i.e. just before the faster stress relaxation ends and after a slower decrease of the stress happens (see Fig. 6.1) . The rest of the atoms in the system start breaking the cage after the rattling atoms, at around 10 ps and similar trends can be observe regarding their SD with that of the rattling atoms, although considerably less pronounced and in a lower magnitude.

The time evolution of the Overlap parameter for the stress relaxation process (Fig. 6.13) has also notably different shape than that of the straining process (Fig. 5.14). In this case, we see that the system configurations differ greatly from the reference configuration at very short times and then the rate at which Q diminish, decreases. Similar trends at similar time intervals with respect to the stress relaxation (Fig. 6.1) are observable regardless of the applied cutoff *d*. The relaxation times are again lower than 1 ps when the cutoff is 0.2 Å or less. Then they increase considerably for each increment in the distance cutoff, from 35 ps when d = 0.25 Å to 735 ps for a cutoff of 0.35 Å. The differences in the length of the plateau between the straining and stress relaxation processes are also remarkable, clearly perceptible in the logarithmic plots (Fig. 5.14(b) and Fig. 6.13(b) respectively). The length of these plateaus is related with the time length of the relaxation processes taking place in the system, which are significantly shorter for the stress relaxation phase than for the straining process.

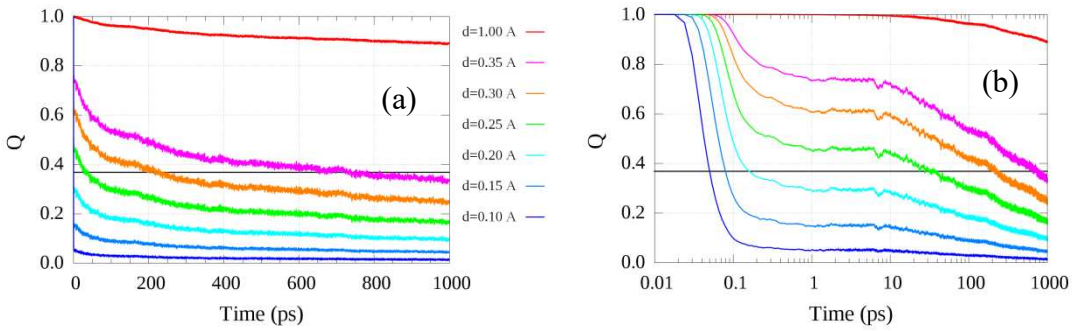

Fig. 6.13) (a) System's Overlap parameter versus time during the relaxation process for different thresholds and (b) same as in (a) with logarithmic scale in the x axis. The behaviour of the overlap parameter resembles very similar trends at the same time intervals as those of the stress relaxation (Fig. 6.1). All the relaxation times obtained are summarized in Table 6.2.

Similar behaviour can be seen when we calculate the overlap parameter for the rattling atoms (Fig. 6.13) within the tolerance of larger values of the cutoff. Only for a cutoff of 0.2 Å we find a relaxation time of less than 1 ps and, once again, the relaxation times increase significantly for small increments in the cutoff distance, e.g. for a cutoff of 0.4 Å the relaxation time is 155 ps, while for a cutoff of 0.8 Å, the relaxation time is 990 ps. For larger values of the cutoff, the length of our simulation is not enough to capture the local relaxation around rattling atoms. Once again, the length of the plateau

manifested in the logarithmic scale plots is remarkably shorter for the stress relaxation process (Fig. 6.14(b)) than for the straining process (Fig. 5.15(b)).

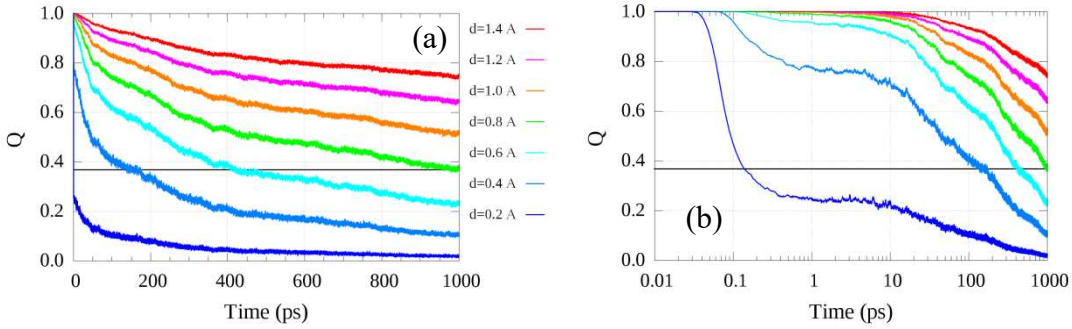

Fig. 6.14) (a) Overlap parameter versus time for the rattling atoms for different thresholds (longer than in the previous figure for the whole system) and (b) same as in (a) with logarithmic scale in the x axis. All the relaxation times obtained are summarized in Table 6.2.

Turning on the MSD of rattling atoms (Fig. 6.15), we can see that in the case of the stress relaxation process, the rattling atoms are also diffusing with a diffusion coefficient of $1.7 \cdot 10^{-8}$ cm^2/s, which is slightly smaller than the diffusion coefficient we obtained for the straining process ($3.6 \cdot 10^{-8}$ cm^2/s). As in the case of the straining process, most of the rattling atoms jump less than 1 Å. The cage breaking phenomena take place between configurations separated by approximately 7 ps in general for the rattling atoms. Atoms jumping more than 1 Å break the cage after shorter times of approximately 5 ps (inset of Fig. 6.15).

The overlap parameter (Q) averaged over the whole stress relaxation trajectory is presented for the rattling atoms in Fig. 6.16. It turns out that the relaxation times (Table 6.2) are much larger for the stress relaxation process than for the straining process as it can be seen comparing Fig. 6.16 and Fig. 5.17). For the time scale studied in our simulations, the relaxation times corresponding to a cutoff of more than 0.4 Å can only be obtained for the cutoff distance of 0.6 Å (575 ps) and 0.8 Å (960 ps). For larger values of the cutoff, longer simulations are required.

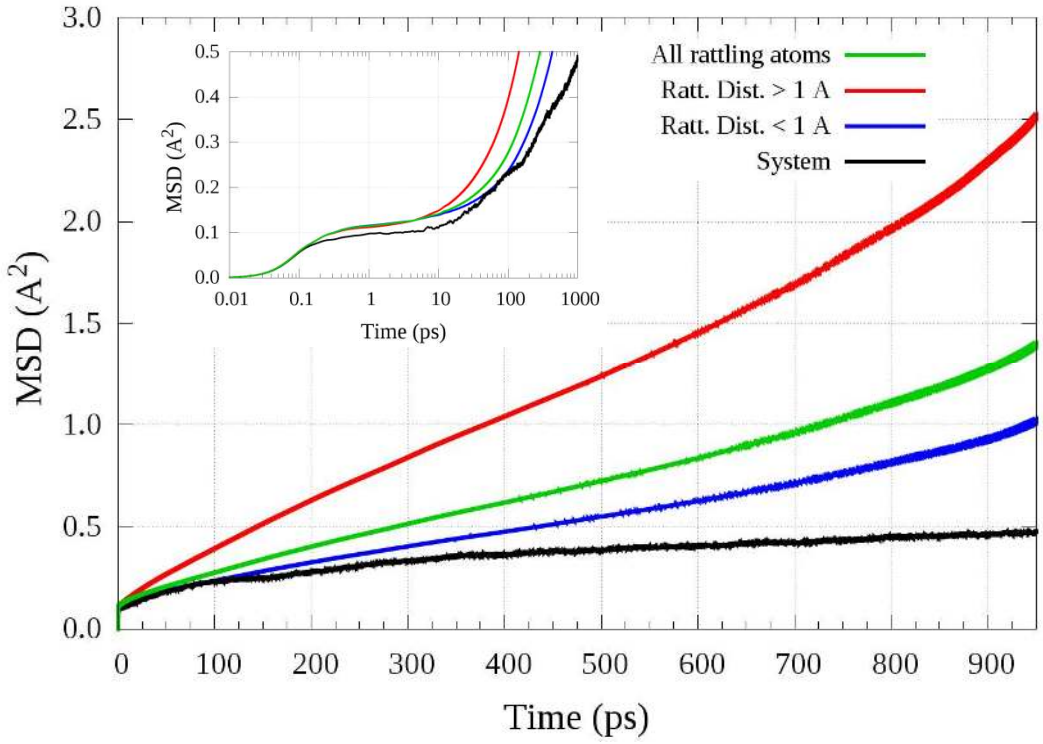

Fig. 6.15) MSD for all the rattling atoms and separately for atoms that jumps more or less than 1 Å. The system SD is also plotted for reference (black line). In the inset, the x axis is plotted using a logarithmic scale. Rattling atoms diffuse with a diffusion coefficient of $1.7 \cdot 10^{-8}$. Most of the rattling atoms perform jumps of less than 1 Å. The inset shows that rattling atoms breaks the cage at around 7 ps (in average along the entire trajectory, i.e. all the relaxation process). Atoms jumping more than 1 Å break the cage even sooner, at around 5 ps.

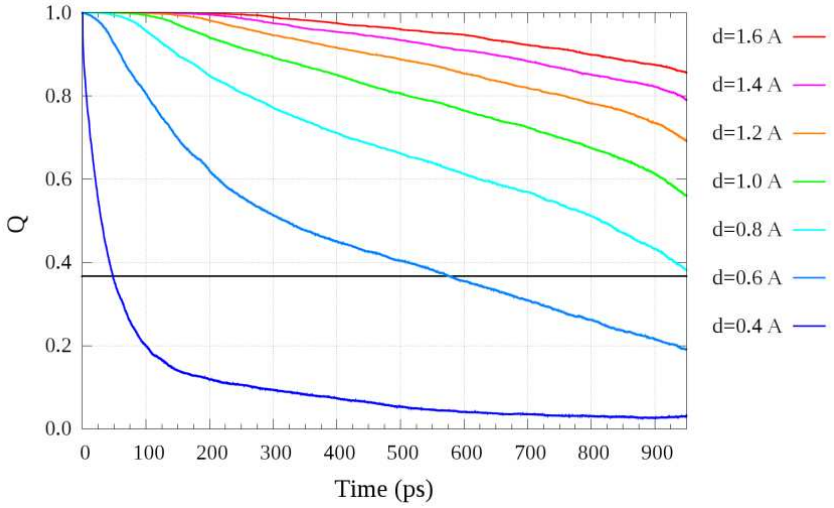

Fig. 6.16) (a) Overlap parameter versus time for the rattling atoms using their MSD (i.e. averages over the entire relaxation process) for different thresholds. All the relaxation times obtained are summarized in Table 6.2.

System		SD Rattling atoms		MSD Rattling atoms	
Cutoff *d* (Å)	**Rel. time τ (ps)**	**Cutoff *d* (Å)**	**Rel. time τ (ps)**	**Cutoff *d* (Å)**	**Rel. time τ (ps)**
0.10	0.05	0.2	0.14	0.4	47
0.15	0.08	0.4	156	0.6	575
0.2	0.16	0.6	420	0.8	960
0.25	35	0.8	990	1.0	--
0.3	223	1.0	--	1.2	--
0.35	735	1.2	--	1.4	--
1.0	--	1.4	--	1.6	--

Table 6.2) Relaxation times obtained from the overlap parameter decay upon stress relaxation

Finally, we present the histogram of the rattling movements on time for the stress relaxation process along with the corresponding KWW fit (Fig. 6.17). Since the volume of the system was kept constant during the stress relaxation process, there were no affine displacements and the FOC depicted in Fig. 6.17 is significantly more accurate than the FOC obtained upon straining (Fig. 5.18). The number of jumps seems intrinsically correlated with the stress relaxation exhibited by our system in Fig. 6.1 and the SD depicted in Fig. 6.12. The behaviour of the FOC is composed by a very fast decay during the first 100 ps, followed by a plateau that lasts up to approximately 350 ps and a posterior slower decay that extends until the end of the simulation. The fit parameters indicate a relaxation time of approximately 20 ps, which is ten times shorter than the relaxation time corresponding to the stress decline, with a similar β parameter, e.g. 0.39. Interestingly, a relaxation time of 20 ps corresponds with a frequency of 50 Ghz, very similar to the FOM measured for the rattling atoms, which showed very little dependency on temperature or strain.

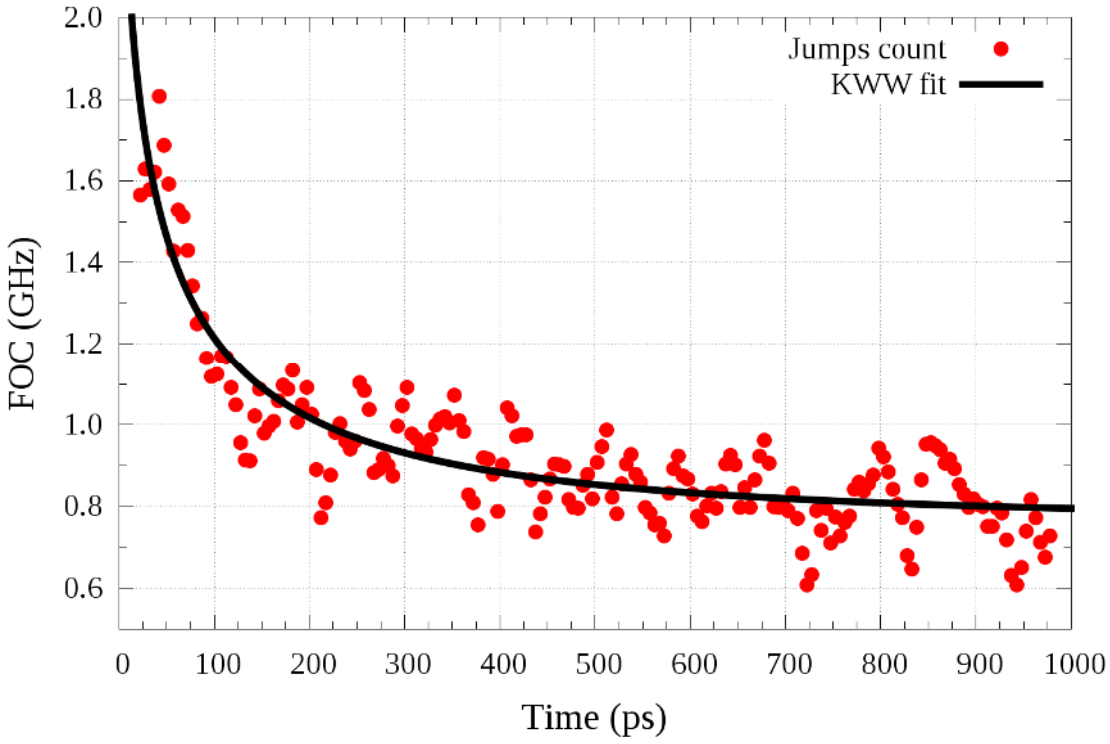

Fig. 6.17) Histogram of the Rattling movements vs time for the stress relaxation process and KWW fit. The FOC on the atomic rattling decreases exponentially with time.

To further investigate the connection between the thermodynamics, the structure and the dynamics of the system with the rattling movements and its evolution upon stress relaxation, we proceeded with the way we did it in the previous chapter and produced a set of plots like those depicted in Fig. 5.19 and Fig. 5.20. Fig. 6.18 represents the spatial distribution of the stress differences corresponding to the zz component of the stress tensor, i.e. $\Delta\sigma_{zz}$, versus time for different stress relaxation stages. In this case, each row represents an interval of 200 ps. For example, the first row refers to the interval [0, 200 ps, the second row refers to the interval [200, 400] ps, etc. However, instead of performing an average for each atom over the 200 configurations of each interval, as we did in Fig. 5.19 and Fig. 5.20, for the data depicted in Fig. 6.18, we performed two averages in each time interval, one over the first 100 ps of the time interval and another one over the last 100 ps of the same time interval (using 100 configurations for each of the two averages). For example, the third row, which corresponds to the time interval [400, 600] ps, represents the difference of the stress component $\Delta\sigma_{zz}$, for each atom, calculated by subtracting the atomic σ_{zz} averaged over 100 configurations from 400 ps to 500 ps, from the atomic σ_{zz} averaged over 100 configurations from 500 ps to 600 ps.

Then the colours of the atoms are selected according to this difference, as depicted in the colour bar, from -0.05 MPa (blue) to 0.05 MPa (red). Once again, column (a) includes all atoms in the system, column (b) includes only the rattling atoms and in this case, column (c) includes those atoms in the system with very large (positive or negative) stress differences (i.e. less than 0.1 MPa or more than 0.1 MPa). From Fig. 6.1, it is evident that the $\Delta\sigma_{zz}$ values decrease with time, as it is reflected as well on column (a) of Fig. 6.18, where for most of the atoms, the $\Delta\sigma_{zz}$ values are very close to zero (green atoms). More interesting is the fact the regions where there are significant changes in the stress are highly localized. Following the opposite trend from the one found upon straining, these regions percolate in the beginning of the stress relaxation process and progressively become isolated as the system becomes more relaxed. Moreover, regions with the largest positive $\Delta\sigma_{zz}$ tend to be next to regions with the largest negative $\Delta\sigma_{zz}$ values, suggesting that in fact, they should both be considered just as regions with a high stress flow, i.e. the regions where the stress is being released upon relaxation. Notice that the atoms with very small $\Delta\sigma_{zz}$, which are connected with the ICO clusters [36], [83], [107], form a network that resembles the backbone of the MGs described by Cao *et al*. [127] which grows upon relaxation, confirming that the system is indeed aging, which was not possible to doubtlessly conclude from the structural analysis depicted in Fig. 6.7 and Fig. 6.8. Nevertheless, the evolution of this backbone depicted in Fig. 6.18 may represent the first steps towards a mild recuperation of the icosahedral structure, which was severely damaged during the last stages of the strain process, suggesting that such recuperation could be observed if longer simulations are performed.

The correlation between the rattling atoms and the atoms with the highest stress flow is astonishing. Practically the same patterns are exhibited in each row of columns (b) and (c), supporting the conclusion extracted from Fig. 5.20: that the rattling atoms are the stress mediators of the system, through which the stress is released.

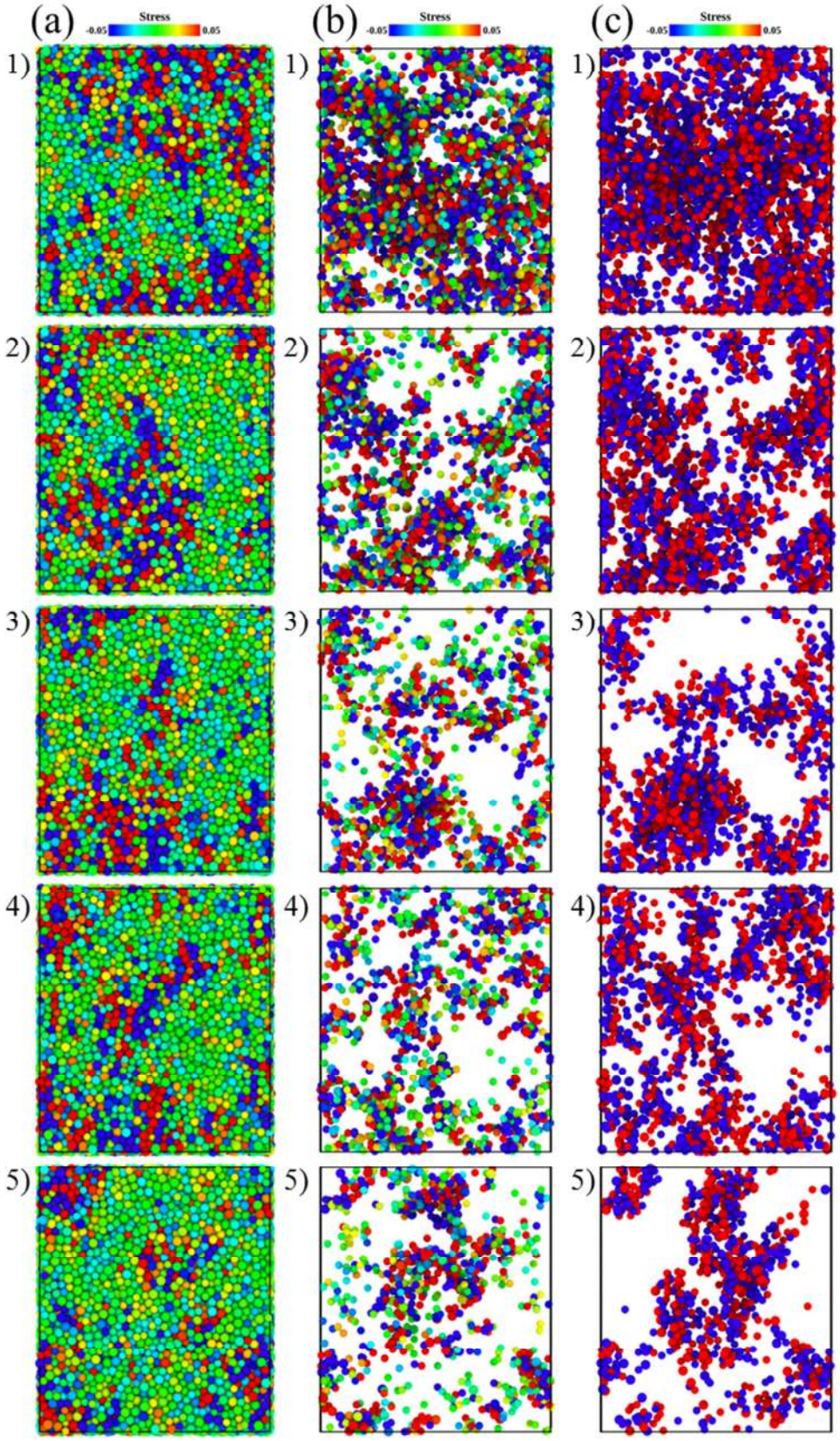

Fig. 6.18) Atomic stress differences ($\Delta\sigma_{zz}$) plots upon stress relaxation. Column (a) includes all atoms, column (b) includes only the rattling atoms and column (c) includes those atoms with a large positive or negative $\Delta\sigma_{zz}$ value (i.e. $|\Delta\sigma_{zz}| > 0.1$ MPa). Each of the five rows corresponds to a time interval of 200 ps. Each atom is coloured depending on their ($\Delta\sigma_{zz}$) value, as indicated in the top scale bars, from -0.05 MPa (blue) to 0.05 MPa (red).

During the stress relaxation process, a portion of the total energy of the system accumulated upon straining was also released (Fig. 6.2). As we previously stated, the potential energy (U) of the system decreased as well in the same manner. Aiming in determining whether the decay of U was spatially localized as in the case of the stress, we followed the same procedure as in Fig. 6.18, using as input the atomic potential energy (Fig. 6.19). Because the potential energy is significantly different for Cu and Zr atoms, we divided the atomic potential energy differences, ΔU, by the initial value at each interval, i.e. the value of U averaged over the first 100 ps of each time interval. For this reason, the colours of the atoms plotted in Fig. 6.19 represent their ΔU in %, ranging from -0.5% (blue) to 0.5% (red) as indicated in the scale bars on top. The rest of the scheme is exactly as in Fig. 6.18, except that in this case, column (c) includes the atoms for which $|\Delta U| > 1\%$. The behaviour depicted in Fig. 6.19 is practically identical to the one exhibited by the stress differences illustrated in Fig. 6.18, thus it appears that the stress and potential energy relaxations are carried out almost exclusively by the rattling movements, described in detail along this dissertation, as the fast relaxation processes that precede slower relaxation modes such as the fast β' and slow β.

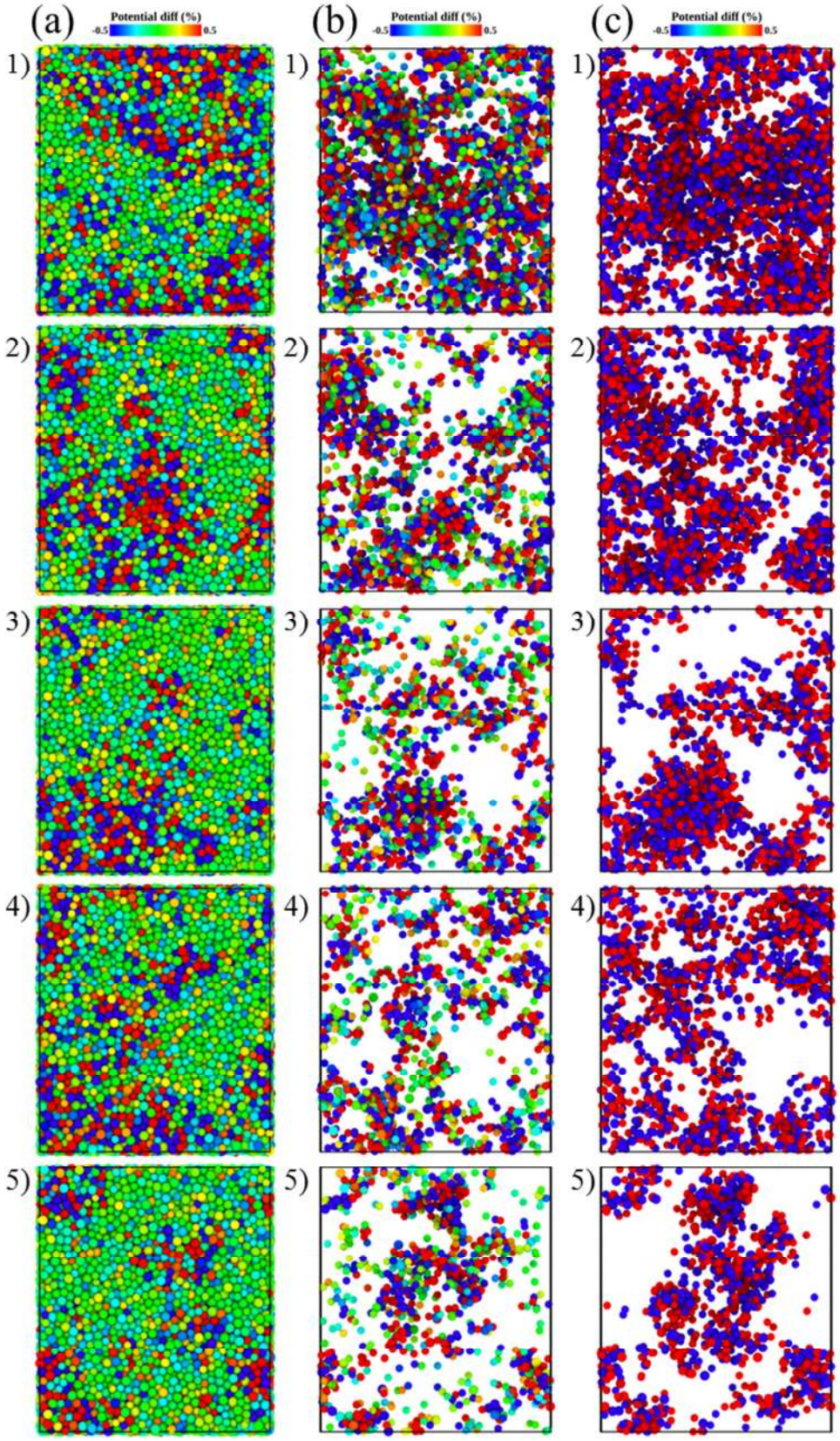

Fig. 6.19) Atomic Potential energy differences (ΔU) plots upon stress relaxation. Column (a) includes all atoms, column (b) includes only the rattling atoms and column (c) includes those atoms with a large positive or negative ΔU value (i.e. $|\Delta\sigma_{zz}| > 1\%$). Each of the five rows corresponds to a time interval of 200 ps. Each atom is coloured depending on their (ΔU) value, as indicated in the top scale bars, from -0.5% (blue) to 0.5 % (red).

7) Concluding remarks

In this dissertation we performed Molecular Dynamics (MD) simulations of a model $Cu_{65}Zr_{35}$ glass. We studied the thermodynamics and the structural and dynamical properties of the system at the quiescent state prepared by two different cooling rates. In addition, we analysed the evolution of the thermodynamical, structural and dynamical quantities upon straining up to a strain of 10% and explored the stress relaxation process that takes place once the straining procedure is completed and the system remains under fixed strain.

The analysis of the atomic coordinates in our glass at 300 K yielded that a small portion of the system's atoms perform rattling motions between two neighboring sites. The to-and-fro motions show a wide distribution of distances and lifetimes, and appear distinct from the motions attributed to the boson peak. The rattling events take place even at the quiescent state, with string-like concerted motions of two or three neighboring atoms and are accompanied by local changes in the atomic coordination, some of which are persistent. The frequency of the rattling mechanism is of the order of 40 GHz, independent of the temperature and the applied strain. We identified the observed rattling between sites as the mechanism (for our simulated metallic glass) of the fast processes that are characteristic of the glassy materials in general and lie in the frequency range between β relaxation and the Boson peak.

Furthermore, we found that the rattling atoms are centers predominantly of geometrically imperfect coordination polyhedra; these are heterogeneously distributed, concentrated in local low-density and high mobility regions with a wide range of sizes. In the quiescent glass (not subjected to externally imposed strain) at 300 K, the frequency of occurrence of rattling events (i.e. the number of rattling movements normalized by the total number of atoms in the system) is 430 MHz for the system cooled down at $2 \cdot 10^{12}$ K/ps and 230 MHz for the system cooled down at $1 \cdot 10^{11}$ K/ps, and in both cases, it rises with temperature. This frequency increases as well to 1.8 GHz when the glass reaches 10% strain and it stabilizes at 800 MHz at the end of the stress relaxation process that takes place after the straining procedure, i.e. with the glass subjected to a constant tensile strain of 10%. The strain application leads to more atoms performing rattling motions, congregated in larger regions. Changes in the atomic

coordination polyhedra, of the kind associated with rattling motions, account for one third of the total volume increase resulting from the imposed strain. The predominant structural change in the glass refers to a reduction in the relative proportion of icosahedral coordination polyhedra.

During the straining process, two regimes were clearly exhibited by our glass and manifested by an endothermic behavior, which has not been reported before. The glass underwent a relaxation or aging regime during the early strain stages. In addition, during these early strain stages, it was possible to observe a small increase in the number of densely packed clusters and a slowdown of the dynamics of the system. This regime was followed by a disorder or rejuvenation process, which became dominant when the strain of the glass reached 4% and took over completely after a strain of 6%. During this process, the fast processes manifested by the atomic rattling were significantly enhanced, causing massive reduction of the number of densely packed clusters and an increase of the number of loosely packed clusters accordingly. Additionally, the dynamics of the system became considerably faster.

The analysis of the rattling atoms was performed as well during the stress relaxation process, which our MGs exhibited once the straining procedure finished and the system was kept under a target strain of 10%. By modelling the stress and energy relaxation decay and the overlap parameter under different conditions, it was possible to obtain a distribution of relaxation times, ranging from less than a picosecond to a few hundred of picoseconds. In addition, it came out that the stress and energy flow upon relaxation takes place mostly in highly localized region that coincide with the localized regions where the atoms are rattling. These findings reinforce the suggestion that the rattling atoms are at the origin for the deformation accommodation and relaxation mechanisms of the MGs

The wide distributions of relaxation times associated with α, β and β’ relaxation modes ensure that there are regions in the frequency (or temperature) spectrum where the different modes overlap and are coupled. The observed rattling of atoms in a concerted string-like motion shows that these fast processes have a link with β relaxation, suggesting that the processes (which, in contrast to the relaxation itself, exhibit little or no thermal activation) are a low-amplitude, short-string precursor of the mentioned β relaxation dynamic mode. These fast processes appear to be predictors for the origin of the shear transformation zones (STZs) that ultimately trigger plastic flow. They are

concentrated in loosely packed regions, the distribution and extent of which are important in determining the mechanical properties of metallic glasses, which in turn could enlighten and assist to understand the macroscopic response of these materials to external perturbations. The results presented on this dissertation are intimately connected to properties of metallic glasses such as ductility, brittleness and toughness fracture. Therefore, they are crucial for the understanding and eventual control and improvement of the metallic glasses outstanding performance.

8) Bibliography

[1] W. K. Jun, R. H. Willens, and P. Duwez, "Non-crystalline Structure in Solidified Gold–Silicon Alloys," *Nature*, vol. 187, no. 4740, pp. 869–870, Sep. 1960.

[2] A. Inoue, K. Ohtera, Z. Tao, and T. Masumoto, "New Amorphous Al-Ln (Ln=Pr, Nd, Sm or Gd) Alloys Prepared by Melt Spinning," *Jpn. J. Appl. Phys.*, vol. 27, no. 9A, p. L1583, Sep. 1988.

[3] A. Inoue, T. Zhang, and T. Masumoto, "Al–La–Ni Amorphous Alloys with a Wide Supercooled Liquid Region," *Mater. Trans. JIM*, vol. 30, no. 12, pp. 965–972, 1989.

[4] A. Inoue, T. Zhang, and T. Masumoto, "Zr–Al–Ni Amorphous Alloys with High Glass Transition Temperature and Significant Supercooled Liquid Region," *Mater. Trans. JIM*, vol. 31, no. 3, pp. 177–183, 1990.

[5] A. Inoue, T. Zhang, and T. Masumoto, "Glass-forming ability of alloys," *J. Non-Cryst. Solids*, vol. 156–158, pp. 473–480, May 1993.

[6] A. Inoue, "Stabilization and high strain-rate superplasticity of metallic supercooled liquid," *Mater. Sci. Eng. A*, vol. 267, no. 2, pp. 171–183, Jul. 1999.

[7] A. Inoue, "Stabilization of metallic supercooled liquid and bulk amorphous alloys," *Acta Mater.*, vol. 48, no. 1, pp. 279–306, Jan. 2000.

[8] C. A. Angell, "Strong and fragile liquids," *Relax. Complex Syst.*, pp. 3–11, 1985.

[9] C. Suryanarayana and A. Inoue, *Bulk metallic glasses*. Boca Raton, Fla.: CRC, 2011.

[10] P. H. Gaskell, "A new structural model for transition metal–metalloid glasses," *Nature*, vol. 276, no. 5687, pp. 484–485, Nov. 1978.

[11] T. M. Hayes, J. W. Allen, J. Tauc, B. C. Giessen, and J. J. Hauser, "Short-Range Order in Metallic Glasses," *Phys. Rev. Lett.*, vol. 40, no. 19, pp. 1282–1285, May 1978.

[12] H. W. Sheng, W. K. Luo, F. M. Alamgir, J. M. Bai, and E. Ma, "Atomic packing and short-to-medium-range order in metallic glasses," *Nature*, vol. 439, no. 7075, pp. 419–425, Jan. 2006.

[13] F. C. Frank, "Supercooling of liquids," *Proc R Soc Lond A*, vol. 215, no. 1120, pp. 43–46, Nov. 1952.

[14] F. C. Frank and J. S. Kasper, “Complex alloy structures regarded as sphere packings. I. Definitions and basic principles,” *Acta Crystallogr.*, vol. 11, no. 3, pp. 184–190, Mar. 1958.

[15] N. Mattern *et al.*, “Short-range order of Cu–Zr metallic glasses,” *J. Alloys Compd.*, vol. 485, no. 1, pp. 163–169, Oct. 2009.

[16] D. B. Miracle, “A structural model for metallic glasses,” *Nat. Mater.*, vol. 3, no. 10, pp. 697–702, Oct. 2004.

[17] G. A. Almyras, C. E. Lekka, N. Mattern, and G. A. Evangelakis, “On the microstructure of the Cu65Zr35 and Cu35Zr65 metallic glasses,” *Scr. Mater.*, vol. 62, no. 1, pp. 33–36, Jan. 2010.

[18] M. Li, C. Z. Wang, S. G. Hao, M. J. Kramer, and K. M. Ho, “Structural heterogeneity and medium-range order in Zr(x)Cu(100-x) metallic glasses,” *Phys. Rev. B*, vol. 80, no. 18, p. 184201, Nov. 2009.

[19] P. G. Debenedetti and F. H. Stillinger, “Supercooled liquids and the glass transition,” *Nature*, vol. 410, pp. 259–267, Mar. 2001.

[20] H. Y. Jiang, P. Luo, P. Wen, H. Y. Bai, W. H. Wang, and M. X. Pan, “The near constant loss dynamic mode in metallic glass,” *J. Appl. Phys.*, vol. 120, no. 14, p. 145106, Oct. 2016.

[21] Q. Wang, S. T. Zhang, Y. Yang, Y. D. Dong, C. T. Liu, and J. Lu, “Unusual fast secondary relaxation in metallic glass,” *Nat. Commun.*, vol. 6, p. 7876, Jul. 2015.

[22] L. Z. Zhao, R. J. Xue, Z. G. Zhu, K. L. Ngai, W. H. Wang, and H. Y. Bai, “A fast dynamic mode in rare earth based glasses,” *J. Chem. Phys.*, vol. 144, no. 20, p. 204507, May 2016.

[23] P. Lunkenheimer, U. Schneider, R. Brand, and A. Loid, “Glassy dynamics,” *Contemp. Phys.*, vol. 41, no. 1, pp. 15–36, Jan. 2000.

[24] H. B. Yu, W. H. Wang, H. Y. Bai, and K. Samwer, “The β-relaxation in metallic glasses,” *Natl. Sci. Rev.*, vol. 1, no. 3, pp. 429–461, Sep. 2014.

[25] P. Lunkenheimer and A. Loidl, “Dielectric spectroscopy of glass-forming materials: α-relaxation and excess wing,” *Chem. Phys.*, vol. 284, no. 1, pp. 205–219, Nov. 2002.

[26] H. B. Yu, K. Samwer, Y. Wu, and W. H. Wang, “Correlation between beta Relaxation and Self-Diffusion of the Smallest Constituting Atoms in Metallic Glasses,” *Phys. Rev. Lett.*, vol. 109, no. 9, p. 095508, Aug. 2012.

[27] H.-B. Yu, W.-H. Wang, and K. Samwer, “The β relaxation in metallic glasses: an overview,” *Mater. Today*, vol. 16, no. 5, pp. 183–191, May 2013.

[28] J. C. Qiao *et al.*, “Transition from stress-driven to thermally activated stress relaxation in metallic glasses,” *Phys. Rev. B*, vol. 94, no. 10, p. 104203, Sep. 2016.

[29] A. P. Sokolov, E. Rössler, A. Kisliuk, and D. Quitmann, “Dynamics of strong and fragile glass formers: Differences and correlation with low-temperature properties,” *Phys. Rev. Lett.*, vol. 71, no. 13, pp. 2062–2065, Sep. 1993.

[30] J. C. Qiao and J. M. Pelletier, “Dynamic mechanical analysis in La-based bulk metallic glasses: Secondary (β) and main (α) relaxations,” *J. Appl. Phys.*, vol. 112, no. 8, p. 083528, Oct. 2012.

[31] H. B. Yu, K. Samwer, W. H. Wang, and H. Y. Bai, “Chemical influence on β-relaxations and the formation of molecule-like metallic glasses,” *Nat. Commun.*, vol. 4, p. 2204, Jul. 2013.

[32] Z. Lu *et al.*, “Revealing β-relaxation mechanism based on energy distribution of flow units in metallic glass,” *J. Chem. Phys.*, vol. 144, no. 14, p. 144501, Apr. 2016.

[33] Y. Li, H. Y. Bai, W. H. Wang, and K. Samwer, “Low-temperature specific-heat anomalies associated with the boson peak in CuZr-based bulk metallic glasses,” *Phys. Rev. B*, vol. 74, no. 5, p. 052201, Aug. 2006.

[34] B. Huang *et al.*, “Hand in hand evolution of boson heat capacity anomaly and slow β-relaxation in La-based metallic glasses,” *Acta Mater.*, vol. 110, pp. 73–83, May 2016.

[35] N. Jakse, A. Nassour, and A. Pasturel, “Structural and dynamic origin of the boson peak in a Cu-Zr metallic glass,” *Phys. Rev. B*, vol. 85, no. 17, p. 174201, May 2012.

[36] J. Ding, S. Patinet, M. L. Falk, Y. Cheng, and E. Ma, “Soft spots and their structural signature in a metallic glass,” *Proc. Natl. Acad. Sci.*, vol. 111, no. 39, pp. 14052–14056, Sep. 2014.

[37] A. L. Greer, “Metallic Glasses,” *Science*, vol. 267, no. 5206, pp. 1947–1953, Mar. 1995.

[38] M. Telford, “The case for bulk metallic glass,” *Mater. Today*, vol. 7, no. 3, pp. 36–43, Mar. 2004.

[39] F. Spaepen, “A microscopic mechanism for steady state inhomogeneous flow in metallic glasses,” *Acta Metall.*, vol. 25, no. 4, pp. 407–415, Apr. 1977.

[40] D. Turnbull and M. H. Cohen, “Free-Volume Model of the Amorphous Phase: Glass Transition,” *J. Chem. Phys.*, vol. 34, no. 1, pp. 120–125, Jan. 1961.

[41] A. S. Argon, “Plastic deformation in metallic glasses,” *Acta Metall.*, vol. 27, no. 1, pp. 47–58, Jan. 1979.

[42] M. L. Falk and J. S. Langer, “Dynamics of viscoplastic deformation in amorphous solids,” *Phys. Rev. E*, vol. 57, no. 6, pp. 7192–7205, Jun. 1998.

[43] T. Egami, T. Iwashita, and W. Dmowski, “Mechanical Properties of Metallic Glasses,” *Metals*, vol. 3, no. 1, pp. 77–113, Jan. 2013.

[44] P. W. Anderson, “Through the Glass Lightly,” *Science*, vol. 267, no. 5204, pp. 1615–1616, Mar. 1995.

[45] F. Hamed, “Positive and Negative Temperature Dependence in the Resistivity of Crystallized Zr-Fe-Ni Metallic Glasses,” *Materials*, vol. 3, no. 12, pp. 5212–5219, Dec. 2010.

[46] J. M. Riveiro and R. Pareja, “Electrical and magnetic properties of metallic glasses during tensile deformation,” *J. Phys. Colloq.*, vol. 49, no. C8, pp. C8-1331-C8-1332, Dec. 1988.

[47] A. Inoue, X. M. Wang, and W. Zhang, “Developments and applications of bulk metallic glasses,” *Rev. Adv. Mater. Sci.*, vol. 18, no. 1, p. 9, 2008.

[48] B. J. Alder and T. E. Wainwright, “Phase Transition for a Hard Sphere System,” *J. Chem. Phys.*, vol. 27, no. 5, pp. 1208–1209, Nov. 1957.

[49] A. Rahman, “Correlations in the Motion of Atoms in Liquid Argon,” *Phys. Rev.*, vol. 136, no. 2A, pp. A405–A411, Oct. 1964.

[50] L. V. Heimendahl and M. F. Thorpe, “Phonons in metallic glasses,” *J. Phys. F Met. Phys.*, vol. 5, no. 6, p. L87, 1975.

[51] G. a. N. Connell, “Electrons and phonons in amorphous semiconductors,” *Phys. Status Solidi B*, vol. 69, no. 1, pp. 9–24, May 1975.

[52] A. Rahman, M. J. Mandell, and J. P. McTague, “Molecular dynamics study of an amorphous Lennard-Jones system at low temperature,” *J. Chem. Phys.*, vol. 64, no. 4, pp. 1564–1568, Feb. 1976.

[53] R. Yamamoto, T. Mihara, K. Taira, and M. Doyama, “Amorphous structures of iron obtained by quenching of the liquid state,” *Phys. Lett. A*, vol. 70, no. 1, pp. 41–43, Feb. 1979.

[54] W. Eckhardt *et al.*, “591 TFLOPS Multi-trillion Particles Simulation on SuperMUC,” in *Supercomputing*, vol. 7905, J. M. Kunkel, T. Ludwig, and H. W. Meuer, Eds. Berlin, Heidelberg: Springer Berlin Heidelberg, 2013, pp. 1–12.

[55] L. Verlet, “Computer ‘Experiments’ on Classical Fluids. I. Thermodynamical Properties of Lennard-Jones Molecules,” *Phys. Rev.*, vol. 159, no. 1, pp. 98–103, Jul. 1967.

[56] D. Frenkel and B. Smit, *Understanding molecular simulation: from algorithms to applications*, 2nd ed. San Diego: Academic Press, 2002.

[57] M. Ferrario, G. Ciccotti, and K. Binder, Eds., *Computer simulations in condensed matter systems: from materials to chemical biology*. Berlin ; New York: Springer, 2006.

[58] D. Fincham, “Choice of timestep in molecular dynamics simulation,” *Comput. Phys. Commun.*, vol. 40, no. 2, pp. 263–269, Jun. 1986.

[59] M. Zhou, “A new look at the atomic level virial stress: on continuum-molecular system equivalence,” *Proc. R. Soc. Lond. Math. Phys. Eng. Sci.*, vol. 459, no. 2037, pp. 2347–2392, Sep. 2003.

[60] D. H. Tsai, “The virial theorem and stress calculation in molecular dynamics,” *J. Chem. Phys.*, vol. 70, no. 3, pp. 1375–1382, Feb. 1979.

[61] J. E. Jones and D. Sc, “On the determination of molecular fields. —II. From the equation of state of a gas,” *Proc R Soc Lond A*, vol. 106, no. 738, pp. 463–477, Oct. 1924.

[62] “Atoms In Motion - Atoms In Motion.” [Online]. Available: http://atomsinmotion.com/.

[63] M. W. Finnis and J. E. Sinclair, “A simple empirical N-body potential for transition metals,” *Philos. Mag. A*, vol. 50, no. 1, pp. 45–55, Jul. 1984.

[64] M. S. Daw and M. I. Baskes, “Semiempirical, Quantum Mechanical Calculation of Hydrogen Embrittlement in Metals,” *Phys. Rev. Lett.*, vol. 50, no. 17, pp. 1285–1288, Apr. 1983.

[65] Y. Q. Cheng, H. W. Sheng, and E. Ma, “Relationship between structure, dynamics, and mechanical properties in metallic glass-forming alloys,” *Phys. Rev. B*, vol. 78, no. 1, p. 014207, Jul. 2008.

[66] M. I. Mendelev *et al.*, “Experimental and computer simulation determination of the structural changes occurring through the liquid–glass transition in Cu–Zr alloys,” *Philos. Mag.*, vol. 90, no. 29, pp. 3795–3815, Oct. 2010.

[67] P.-F. Paradis *et al.*, “Materials properties measurements and particle beam interactions studies using electrostatic levitation,” *Mater. Sci. Eng. R Rep.*, vol. 76, pp. 1–53, Feb. 2014.

[68] F. Ercolessi and J. B. Adams, “Interatomic Potentials from First-Principles Calculations: The Force-Matching Method,” *EPL Europhys. Lett.*, vol. 26, no. 8, p. 583, 1994.

[69] G. Kresse and J. Furthmüller, “Efficiency of ab-initio total energy calculations for metals and semiconductors using a plane-wave basis set,” *Comput. Mater. Sci.*, vol. 6, no. 1, pp. 15–50, Jul. 1996.

[70] P. E. Blöchl, “Projector augmented-wave method,” *Phys. Rev. B*, vol. 50, no. 24, pp. 17953–17979, Dec. 1994.

[71] G. Kresse and D. Joubert, “From ultrasoft pseudopotentials to the projector augmented-wave method,” *Phys. Rev. B*, vol. 59, no. 3, pp. 1758–1775, Jan. 1999.

[72] “Cu-Zr - EAM potentials.” [Online]. Available: https://sites.google.com/site/eampotentials/Home/CuZr.

[73] B. J. Alder, S. P. Frankel, and V. A. Lewinson, “Radial Distribution Function Calculated by the Monte-Carlo Method for a Hard Sphere Fluid,” *J. Chem. Phys.*, vol. 23, no. 3, pp. 417–419, Mar. 1955.

[74] “Periodic Boundary Conditions.” [Online]. Available: http://isaacs.sourceforge.net/phys/pbc.html.

[75] P. H. Hünenberger, “Thermostat Algorithms for Molecular Dynamics Simulations,” in *Advanced Computer Simulation*, Springer, Berlin, Heidelberg, pp. 105–149.

[76] S. Nosé, “A molecular dynamics method for simulations in the canonical ensemble,” *Mol. Phys.*, vol. 52, no. 2, pp. 255–268, Jun. 1984.

[77] W. G. Hoover, “Canonical dynamics: Equilibrium phase-space distributions,” *Phys. Rev. A*, vol. 31, no. 3, pp. 1695–1697, Mar. 1985.

[78] H. C. Andersen, “Molecular dynamics simulations at constant pressure and/or temperature,” *J. Chem. Phys.*, vol. 72, no. 4, pp. 2384–2393, Feb. 1980.

[79] D. A. McQuarrie, *Statistical mechanics*. Sausalito, Calif: University Science Books, 2000.

[80] “What is the pair correlation function g(r)?” [Online]. Available: http://www.physics.emory.edu/faculty/weeks//idl/gofr.html.

[81] “Molecular Simulation/Solids.” [Online]. Available: https://en.wikibooks.org/wiki/Molecular_Simulation/Solids.

[82] G. Voronoi, “Nouvelles applications des paramètres continus à la théorie des formes quadratiques. Deuxième mémoire. Recherches sur les parallélloèdres primitifs.,” *J. Für Reine Angew. Math. Crelles J.*, vol. 1908, no. 134, pp. 198–287, 2009.

[83] Y. Q. Cheng and E. Ma, “Atomic-level structure and structure–property relationship in metallic glasses,” *Prog. Mater. Sci.*, vol. 56, no. 4, pp. 379–473, May 2011.

[84] S. G. Hao *et al.*, “Experimental and ab initio structural studies of liquid Zr2Ni,” *Phys. Rev. B*, vol. 79, no. 10, p. 104206, Mar. 2009.

[85] C. H. Rycroft, “VORO++: A three-dimensional Voronoi cell library in C++,” *Chaos Interdiscip. J. Nonlinear Sci.*, vol. 19, no. 4, p. 041111, Oct. 2009.

[86] A. Entezari, D. V. D. Ville, and T. Möeller, “Practical Box Splines for Reconstruction on the Body Centered Cubic Lattice,” *IEEE Trans. Vis. Comput. Graph.*, vol. 14, no. 2, pp. 313–328, Mar. 2008.

[87] Y. D. Wei *et al.*, “A comparative study on local atomic configurations characterized by cluster-type-index method and Voronoi polyhedron method,” *Comput. Mater. Sci.*, vol. 123, pp. 214–223, Oct. 2016.

[88] G. A. Almyras, D. G. Papageorgiou, C. E. Lekka, N. Mattern, J. Eckert, and G. A. Evangelakis, “Atomic cluster arrangements in Reverse Monte Carlo and Molecular Dynamics structural models of binary Cu–Zr Metallic Glasses,” *Intermetallics*, vol. 19, no. 5, pp. 657–661, May 2011.

[89] H. Zhang *et al.*, “Role of string-like collective atomic motion on diffusion and structural relaxation in glass forming Cu-Zr alloys,” *J. Chem. Phys.*, vol. 142, no. 16, p. 164506, Apr. 2015.

[90] R. Metzler and J. Klafter, “The random walk’s guide to anomalous diffusion: a fractional dynamics approach,” *Phys. Rep.*, vol. 339, no. 1, pp. 1–77, Dec. 2000.

[91] E. R. Weeks and D. A. Weitz, “Subdiffusion and the cage effect studied near the colloidal glass transition,” *Chem. Phys.*, vol. 284, no. 1, pp. 361–367, Nov. 2002.

[92] B. Doliwa and A. Heuer, “Cage Effect, Local Anisotropies, and Dynamic Heterogeneities at the Glass Transition: A Computer Study of Hard Spheres,” *Phys. Rev. Lett.*, vol. 80, no. 22, pp. 4915–4918, Jun. 1998.

[93] H. L. Peng, M. Z. Li, and W. H. Wang, “Structural Signature of Plastic Deformation in Metallic Glasses,” *Phys. Rev. Lett.*, vol. 106, no. 13, Mar. 2011.

[94] N. P. Bailey, J. Schiøtz, and K. W. Jacobsen, “Atomistic simulation study of the shear-band deformation mechanism in Mg-Cu metallic glasses,” *Phys. Rev. B*, vol. 73, no. 6, p. 064108, Feb. 2006.

[95] G. Parisi, “Numerical indications for the existence of a thermodynamic transition in binary glasses,” *J. Phys. Math. Gen.*, vol. 30, no. 24, p. 8523, 1997.

[96] N. Lačević, F. W. Starr, T. B. Schrøder, and S. C. Glotzer, “Spatially heterogeneous dynamics investigated via a time-dependent four-point density correlation function,” *J. Chem. Phys.*, vol. 119, no. 14, pp. 7372–7387, Sep. 2003.

[97] S. Sengupta, F. Vasconcelos, F. Affouard, and S. Sastry, “Dependence of the fragility of a glass former on the softness of interparticle interactions,” *J. Chem. Phys.*, vol. 135, no. 19, p. 194503, Nov. 2011.

[98] S. Sengupta, S. Karmakar, C. Dasgupta, and S. Sastry, “Breakdown of the Stokes-Einstein relation in two, three, and four dimensions,” *J. Chem. Phys.*, vol. 138, no. 12, p. 12A548, Mar. 2013.

[99] A. Ninarello, L. Berthier, and D. Coslovich, “Structure and dynamics of coupled viscous liquids,” *Mol. Phys.*, vol. 113, no. 17–18, pp. 2707–2715, Sep. 2015.

[100] I. Procaccia, C. Rainone, and M. Singh, “Mechanical failure in amorphous solids: Scale-free spinodal criticality,” *Phys. Rev. E*, vol. 96, no. 3, p. 032907, Sep. 2017.

[101] N. Mattern, A. Schöps, U. Kühn, J. Acker, O. Khvostikova, and J. Eckert, “Structural behavior of CuxZr100−x metallic glass (x=35−70),” *J. Non-Cryst. Solids*, vol. 354, no. 10, pp. 1054–1060, Feb. 2008.

[102] C. Tang, H. Peng, Y. Chen, and M. Ferry, “Formation and dilatation of shear bands in a Cu-Zr metallic glass: A free volume perspective,” *J. Appl. Phys.*, vol. 120, no. 23, p. 235101, Dec. 2016.

[103] I. Bakonyi, “Atomic volumes and local structure of metallic glasses,” *Acta Mater.*, vol. 53, no. 8, pp. 2509–2520, May 2005.

[104] M. I. Mendelev, D. K. Rehbein, R. T. Ott, M. J. Kramer, and D. J. Sordelet, “Computer simulation and experimental study of elastic properties of amorphous Cu-Zr alloys,” *J. Appl. Phys.*, vol. 102, no. 9, p. 093518, Nov. 2007.

[105] B. Jelinek *et al.*, “Modified embedded atom method potential for Al, Si, Mg, Cu, and Fe alloys,” *Phys. Rev. B*, vol. 85, no. 24, p. 245102, Jun. 2012.

[106] C. E. Lekka, A. Ibenskas, A. R. Yavari, and G. A. Evangelakis, “Tensile deformation accommodation in microscopic metallic glasses via subnanocluster reconstructions,” *Appl. Phys. Lett.*, vol. 91, no. 21, p. 214103, Nov. 2007.

[107] Y. Zhang *et al.*, “Impact of deformation on the atomic structures and dynamics of a Cu-Zr metallic glass: A molecular dynamics study,” *Phys. Rev. B*, vol. 90, no. 17, p. 174101, Nov. 2014.

[108] H. S. Chen and Y. Waseda, “Structure of glassy Zr-Cu and Nb-Ni alloys,” *Phys. Status Solidi A*, vol. 51, no. 2, pp. 593–599, Feb. 1979.

[109] H. S. Chen and J. T. Krause, “Correlation between young’s modulus and thermal properties of metallic glasses,” *Scr. Metall.*, vol. 11, no. 9, pp. 761–764, Sep. 1977.

[110] K.-W. Park, C.-M. Lee, M.-R. Lee, E. Fleury, M. L. Falk, and J.-C. Lee, “Paradoxical phenomena between the homogeneous and inhomogeneous deformations of metallic glasses,” *Appl. Phys. Lett.*, vol. 94, no. 2, p. 021907, Jan. 2009.

[111] N. Mattern, J. Bednarcik, M. Stoica, and J. Eckert, “Temperature dependence of the short-range order of Cu65Zr35 metallic glass,” *Intermetallics*, vol. 32, pp. 51–56, Jan. 2013.

[112] A. L. Greer and Y. H. Sun, “Stored energy in metallic glasses due to strains within the elastic limit,” *Philos. Mag.*, vol. 96, no. 16, pp. 1643–1663, Jun. 2016.

[113] H. S. Chen, “Glassy metals,” *Rep. Prog. Phys.*, vol. 43, no. 4, p. 353, 1980.

[114] K.-W. Park, J. Jang, M. Wakeda, Y. Shibutani, and J.-C. Lee, “Atomic packing density and its influence on the properties of Cu–Zr amorphous alloys,” *Scr. Mater.*, vol. 57, no. 9, pp. 805–808, Nov. 2007.

[115] I. Kaban *et al.*, “Local atomic arrangements and their topology in Ni–Zr and Cu–Zr glassy and crystalline alloys,” *Acta Mater.*, vol. 61, no. 7, pp. 2509–2520, Apr. 2013.

[116] T. Tomida and T. Egami, “Molecular-dynamics study of structural anisotropy and anelasticity in metallic glasses,” *Phys. Rev. B*, vol. 48, no. 5, pp. 3048–3057, Aug. 1993.

[117] Y. Zhang, N. Mattern, and J. Eckert, “Effect of uniaxial loading on the structural anisotropy and the dynamics of atoms of Cu50Zr50 metallic glasses within the elastic regime studied by molecular dynamics simulation,” *Acta Mater.*, vol. 59, no. 11, pp. 4303–4313, Jun. 2011.

[118] K.-H. Kang, K.-W. Park, J.-C. Lee, E. Fleury, and B.-J. Lee, “Correlation between plasticity and other materials properties of Cu–Zr bulk metallic glasses: An atomistic simulation study,” *Acta Mater.*, vol. 59, no. 2, pp. 805–811, Jan. 2011.

[119] X. D. Wang, S. Yin, Q. P. Cao, J. Z. Jiang, H. Franz, and Z. H. Jin, “Atomic structure of binary Cu64.5Zr35.5 bulk metallic glass,” *Appl. Phys. Lett.*, vol. 92, no. 1, p. 011902, Jan. 2008.

[120] D. V. Louzguine-Luzgin, A. R. Yavari, G. Vaughan, and A. Inoue, “Clustered crystalline structures as glassy phase approximants,” *Intermetallics*, vol. 17, no. 7, pp. 477–480, Jul. 2009.

[121] M. Wakeda and Y. Shibutani, “Icosahedral clustering with medium-range order and local elastic properties of amorphous metals,” *Acta Mater.*, vol. 58, no. 11, pp. 3963–3969, Jun. 2010.

[122] R. Liu, K. Dong, J. Li, A. Yu, and R. Zou, “Formation and description of nano-clusters formed during rapid solidification processes in liquid metals,” *J. Non-Cryst. Solids*, vol. 351, no. 6, pp. 612–617, Mar. 2005.

[123] Y. L. Sun, J. Shen, and A. A. Valladares, “Atomic structure and diffusion in Cu60Zr40 metallic liquid and glass: molecular dynamics simulations,” *J. Appl. Phys.*, vol. 106, no. 7, p. 073520, Oct. 2009.

[124] M. Kluge and H. R. Schober, “Diffusion and jump-length distribution in liquid and amorphous Cu33Zr67,” *Phys. Rev. B*, vol. 70, no. 22, p. 224209, Dec. 2004.

[125] S. Küchemann and R. Maaß, “Gamma relaxation in bulk metallic glasses,” *Scr. Mater.*, vol. 137, pp. 5–8, Aug. 2017.

[126] Y. Fan, T. Iwashita, and T. Egami, “How thermally activated deformation starts in metallic glass,” *Nat. Commun.*, vol. 5, p. 5083, Sep. 2014.

[127] A. J. Cao, Y. Q. Cheng, and E. Ma, “Structural processes that initiate shear localization in metallic glass,” *Acta Mater.*, vol. 57, no. 17, pp. 5146–5155, Oct. 2009.

[128] S. Q. Wu, C. Z. Wang, S. G. Hao, Z. Z. Zhu, and K. M. Ho, “Energetics of local clusters in Cu64.5Zr35.5 metallic liquid and glass,” *Appl. Phys. Lett.*, vol. 97, no. 2, p. 021901, Jul. 2010.

[129] D. Bedorf and K. Samwer, “Length scale effects on relaxations in metallic glasses,” *J. Non-Cryst. Solids*, vol. 356, no. 6, pp. 340–343, Mar. 2010.

[130] M. Zink, K. Samwer, W. L. Johnson, and S. G. Mayr, “Plastic deformation of metallic glasses: Size of shear transformation zones from molecular dynamics simulations,” *Phys. Rev. B*, vol. 73, no. 17, p. 172203, May 2006.

[131] R. D. Conner, W. L. Johnson, N. E. Paton, and W. D. Nix, “Shear bands and cracking of metallic glass plates in bending,” *J. Appl. Phys.*, vol. 94, no. 2, pp. 904–911, Jun. 2003.

[132] C. A. Schuh, T. C. Hufnagel, and U. Ramamurty, “Mechanical behavior of amorphous alloys,” *Acta Mater.*, vol. 55, no. 12, pp. 4067–4109, Jul. 2007.

[133] A. R. Yavari, J. J. Lewandowski, and J. Eckert, “Mechanical Properties of Bulk Metallic Glasses,” *MRS Bull.*, vol. 32, no. 8, pp. 635–638, Aug. 2007.

[134] M. Wakeda, J. Saida, J. Li, and S. Ogata, “Controlled Rejuvenation of Amorphous Metals with Thermal Processing,” *Sci. Rep.*, vol. 5, p. 10545, May 2015.

[135] L. Wang, M. C. Liu, J. C. Huang, Y. Li, W. H. Wang, and T. G. Nieh, “Effect of temperature on the yield strength of a binary CuZr metallic glass: Stress-induced glass transition,” *Intermetallics*, vol. 26, pp. 162–165, Jul. 2012.

[136] N. Mattern, J. Bednarčik, S. Pauly, G. Wang, J. Das, and J. Eckert, “Structural evolution of Cu–Zr metallic glasses under tension,” *Acta Mater.*, vol. 57, no. 14, pp. 4133–4139, Aug. 2009.

[137] K.-W. Park, C.-M. Lee, M. Wakeda, Y. Shibutani, M. L. Falk, and J.-C. Lee, “Elastostatically induced structural disordering in amorphous alloys,” *Acta Mater.*, vol. 56, no. 19, pp. 5440–5450, Nov. 2008.

[138] D. Xu, B. Lohwongwatana, G. Duan, W. L. Johnson, and C. Garland, “Bulk metallic glass formation in binary Cu-rich alloy series – Cu100−xZrx (x=34, 36, 38.2, 40 at.%) and mechanical properties of bulk Cu64Zr36 glass,” *Acta Mater.*, vol. 52, no. 9, pp. 2621–2624, May 2004.

[139] G. Duan, K. De Blauwe, M. L. Lind, J. P. Schramm, and W. L. Johnson, “Compositional dependence of thermal, elastic, and mechanical properties in Cu–Zr–Ag bulk metallic glasses,” *Scr. Mater.*, vol. 58, no. 3, pp. 159–162, Feb. 2008.

[140] P. Palomino Rico, D. G. Papageorgiou, A. L. Greer, and G. A. Evangelakis, “The atomistic mechanism of fast relaxation processes in Cu65Zr35 glass,” *Acta Mater.*, vol. 135, pp. 290–296, Aug. 2017.

[141] X. W. Fang *et al.*, “Spatially Resolved Distribution Function and the Medium-Range Order in Metallic Liquid and Glass,” *Sci. Rep.*, vol. 1, p. 194, Dec. 2011.

[142] A. L. Greer, Y. Q. Cheng, and E. Ma, “Shear bands in metallic glasses,” *Mater. Sci. Eng. R Rep.*, vol. 74, no. 4, pp. 71–132, Apr. 2013.

[143] D. Roylance, “Engineering viscoelasticity,” Oct. 2001.

[144] G. Williams and D. C. Watts, “Non-symmetrical dielectric relaxation behaviour arising from a simple empirical decay function,” *Trans. Faraday Soc.*, vol. 66, no. 0, pp. 80–85, Jan. 1970.

[145] C. Liu, E. Pineda, and D. Crespo, “Mechanical Relaxation of Metallic Glasses: An Overview of Experimental Data and Theoretical Models,” *Metals*, vol. 5, no. 2, pp. 1073–1111, Jun. 2015.

[146] Z. Wang, B. A. Sun, H. Y. Bai, and W. H. Wang, “Evolution of hidden localized flow during glass-to-liquid transition in metallic glass,” *Nat. Commun.*, vol. 5, p. 5823, Dec. 2014.

[147] Y. Z. Li, L. Z. Zhao, C. Wang, Z. Lu, H. Y. Bai, and W. H. Wang, “Communication: Non-monotonic evolution of dynamical heterogeneity in unfreezing process of metallic glasses,” *J. Chem. Phys.*, vol. 143, no. 4, p. 041104, Jul. 2015.

[148] J. C. Qiao, Y.-J. Wang, J. M. Pelletier, L. M. Keer, M. E. Fine, and Y. Yao, “Characteristics of stress relaxation kinetics of La60Ni15Al25 bulk metallic glass,” *Acta Mater.*, vol. 98, pp. 43–50, Oct. 2015.

[149] J. Ketkaew, M. Fan, M. D. Shattuck, C. S. O’Hern, and J. Schroers, “Structural relaxation kinetics defines embrittlement in metallic glasses,” *Scr. Mater.*, vol. 149, pp. 21–25, May 2018.